Atomic force microscopy studies on the electrostatic environment and energy levels of self-assembled quantum dots

Lynda Patricia Cockins

Department of Physics
McGill University
Montréal, Québec, Canada
June 2010

A thesis submitted to McGill University
in partial fulfillment of the requirements of the degree of
Doctor of Philosophy

To my husband

Abstract

The ability of quantum dots to confine single charges at discrete energy levels makes them a promising platform for novel electronic and optoelectronic devices. Self-assembled quantum dots are of considerable interest because their size, shape, and material can be controlled during growth. These properties influence the confinement potential, thereby controlling the energy levels of the dot. However, the method of growth does not allow for positioning of the quantum dots which end up randomly distributed over the sample surface, making it difficult for lithographic techniques to access the quantum dots to perform either charge transport or charge sensing measurements so that single dot properties can be measured.

An atomic force microscope (AFM) can be used to spatially access individual dots, and by applying a voltage between cantilever tip and back-electrode, the energy levels of individual dots can be measured as electrons are added to the dot one-by-one in the Coulomb blockade regime. The oscillating cantilever in these experiments is responsible for both loading the dots through electrical gating and also detecting tunneling events through a change in cantilever resonance frequency and/or cantilever dissipation.

We use an AFM to measure the energy levels in few electron self-assembled InAs quantum dots. The charging energy, level spacing, and shell structure of single dots are extracted experimentally. We compare our results to a theoretical model that

describes in detail the mechanism behind the dissipative electrostatic interaction due to the tunneling single-electrons.

Examples of the electrostatic influence of the environment on the dots are also presented, and a method for using an AFM for characterizing electrostatic noise is demonstrated. Charge fluctuations are known to compromise the operation of electronic devices, especially for electrical components which are built in the micron and nano regime. Super bandgap irradiation leads to generation-recombination noise over the sample surface but not over the self-assembled quantum dots. We measure the generation-recombination noise with an AFM and compare the noise on and off the dot to show sub-20 nm spatial resolution, demonstrating the ability of AFM for characterizing noise arising from charge fluctuations within the sample with high spatial resolution.

Résumé

La propriété qu'ont les points quantiques de confiner des charges élémentaires à des niveaux discrets d'énergie en font une plate-forme prometteuse pour la conception de nouveaux appareils électroniques et opto-électroniques. Les points quantiques auto-assemblés sont d'autant plus intéressants puisque leur taille, forme et matériau peuvent être contrôlés lors de leur croissance. Ces propriétés influencent le potentiel de confinement modifiant ainsi les niveaux d'énergies du point quantique. Toutefois, cette méthode de croissance ne permet pas de positionner les points quantiques et ceux-ci se retrouvent distribués aléatoirement sur la surface de l'échantillon. Cela rend difficile l'accès aux points quantiques par des techniques lithographiques pour effectuer des mesures de transport ou de détection de charge permettant d'en déterminer les propriétés.

Un microscope à force atomique (AFM) permet d'accéder spatialement à des points quantiques individuels et en appliquant une tension électrique entre la pointe du cantilever et une électrode arrière, leurs niveaux d'énergies peuvent être mesurés au fur et à mesure que des électrons sont ajoutés dans un régime de blocage de Coulomb. Dans ces expériences, le cantilever oscillant est responsable simultanément du chargement des points par l'application d'une tension de grille et de la détection du passage d'électron par $\ll$ effet tunnel $\gg$ par un changement de fréquence de résonance et/ou de dissipation du cantilever.

Nous utilisons un AFM pour mesurer les niveaux d'énergie dans des points quantiques à quelques électrons d'InAs auto-assemblés. L'énergie de chargement, l'espacement des niveaux et la configuration électronique de points individuels sont obtenus expérimentalement. Nous comparons nos résultats à un modèle théorique qui décrit en détail le mécanisme derrière l'interaction électrostatique dissipative due au passage d'électrons par $\ll$ effet tunnel $\gg$.

Des exemples de l'influence électrostatique de l'environnement sur les points quantiques sont aussi présentés, ainsi qu'une méthode pour utiliser l'AFM pour caractériser le bruit électrostatique. Les fluctuations de charge sont connues pour compromettre le bon fonctionnement des appareils électroniques et particulièrement des composants micro et nanométriques. L'irradiation de larges bandes d'énergie interdites produit un bruit de génération et de recombinaison à la surface de l'échantillon, mais pas sur les points quantiques auto-assembls. Nous mesurons ce bruit avec un AFM et comparons les résultats obtenus sur la surface du point quantique et en dehors en démontrant qu'une résolution spatiale inférieure à 20 nm est réalisée. Nous démontrons ainsi qu'un AFM permet de caractériser le bruit provenant des fluctuations de charge d'un échantillon avec une haute résolution spatiale.

Statement Of Originality

This thesis focuses on using electrostatic force microscopy to characterize the electronic properties of localized states (quantum dots and charge traps) at the nanoscale. The research comprised within this thesis which has led to an advancement in the field is summarized below:

1. Spatial variations of generation-recombination noise was demonstrated using an atomic force microscope.

Published [L. Cockins, Y. Miyahara, P. Grutter PRB 79 (12) 121309 (2009)]. This article was a Rapid Communication in PRB and was also selected as Editor's Choice.

2.

- Energy level spectroscopy of self-assembled InAs dots is performed using an atomic force microscope.
- Shell degeneracy of quantum dots was verified experimentally using a temperature dependence experiment.
- Images captured showing changes (reversible and time dependent) in quantum dot confinement potentials using an atomic force microscope.
- Coupling between multi-dot complexes is characterized using the atomic force microscope images.

Published [L. Cockins, Y. Miyahara, S. D. Bennett, A. A. Clerk, S. Studenikin, P. Poole, A. Sachrajda and P. Grutter. PNAS 107 (21) 9496 (2010)]

3. The ability to verify the shell structure of the quantum dots by measuring the dot energy levels with large cantilever oscillation amplitudes was verified experimentally.

Published [S. D. Bennett, L. Cockins, Y. Miyahara, P. Grütter and A. A. Clerk. PRL 104 (1) 017203 (2010)]

4. The ability to manipulate the confinement potential of the quantum dot is demonstrated in [L. Cockins, Y. Miyahara, P. Grutter PRB 79 (12) 121309 (2009)] by applying a voltage near the dot, and in this thesis by depositing charge near the dot.

Acknowledgements

I have really enjoyed my research project and my time spent at McGill, and it was all because of the kindness and helpfulness of the wonderful people who I am surrounded by. I have a lot of people to thank for their willingness to help and the generous offering of their time, knowledge and experience.

I thank my supervisor, Dr. Peter Grutter, for giving me so many amazing opportunities during the time I spent in his group. He has sent me all over the world to present, and learn about, science. He allowed me the freedom to pursue my scientific interests, even when that has meant chasing interesting features which were not part of the original plan, but which led to the majority of the data presented within this thesis.

I am exceedingly grateful to have had the supervision of Dr. Yoichi Miyahara. His encouragement, ingenuity, and enthusiasm kept me motivated, even during the difficult times. He has been a major influence on my development as a scientist and researcher, and instrumental to the success of this thesis.

I want to especially thank Steve Bennett for his contribution to the work in this thesis. Steve and Dr. Aash Clerk were responsible for the derivation of all of the theory pertaining to the detection of electron tunneling with an oscillating cantilever that is presented in this thesis. I always enjoy working with Steve because he is so

reliable, careful, and giddy about quantum physics. It was a lot of fun to see the world from a theorist's eyes while we worked together on the quantum dot analysis.

I thank everyone who has provided samples for me to study. In particular, Philip Poole and Sergei Studenikin for the chemical beam epitaxy samples (especially for the quantum dot samples), Mehdi El Ouali for the gold on mica samples, and Dr. Faisal Aldaye and Dr. Hanadi Sleimann for the gold nanoparticle-DNA samples.

Our collaborators at the National Research Council of Canada, Andy Sachrajda, Sergei Studenikin, and Philip Poole have been an excellent resource for useful discussions on anything to do with the quantum dots and I thank them for their helpfulness, enthusiasm, and for sharing their knowledge.

I give a special thank-you to everyone in my research group that has helped me solve all the "little" things, for all of the helpful discussions, and for our envious group dynamic. In particular, I want to thank Dr. Romain Stomp for teaching me how to use the AFM, and Mehdi El Ouali and Will Paul for sharing their Matlab expertise.

I thank Antoine Roy-Gobeil for translating my English abstract into French.

The staff in the physics department has always gone above the call of duty for me. I want to especially thank Robert Gagnon and John Smeros, the "go-to" guys if you have any kind of experimental difficulty. I have yet to come up with a problem that they were not able to solve, a structure they were not able to build, or a broken instrument that they were not able to fix. The tech-guys, Juan Gallego and Paul Mercure, have been especially helpful towards me. Also, the secretaries Louise, Diane, Sonia, Paula, Elizabeth, and Eddie have all contributed towards making my life as a grad student easier.

I thank NSERC, Carl Reinhardt (McGill Majors scholarship), and Walter C. Sumner for financially supporting me throughout my PhD.

Finally, I thank my support group of family and friends. In particular, I thank my mom for listening to me talk about my research almost everyday for the last five years, and my dear husband for his endless support and encouragement.

Table of Contents

List of Figures

CHAPTER 1

Introduction

Once we begin entertaining the notion of building devices out of nanoscale objects an appreciation of quantum phenomena is crucial since we now find ourselves on the same length scale as the wavelengths of the electrons themselves. For conductive materials, to get down to this length scale, we already have made a number of transitions between the appropriate models that describe our system. Although we start off with a bulk material which is three dimensional, we begin to confine electrons within the material, one dimension at a time, so that we first obtain two-dimensional films, then one-dimensional wires, and finally zero-dimensional quantum dots. Of course, none of these are mathematically three, two, one, or zero-dimensional, but the systems can be described that way since the de Broglie wavelength of the electron in that system is on the same order as the confining physical dimension [1]. Using quantum mechanics, we can capture some of the basic principles of these quasi-zero dimensional structures by using the familiar electron-in-a-box calculations. These calculations readily show that electrons in a potential well can occupy only discrete energy states, where the spacing of these states depends on the shape, and depth, of the confining potential.

Quantum dots come in many different shapes and sizes. Typically, they are between a few and tens of nanometers. The material, size, and shape affects the shape of the confinement potential. Symmetric confinement potentials (which are smooth on the order of the de Broglie wavelength) lead to an energy level spacing, ΔE, between shells of degenerate energy levels (called shell structure). For example, spherical colloidal nanoparticles have shell structures similar to atoms because of their spherical symmetry, while disk-shaped quantum dots have a slightly different shell structure. Examples of disk-shaped quantum dots are those lithographically etched out of a two-dimensional electron gas (e.g. a thin layer in a pillar [2]), and self-assembled quantum dots sometimes fall into this category.

Unlike atoms, quantum dots are not restricted to a spherical shape and so different shell structures are possible. In addition, whereas the spacing of the atomic energy levels is on the order of 1 eV, the spacing in semiconductor quantum dots is on the order of 0.01 - 10 meV. The other relevant energy scale is the energy required to add/remove an electron to the dot, similar to the process of ionization for an atom [3]. There is an energy cost for adding an additional electron to the dot due to the Coulomb repulsion from the electrons already residing there. Called the charging energy, E_C, this energy cost can be large enough to suppress electron tunneling into the dot at low temperature. Quantum dots typically have charging energies in the range of 10 meV, while the ionization energy of atoms is on the order of 10 eV. The large difference between these energy scales makes it possible to investigate phenomena that is experimentally challenging or potentially even unattainable in atoms. For example it is easier to study the effect of magnetic fields, since magnetic fields on the order of 1 T can lead to considerable change in the shape of the wavefunctions of electrons in a quantum dot, but for atoms the same modification to the wavefunction

would require magnetic fields on the order of 10^6 T [4]. The size difference also has a practical advantage as the larger quantum dots are easier to incorporate into devices because of the current limitations of micro and nano fabrication techniques. Since the properties of quantum dots depend heavily on their size, composition and shape, there are more available types of energy level structures in quantum dots than in atoms and thus there is potential for engineering these levels through quantum dot growth for specific applications or for study.

When the charging energy is large enough to suppress tunneling, energy must be given to the electrons in a nearby reservoir to overcome this energy cost before an electron can be added to the dot. This is done by applying a voltage across the dot and electron reservoir. As the voltage is increased, this energy cost will be sequentially overcome, each time with a single electron tunneling from the reservoir into the dot. If this is done by attaching two electrodes to the dot, and then using a gate electrode to shift an electrochemical potential level of the dot into the electrochemical potential window of the two electrodes (i.e. $\mu_{source} \geq \mu_{dot} \geq \mu_{drain}$ for the electrochemical potentials of the source, drain and dot) then a single electron current will flow between the electrodes through the dot. In such an experiment peaks are measured in the current, as the gate voltage is swept, whenever the electron addition energy is overcome. If the discrete energy level spacings of the dot are on the order of the charging energy, then these are also resolved in the peak spacing. Historically, single electron transport/charging phenomena was first investigated when peaks were observed in the current through a granular metal film (See [3] for a review). The first transport measurement through a single metal particle was in 1995 by Ralph et al. [5]. In this report Ralph et al. observed both single electron charging effects and the energy level spacing of the dot.

There are a few different approaches for *electrically* performing energy level spectroscopy of single quantum dots. The majority of methods require attaching electrodes nearby the dot. In addition to the electrodes (source, drain and sometimes gate) surrounding a quantum dot as discussed above where a single electron current must pass through the dot, other methods include: lithographically defined lateral dots and electrodes, vertical dots such as etched pillar designs and nanowires, and scanning tunneling microscopy. Methods not requiring a current to flow through the dot are lateral dots using a quantum point contact (QPC) or single electron transistor, capacitance spectroscopy and atomic force microscopy. Charge sensing techniques (those not requiring a current to be passed through the dot) are preferred because in order to have a current through the dot, the tunneling barriers must be relatively small which makes higher order tunneling processes more likely, and this makes it more difficult to control the coherence of the quantum state [6]. Sometimes two of these methods are combined so that one has electrodes and a scanning electrode (i.e. a cantilever from an atomic force microscopy experiment), this technique is referred to as scanning gate microscopy and it offers spatial control of the movable gate and the ability to image the surface topography in situ. In order to understand how our measurements fit into this scheme, each of these methods is described briefly.

In lateral quantum dots, electrons are often confined electrostatically in semiconductor heterostructures by applying negative voltages to lithographically defined electrodes which lie in a plane parallel to, but separated from, a two-dimensional electron gas. Negative voltages deplete the region of the two-dimensional electron gas directly below the electrodes, and electrons pool into other regions. Cleverly designed electrodes create a well formed quantum dot out of this pool. At low temperatures where the charging energy is important, a transport measurement between

the source and drain electrodes reveals single electron charging effects. The first intentional quantum dot created in this way was done by Meirav et al. in 1990 and single electron charging of this dot was demonstrated [7]. The first example of a lateral dot confined electrostatically that reached the few electron regime was in 2000 by researchers at the National Research Council of Canada [8].

As with all electrical conductance measurements, real-time detection is restricted by the minimal detectable current. For example, presently the smallest resolvable currents are roughly 10 fA, which corresponds to a tunneling rate of 10 fA/e $\sim$ 100 kHz [9]. Smaller tunneling rates will simply not lead to a large enough current to be measured via a transport measurement. In order to measure single electron loading into dots with small tunneling rates, charge sensing techniques must be used. The first QPC for measuring the charging energy of an electrostatically confined semiconductor lateral dot was in 1993 by Field et al [10]. The current running through the QPC is gated by the number of electrons in the dot, making real-time read-out of the charge state of the quantum dot possible since the bandwidth on the current measurement is decoupled from the number of electrons tunneling into the dot. Real-time detection of the electron occupation of a dot was achieved with a QPC in 2004 [6, 11], and slightly earlier with a single electron transistor nearby the dot [12, 13].

Whereas the orientation of the lateral dots has source and drain electrodes at the sides and in plane with the dot, a vertical dot (e.g. in an etched pillar or nanowire) has the source and drain electrodes above and below the dot. Although for spherical dots this would not make a difference, for non-spherical dots the extent of the electron wavefunction would lead to a different coupling to the electrodes. Often for vertical dots, several layers of semiconductors are grown by molecular beam

epitaxy or chemical beam epitaxy techniques, and then the whole sample is etched away so that only a pillar remains. The relevant layers of the pillar are the top electrode, tunnel barrier, quantum well, tunneling barrier, and bottom electrode. The layered cylindrically symmetric pillars give rise to disk-shaped quantum dots with parabolic confinement potentials. Transport measurements are then used to measure the energy levels of the dot. The first demonstration of a pillar dot was by Reed et al. in 1988 [14], where they measured the energy level spacings of the dot. In 1996, Tarucha et al. measured the charging energy and discrete energy level separation of a InGaAs quantum dot and showed that it had the shell structure expected of a disk-shaped, few electron quantum dot [2].

Another type of dot formed within pillars are those grown in semiconductor nanowires. The nanowires grow out of a bulk substrate with a width that is on the order of the diameter of the gold nanoparticle that seeded the growth (typically a wire may have a 50 nm diameter and the dot a 10 nm thickness). Transport measurements done on an InAs wire with two, thin InP tunnel barriers with a small segment of InAs between them, resulted in a few electron quantum dot with shell structure [15].

Single-electron capacitance spectroscopy [16] measures small changes in charge collected on a parallel plate capacitor which straddles a quantum dot in order to detect single electron charging of a dot. In these experiments, the dot is separated from a bottom electrode by a tunnel barrier and a top electrode by a layer which does not allow tunneling in a layered semi-conductor structure built by molecular beam epitaxy. When the voltage of the bottom electrode is resonant with a dot level, an electron can tunnel on and off the dot and this fluctuating charge is sensed on the upper plate which is connected to a sensitive electrometer. In 1992, Ashoori et

al. introduced single-electron capacitance spectroscopy and single electron charging of several electron puddles were reported. Although the goal was to have a single quantum dot, from the data the authors deduced that potential fluctuations in the confinement potential broke the dot into several localized electron pools [16]. In 1993, the same group published results where they had obtained a single dot, which they analyzed in the few electron regime under magnetic fields between zero and seven Tesla [17]. In 1994, Drexler et al., instead of having a relatively large quantum dot defined within a two-dimensional electron gas, studied an ensemble of InGaAs self-assembled quantum dots of diameter 20 nm. Using capacitance spectroscopy, and by comparing their results to a model, the authors convincingly deduced that they observed the expected shell structure of quantum dots with a parabolic confinement potential. Furthermore, their quantum dots showed the first example of the energy level spacing being larger than the charging energy [18]. Relevant to the work in this thesis, in 1997 Miller et al. performed a similar experiment as in Ref. [18] but with InAs self-assembled dots and were able to confirm that, on average, these dots also had the shell structure expected of dots with a parabolic confinement potential [19]. Single-electron capacitance spectroscopy is a powerful method for investigating the properties of quantum dots, however it is restricted to studying the quantum dots that are between the capacitor plates which has so far led to only large dots or dot ensembles being measured.

The scanning probe microscopes, such as the scanning tunneling microscope (STM) and the atomic force microscope (AFM), can routinely access sub-30nm length scales. Typically, they are used to first map out the surface topography and then probe some other local property of the sample. A small probe, often a cone-like structure with the smallest tip apex possible (on the order of 10 nm in diameter) is

brought into close proximity to the sample and the interaction that the probe has with the sample is not only measurable but is often used as part of a feedback-loop to control the distance between the sample and probe. The benefits of scanning probe techniques over the ones aforementioned is the lack of a need for electrodes to be built around the dot and, consequently, that several individual dots can be measured in one experiment. Lithography techniques are not yet to the point where they can reproducibly place electrodes around a single dot and many devices are fabricated with low yield. This is particularly true with dots that are randomly distributed on the sample surface, such as self-assembled quantum dots, however some groups have been successful in doing so, yielding interesting results but only on one device (for self-assembled InAs quantum dots see [20–25]). The scalability of the method is not only important for dot characterization but also for potential applications. There are two other scanning probes, the scanning capacitance microscope and scanning single-electron transistor, which can routinely access sub-100 nm length scales and are very sensitive to charge but are not as powerful for mapping out the surface because the probes are much larger than those typically used in STM and AFM.

The scanning capacitance microscope [26] (also called subsurface charge accumulation microscopy) and scanning single-electron transistor [27] were developed around the same time. The scanning capacitance microscope works on the same principles as capacitance spectroscopy, but now the upper plate of the capacitor is a scanning probe which can be moved over the sample surface to locally probe the sample capacitance. It was first demonstrated in 1998 where the charge in a two dimensional electron gas was imaged [26], and in 2008 single electron charging was achieved for semiconductor donor molecules [28]. The scanning single-electron transistor, capable of detecting a fraction of an electron charge, fabricates a single electron transistor

onto the end of a glass probe which is scanned over the sample surface to identify local changes in electric field. It was first demonstrated in 1997 by Yoo et al., when they identified (amoung other things) several individual photo-ionized charge sites in a semiconductor heterostructure [27]. In 2000, the same group observed ring-like shapes in a two-dimensional electron gas which they argued were caused by single electron charging events [29].

The precursor to the AFM, the STM [30] uses the tunneling current between a sharp conductive probe and sample for distance regulation, and to measure sample properties. As the STM requires a current to flow between probe and sample, the samples must be conductive. The first example of an STM measurement showing single electron charging effects in the tunnel current taken over a single particle (in this case an aluminum grain) was accomplished by van Bentum et al. in 1988. In these types of experiments, the STM probe forms a nanoscale tunnel junction with an electrode-tunnel barrier- quantum dot - tunnel barrier (small vacuum gap) - probe configuration. In this way the dot is separated from the electrodes by two tunnel junctions, and so the measurements are fundamentally the same as those using two lithographically defined electrodes. In 1999, STM measurements over single InAs nanocrystals were preformed in this manner. Single electron charging effects were observed, from which the authors could deduce that some of the nanocrystals appeared to have the shell structure of a spherical particle which was expected [31].

The AFM [32] uses a sharp tip attached to a cantilever to measure the changes in the cantilever properties (i.e. change in cantilever deflection, resonance frequency, or oscillation amplitude) caused by tip-sample force interactions, in order to locally characterize the sample. Unlike the STM, the AFM does not require a current to flow between sample and probe and thus does not require conductive samples, making

the AFM a more suitable choice for most samples. Specifically, with reference to measuring the energy levels of single particles, the AFM can analyze buried, or capped, structures, can measure with the cantilever further away from the dot to minimize deformation of the confinement potential, and can measure the tunneling rate of the electrons into the dot for certain conditions. All of these additional abilities are crucial for many practical applications, making the AFM, in most cases, a more suitable tool for measuring the energy levels of quantum dots.

The first demonstration where an AFM was used to detect the single electron charging of a quantum dot was in 2002 by Woodside and McEuen [33]. In this experiment, changes to the cantilever resonance frequency and Q-factor were observed in response to voltage-induced charging of segments of a carbon nanotube (quantum dots) of approximately 1 μm in length. [1] The same research group continued measurements on the carbon nanotube segments and were able to measure the same effects in carbon nanotubes which were not attached to source and drain electrodes [34]. In this work, they also were able to reduce the number of holes confined in the segment so that only a few remained. Later, in 2008, the group attached gold nanoparticles to the nanotubes and measured single electron charging of these nanoparticles. As the nanoparticles had an average diameter of only 12 nm, they were able to observe the charging at 77 K. In this work, they also provided a formula for calculating the tunneling rate of the electrons from the carbon nanotube into the gold nanoparticle. The systems and temperature regime studied by this group

[1] In this article, Woodside and McEuen also were the first to demonstrate scanning gate microscopy where the AFM probe is used as a movable gate over a quantum dot and the current through the dot as a function of the gate voltage revealed single electron charging.

- the micron sized carbon nanotube segments and the 12 nm gold nanoparticles - led to equally spaced charging events which does not reveal the discrete nature of the energy levels of the particle, but merely reflects its overall capacitance. Thus, in the experiments done by this group, shell structure of the quantum dots was not observed and so their theoretical analysis did not include effects caused by degenerate levels [33–37]. It is important to note that in these experiments the charge on the particle was only measured indirectly, i.e. when an electron tunneled between backelectrode and dot. Only by counting the number of "tunneling events" could the number of electrons that had been added/removed from the dot be determined.

A similar study, by Dana and Yamamoto in 2005, measured single electron charging of localized states on the semiconductor surface [38]. They also claimed to have studied uncapped self-assembled quantum dots, but although a figure showing the data is mentioned in the paper, the figure itself is missing. However, they showed AFM constant height amplitude images of GaAs capped self-assembled quantum dots that exhibited faint ring structures which is the signature of this one-by-one electron charging of a dot.

There are two remaining published works in the field which show similar results to each other. Unlike the results from McEuen and Yamamoto, which showed peaks in the spectra and rings in the images, neither of these reports showed peaks probably because the cantilever oscillation amplitude was too large. Although the data presented in both works are convincing, unfortunately they lack the corresponding AFM images which localize the observed charging onto the uncapped InAs quantum dots [39] or the gold nanoparticles [40], which is where they claim the results are originating. Moreover, neither group published control data taken off the dot in order to attribute the observed effect as originating from the dot.

For completeness, there are a few other AFM studies which can measure the electrostatic force arising from a single electron. These reports are impressive, because they have achieved the ultimate in electrical sensitivity. These studies differ from the previous ones in that they are focusing on placing a single charge on the particle and measuring the change in force resulting from that charge, and not on using single electron charging to measure the physical properties of the particle. Obviously, these works are closely related to the aforementioned studies and also to studies of the electrostatic force in general and so it is important to cover them here.

The first report of single electron sensitivity was in 1990 by Schönonberger and Alvarado who reported discrete steps in the electrostatic force which they attributed to the recombination of charges in a region where the surface had been intentionally charged by applying a large bias [41]. Then, in 2001, Klein and Williams showed the detection of single electrons moving from a small metal particle (attached to the tip) into the conductive tip of an oscillating AFM cantilever upon close approach to a sample since this increased the electrostatic field between particle and tip [42]. Distinct oscillations occurred in the cantilever amplitude as each electron left the metal particle, with increasing fluctuation size for each subsequent electron. In this experiment the electrons left the particle based on the proximity of the metal particle to the surface (and the strength of the electric field) and not because of any fundamental property of the particle itself [42]. The same group later identified localized states in thick films of hafnium silicate and silicon dioxide by tunneling single electrons between a conductive AFM tip and a localized state [43]. Although similar to operation as an STM, here only a single electron is transferred between tip and surface every second or so, resulting in currents which are much too low to be measured by STM. The change in the electrostatic force caused by this charge displacement

is detected via AFM techniques [43–45]. Recently, Gross et al. demonstrated the ability of an AFM to not only charge gold or silver adatoms on an NaCl substrate by a single charge, but also the ability to distinguish the charge state of the adatom with single electron resolution [46].

The work by Williams not only demonstrates the sensitivity of AFM, but is also of practical importance as the revealed localized states trap charge, and charge traps degrade electrical device performance. As electronic devices continually shrink in size, it becomes more and more likely that even one of these traps will have a significant influence on its operation. Characterizing these traps is the first step in being able to control them. The ability to characterize electrostatic noise originating from the sample with high spatial resolution is important, yet few studies have been done with AFM. In the later chapters of the thesis, this topic is discussed in more detail.

From these studies, AFM has proven itself as a contender in the field of quantum dot characterization. The combined high spatial resolution and single electron charge sensitivity makes it aptly suited for this field. It is flexible in that it can be used to measure the properties of several types of quantum dots, in particular self-assembled quantum dots, which are being investigated for use as single photo-sources [47], and also for quantum computing for housing spin qubits [48, 49]. In this thesis, we use an AFM for performing energy level spectroscopy on self-assembled InAs quantum dots. Since we are using AFM, we do not need to pattern electrodes onto the sample which simplifies the analysis and ensures that the electrical properties of the dot are not altered by the residue of the patterning process. In addition, we can study several dots in one experiment and image the dot topography in situ for comparison with the dot's electrical properties. We use the same measurement techniques as

the McEuen group, which is a measurement technique unique to resonating charge detectors.

Chapter 2 provides the necessary theoretical background required for understanding the energy level spectrum of a quantum dot, and under what conditions we may be able to measure these levels. Chapter 3 explains the basic principles of the AFM modes of operation that were used in this thesis. Chapter 4 contains some data and analysis pertinent to the study of quantum dot energy levels. Chapter 4 also contains examples of how the electrostatic background affects the quantum dots. In Chapter 5, one method that we have used to characterize the electrostatic background is presented. In particular, we induced charge noise on the sample via super bandgap laser irradiation and measured the generation-recombination noise of the charge pairs. Chapter 6 starts with a plan for the next set of experiments and summarizes the basic conclusions of the thesis.

CHAPTER 2

Theoretical Background

2.1 Quantum Dot Physics

Semiconductor quantum dots confine electrons into volumes with dimensions on the order of a few to tens of nanometers. The confinement of the electron wavefunction is on the order of the size of the dot which leads to a discrete spectrum of energy levels within the dot (shell structure). The shape of the confinement potential can lead to degeneracies amongst these discrete energy levels. Since this is also the case for atoms, quantum dots are sometimes referred to as "artificial atoms" [50].

The Coulomb repulsion from the electrons confined within the quantum dot results in an energy barrier that must be exceeded in order to add an additional electron to the dot, called the charging energy, E_C:

$$E_C = \frac{e^2}{2C_\Sigma} \tag{2.1}$$

Where e is the electron charge, and C_Σ is the total capacitance of the dot which is equal to the sum of the capacitances between the dot and all other conductors. In our setup these are the tip-dot and dot-2DEG capacitances [i.e. $C_\Sigma = C_{tip} + C_{sub}$

in Fig. 2–1)(b)]. The charging energy gives us an estimate of the size of the dot by assuming some shape of the dot and calculating the capacitance for such a dot knowing C_Σ. For example, the capacitance of a flat disk with radius R is a decent approximation of the shape of our quantum dots which are wide but short. This capacitance is proportional to dot radius, i.e. $C_{disk} = 8\epsilon_0\epsilon_r R$ for ϵ_r the dielectric constant of the surrounding material [3]. It is clear then, from Eq. 2.1, that smaller dots have larger E_C and vice versa. Under certain conditions, the value of E_C can be large enough to suppress tunneling of electrons onto the dot, keeping the number of electrons on the dot constant, this is called Coulomb blockade.

2.1.1 Coulomb Blockade

The two required conditions for Coulomb blockade are very intuitive: the electrons must not have enough thermal energy to overcome the charging energy (i.e. $E_C \gg k_B T$), and the electron wavefunctions must be well localized on the dot, making the number of electrons on the dot well defined (i.e. the tunnel junction resistance, R_T, must be large: $R_T \gg \frac{h}{e^2} \simeq 25.8\text{k}\Omega$ [1]) [3,52]. If the quantum dot is in a Coulomb blockade state, tunneling into the dot is suppressed and no charge can be added or removed from the dot. The term originated from transport measurements through a dot between two conductive leads, when oscillations in the conductance occured as a nearby gate voltage was varied. When tunneling was suppressed the conductance was low, and the current between source and drain was "blockaded." [51]

[1] The lower bound of h/e^2 comes from the Heisenberg uncertainty principle. $\Delta E_C \Delta t > h$ for $\Delta t = R_t C$ as the time it would take to charge/decharge the dot-2DEG capacitor [3,51].

Experimentally, the two conditions for observing Coulomb blockade are met by carrying out the experiments at a sufficiently low temperature and by having a sufficiently opaque tunneling barrier between the dot and electron reservoir. Fig. 2–1 (a) and (b) shows a schematic of our experimental setup and an equivalent circuit diagram. It so happens that our experimental configuration forms the simplest type of circuit that can be used to measure Coulomb blockade in a quantum dot as the dot is coupled to only one tunnel junction. This type of configuration is given the name *single electron box*. In Fig. 2–1(a) the cantilever is positioned above a single quantum dot. The vacuum gap between tip and dot forms a capacitor, and the dot and 2DEG are separated by an InP tunnel barrier. As the energy barrier formed by the vacuum gap is much larger than that formed at the semiconductor interfaces, tunneling occurs through the InP and not the vacuum gap and so a tunnel barrier is indicated in this region of the equivalent circuit [Fig. 2–1(b)].

Fig. 2–1(c) shows the band diagram of our sample at negative V_B. The quantum dot depicted in the band diagram has well spaced energy levels to represent both the charging energy and the possibility of observing the shell separation, ΔE. An electron will only tunnel into the dot when the electrochemical potential of the electrons in the 2DEG overlaps a dot level. We assume a constant and continuous density of states for the 2DEG so that the electrons populate these states according to the Fermi-Dirac distribution:

$$f(E) = \frac{1}{1 + e^{\frac{E}{k_B T}}} \tag{2.2}$$

where T is the temperature, k_B is the Boltzmann constant, $E = \mu_{dot} - \mu_{2DEG}$, and μ_{dot} and μ_{2DEG} are the chemical potentials of the quantum dot and the 2DEG. If we consider a single, non-degenerate dot level, tunneling into and out of the dot (with

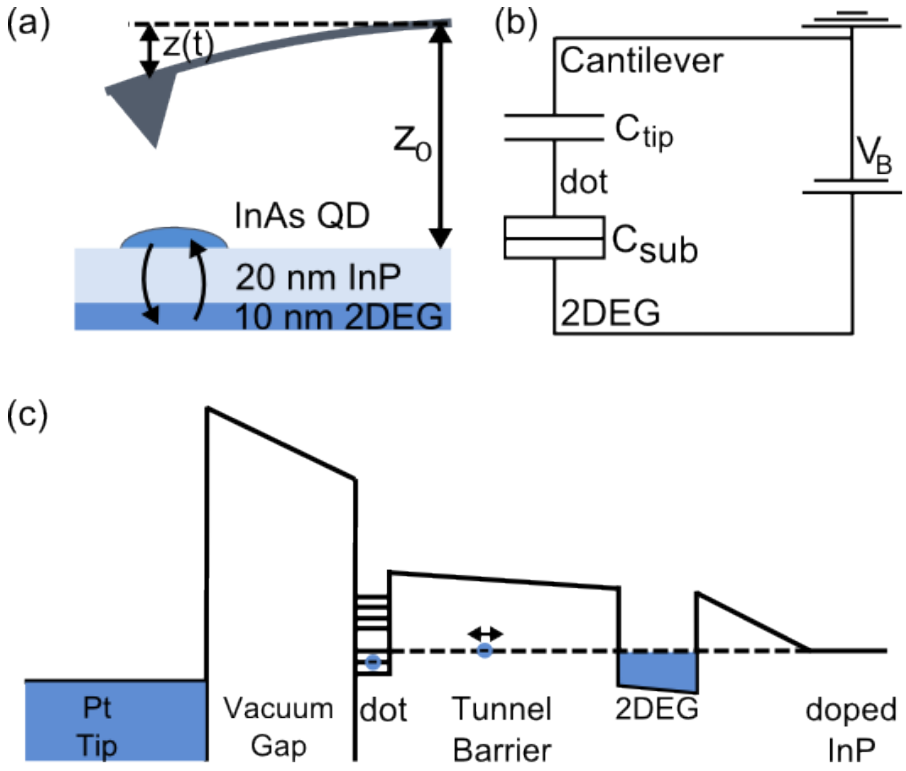

Figure 2–1: (a) A schematic of the sample setup showing the oscillating cantilever (with pyramidal tip) above a quantum dot. Arrows indicate the path taken by tunneling electrons. (b) Equivalent circuit diagram of setup. (c) Band diagram of sample with a negative V_B applied. [53]

tunneling rate Γ) will be maximal when $E = 0$, called a *charge degeneracy point* since both n and $n+1$ electrons on the dot are energetically equal. This occurs when $\mu_{dot} = \mu_{2DEG}$. An electron tunnels from the 2DEG into the dot with the rate Γ_+ and out with Γ_-.

$$\Gamma_+ = \Gamma f(E) \tag{2.3}$$

$$\Gamma_- = \Gamma[1 - f(E)] \tag{2.4}$$

There are two regimes of Coulomb blockade, *classical* and *quantum*, based on whether or not the ΔE spacing is resolvable. In the *classical* regime, several discrete energy levels of the quantum dot overlap the Fermi-Dirac distribution of reservoir electrons, such that $E_C \gg k_B T \gg \Delta E$. In this regime, tunneling events occur with periodicity E_C. In contrast, in the *quantum* regime only one discrete energy level overlaps with the Fermi-Dirac distribution of the reservoir since the separation of the next higher level is larger than the thermal broadening of the reservoir states, i.e. $E_C \geq \Delta E \gg k_B T$.

2.2 Cantilever Dynamics

In atomic force microscopy the detected forces interact with a micro-fabricated cantilever and, since the pyramidal tip mounted on the free end is more than 10 μm long, more substantially with the end of the tip [54]. There are a wide variety of cantilevers commercially available which are tailored to either the mode of operation or the type of sample to be studied. AFM relies on the change in the mechanical state of the cantilever (deflection, resonance frequency, dissipation/damping, or oscillation amplitude) resulting from the tip-sample interaction as a feedback mechanism

to regulate tip-sample distance, and so the cantilever plays an integral role in the experiment.

As the typical oscillation amplitude is on the order of tens of nanometers, there are billions of quanta stored in the cantilever and so it is treated it as a classical oscillator.[2] The equation of motion of the driven and damped cantilever with a single degree of freedom is:

$$m\ddot{z}(t) + m\gamma_0\dot{z}(t) + m\omega_0^2 z(t) = F_{drive}(t) + F_{ts}[z(t), \dot{z}(t)] \tag{2.5}$$

Where the intrinsic cantilever properties m, ω_0, and $\gamma_0 = \omega_0/Q_0$ are the effective mass, resonance frequency, and damping coefficient (due to phonons, thermoelasticity, surface coatings, etc.). The intrinsic properties of the cantilever can be determined for a specified temperature and pressure far away from the sample surface (where sample interaction forces, F_{ts}, are negligible). Q_0 is the quality factor of the cantilever, also measured far from the sample. The free end of the cantilever oscillates with position $z(t)$ in time t. Although the AFM can be operated in the *static deflection mode* [32] (where the cantilever is not driven into oscillation, i.e. $F_{drive} = 0$, and the $\Delta z = -F_{ts}/k$ for spring constant k and cantilever deflection Δz), only *dynamic mode* AFM [56] was used in this thesis and in this mode the cantilever is oscillated with nearly sinusoidal oscillations of amplitude a and frequency ω_d so

[2] Since $\hbar\omega_0 \ll k_B T$ the cantilever is not a quantum oscillator. For the type of AFM cantilevers that we use, the cantilever would need to be oscillating with amplitudes of approximately 10^{-20} m in order for quantum mechanical effects to come into play. This value is calculated from the standard quantum limit for an oscillator, $\Delta x = \sqrt{\frac{\hbar}{2m\omega_0}}$, where the definitions for the variables can be found following Eq. 2.5 [55].

that $z(t \gg 0) \simeq a\cos(\omega_d t)$. [3] Although $F_{ts}(z)$ is non-linear, causing deviations to the harmonic motion of the cantilever, under normal operation small oscillation amplitudes relative to the change in force-gradient ensure this assumption is justified [57]. The cantilever is driven into oscillation by F_{drive}, which is applied to the cantilever via a piezoelectric actuator underneath the cantilever chip. The form of F_{drive} depends on the type of AFM mode used.

2.2.1 Frequency Modulation Mode AFM

Although a more general overview of the types of AFM operation modes is given in Chapter 3, here we discuss the two relevant modes of operation used herein to provide the form of F_{drive}. We typically use only two types of dynamic mode AFM: constant excitation [56], and frequency modulation [58] or self-oscillation mode. Constant excitation mode uses $F_{drive} = F_d\cos(\omega_d t)$ so that the solution to Eq. 2.5 is $z(t \gg 0) \simeq a(\omega_d, F_d)\cos[\omega_d t + \theta_0(\omega_d, F_d)]$ for drive oscillation frequency, ω_d and drive amplitude F_d. Since the oscillation amplitude, a, is a function of F_{ts} it can be used in a feedback loop for distance control. The phase shift between cantilever deflection and drive signals, θ, although also a function of F_{ts}, is not generally used for distance regulation as that signal saturates more quickly than a.

We use the constant excitation mode to determine the Q_0 and ω_0 of the cantilever when the tip-sample gap is very large so that tip-sample interactions are negligible. A resonance curve of the cantilever is obtained by measuring the oscillation amplitude while sweeping the driving frequency. The maximum amplitude of this curve occurs at ω_0 and the full width at $1/\sqrt{2}$ of the maximum amplitude, $\Delta\omega_d^{FWRHM}$ (with

[3] Whether $\omega_d = \omega$ or $\omega_d = \omega_0$ depends on the type of dynamic mode. Where $\omega = \omega_0 + \Delta\omega$ and $\Delta\omega$ is a change in the resonance frequency from ω_0.

FWRHM standing for full width at root half max), describes the quality factor: $Q_0 = \omega_0/\Delta\omega_d^{FWRHM}$. The oscillation amplitude resonance curve and phase response of the oscillator are given by:

$$a = \frac{F_d}{k}\frac{\omega_0^2}{\sqrt{(\omega_0^2 - \omega_d^2)^2 + (\omega_d\omega_0/Q_0)^2}} \tag{2.6}$$

$$\tan(\theta_0) = \frac{1}{Q_0}\frac{\omega_d\omega_0}{\omega_0^2 - \omega_d^2} \tag{2.7}$$

From Eq. 2.6 it is clear that the maximal amplitude occurs at $\omega_d = \omega_0$, and in this condition Eq. 2.7 shows that the phase difference between the drive and cantilever deflection is 90^o. This is a phase lag so that the cantilever velocity is in phase with the driving frequency.

In self-oscillation mode, $F_{drive} = G_d z(t - t_0)$ where G_d is the driving gain applied to the position detection signal at retarded time $t - t_0$. The time t_0 is manually adjusted by a phase shifter at the beginning of the experiment in order to minimize G_d for a set oscillation amplitude. Ideally, this corresponds to a phase lag of 90^o between the cantilever deflection and drive signals and so we use this value to simplify the analysis.[4] More details on how to operate the AFM in self-oscillation mode are given in Section 3.3, which includes a block-diagram of the self-oscillation mode feedback loop (Fig. 3–4).

[4] Ref. [59] found that a large detuning of approximately 20% in the phase lag resulted in only a 0.002% error in the frequency shift and 6% in the dissipation.

2.2.2 The Tip-Sample Interaction Force

Tip-sample interactions arising from attractive forces cause the cantilever beam to soften, leading to a negative frequency shift of the cantilever. For example, if the force gradient is constant over the oscillation cycle then the change in resonance frequency is [60]:

$$\Delta\omega = \frac{\omega_0}{2k} k_{ts} = -\frac{\omega_0}{2k}\frac{\partial F_{ts}}{\partial z}. \tag{2.8}$$

Although this restraint is generally not strictly met, Eq. 2.8 serves to demonstrate that an attractive F_{ts} leads to a negative shift in resonance frequency by $\Delta\omega$. The cantilever resonance frequency can be measured and used for distance regulation by a feedback loop.

We can obtain F_{ts} as a function of tip-sample separation, z_0, for most types of forces by measuring the $\Delta\omega(z_0)$ using self-oscillation mode. Again assuming sinusoidal motion of the cantilever, $z(t) = a\cos(\omega t)$, the driving force becomes $F_{drive} = F_d \sin(\omega t)$ and we can use Fourier analysis to obtain a solution to Eq. 2.5 [57]:

$$\frac{\Delta\omega}{\omega_0} = -\frac{1}{ak}\frac{1}{T}\int_0^T F_{even}(z_0 + z(t))\cos(\omega t)dt \tag{2.9}$$

$$F_d + am\gamma_0\omega = \frac{2}{T}\int_0^T F_{odd}(z_0 + z(t))\sin(\omega t)dt \tag{2.10}$$

Where T is the temperature, k is the spring constant[5] , $\omega = \omega_0 + \Delta\omega$, and $F_{ts} = F_{even} + F_{odd}$.

[5] Here, the spring constant is actually referred to as the dynamic spring constant, which depends on which type of oscillation mode is used. However, if we are only oscillating the cantilever at its fundamental mode, it is a good approximation to use the static spring constant. [57]

In order to carry this analysis further, we require both F_{even} and F_{odd} to be uniquely defined for all tip-sample gaps, z_0 (i.e. the force measured during cantilever approach and retraction have the same value for the same z_0) [57]. Although this is satisfied for F_{even}, it is not the case for F_{odd}. This can be remedied by describing $F_{odd} = \gamma_{gen}(z_c, a, \omega, z(t))\dot{z}_c(t)$. To simplify the notation, we used $z_c = z_0 - a$ to describe the distance of closest approach. "The generalized damping coefficient" γ_{gen} is an even function and $\dot{z}_c(t)$ obviously an odd function since we approach and then retract from the sample. This expression exactly represents F_{odd}. Provided that both F_{even} and $\Delta\gamma_{gen}$ (which is the change in γ_{gen} resulting from F_{ts}) are unique functions of tip-sample gap and that $F_{ts} \to 0$ for infinite tip-sample gap then $F_{ts} = F_{even} + F_{odd}$ can be determined [57]:

$$F_{even}(z_c) = 2k \int_{z_c}^{\infty} \left[\left(1 + \frac{a^{\frac{1}{2}}}{8\sqrt{\pi(t - z_c)}} \right) \Omega(t) - \frac{a^{\frac{3}{2}}}{\sqrt{2(t - z_c)}} \frac{d\Omega(t)}{dt} \right] dt \tag{2.11}$$

$$\Delta\gamma_{gen}(z_c) = -m\gamma_0 \frac{\partial}{\partial z_c} \int_{z}^{\infty} \left[\left(1 + \frac{a^{\frac{1}{2}}}{8\sqrt{\pi(t - z_c)}} \right) \Theta(t) - \frac{a^{\frac{3}{2}}}{\sqrt{2(t - z_c)}} \frac{d\Theta(t)}{dt} \right] dt \tag{2.12}$$

where

$$\Omega(z_c) = \frac{\Delta\omega(z_c)}{\omega_0} \tag{2.13}$$

$$\Theta(z_c) = \frac{\Delta F_d(z_c)}{\bar{F}_d} - \frac{\Delta\omega(z_c)}{\omega_0} \tag{2.14}$$

The fractions $\frac{\Delta F_d(z_c)}{F_d}$ and $\frac{\Delta\omega(z_c)}{\omega_0}$ are measured experimentally; the former from the drive signal required to maintain a preset oscillation amplitude recorded by the automatic gain controller (AGC), and the latter is measured by the PLL. Using Eq. 2.11-Eq. 2.14 we are able to extract the F_{ts} caused by tip-sample interactions [57].

2.2.3 Dissipation Measurements

In order to sustain the cantilever oscillations with constant amplitude (greater than that achievable by thermal oscillation alone), the cantilever must be continually driven. The driving signal required to maintain a constant amplitude is what the AFM community refers to as a *dissipation* signal. Damping processes increase the dissipation. The energy loss per oscillation cycle is [61]:

$$E_{ts} = E_o\left[\frac{A_{exc}}{A_{exc0}} - \frac{\omega}{\omega_o}\right] \approx E_o\left[\frac{A_{exc} - A_{exc0}}{A_{exc0}}\right]. \tag{2.15}$$

where A_{exc} is the excitation signal and A_{exc0} is the intrinsic or background dissipation. The fraction ω/ω_o is the dynamic resonance frequency compared to the reference taken at $F_{ts} = 0$, and is approximately equal to 1 in self-oscillation mode since the shift in resonance frequency is small compared to ω_0. $E_o = \frac{\pi k a^2}{Q_0}$ is the intrinsic loss of energy per oscillation cycle (i.e. for $A_{exc} = 0$ in Eq. 2.15).

To get a feel for the origin of the damping, consider the following force $F_{ts} = F_{ts0}(z(t-\tau))$ which is applied to the cantilever after some lag time τ. In our system, this lag time is the tunneling rate of the quantum dot. If we assume small z and τ [6] , and Taylor expand F_{ts}, and insert the result into Eq. 2.5, then we obtain:

[6] This is not necessarily a valid approximation (i.e. $\Gamma \gg \omega$) in systems like ours where the cantilever resonance frequency is similar to the tunneling rate, however it is nevertheless instructive in demonstrating the origin of the observed dissipation.

$$m\ddot{z} + m\gamma_0\dot{z} + m\omega_0^2 z \approx F_{drive} + F_{ts0} + \frac{\partial F_{ts}}{\partial z}(z - \tau\dot{z}). \tag{2.16}$$

The force F_{ts} has now been decomposed into 3 parts: a constant term, a term linear in z, and a term linear in $\dot{z}$. By comparison with the left hand side of Eq. 2.16 we observe that F_{ts} has led to a change in the damping coefficient and spring constant, which corresponds to a change in dissipation and resonance frequency shift. Although a more rigorous derivation to describe the damping is provided later, this example highlights that in our system the observed dissipation results from a time lag between cantilever motion and force.

2.3 Conservative Forces

There are several types of tip-sample interaction forces that can be measured using AFM, for example the van der Waals, magnetic, adhesion, frictional, repulsive and electrostatic force. Since we work under vacuum at low temperature, on non-magnetic samples in the non-contact mode, we are interested only in the van der Waals and electrostatic forces, since both are long-ranged.

2.3.1 Repulsive forces

Only a brief explanation of the short-ranged repulsive forces will be covered here because in general the cantilever was kept out of the repulsive force regime in the experiments reported. However, for spectra where the cantilever is approached towards the sample, the repulsive regime is used to define where the tip-sample gap is zero. Using self-oscillation mode, we define the zero gap where the oscillation amplitude is only 95% of its free value, and at this separation the cantilever will be in the repulsive force regime. Empirical equations are used to model the potential which quickly rises monotonically at small gaps. For example, the Inverse Power-Law

Potential is given as $U(z_0) = (\sigma/z_0)^n, n\epsilon I$, for hard-sphere diameter σ [62]. From the potential, the force can be calculated via: $F = -dU/dz_0$.

2.3.2 Van Der Waals Force

The long ranged, usually attractive, van der Waals force arises from the dipole-dipole interactions between the atoms of the sample and cantilever tip, and are described by F_{vdW} [62]:

$$F_{vdW} \simeq -\frac{C_H R}{6 z_0^2} \tag{2.17}$$

for a spherical tip of radius R, and tip-sample gap z_0 ($z_0 \ll R$). In vacuum, the Hamaker's constant, H, is approximately 10^{-19}J. [7] C_H is not strictly constant with tip-sample separation as retardation effects arise based on how efficiently the dipoles are able to couple and this becomes more difficult at larger separations since the coupling is not instantaneous. At larger tip-sample separation ($z_0 \gg R$), this effect can be partly accounted for by a more rapidly decaying force, now by a factor of $1/z^3$ [64]. The magnitude of this force at $z_0 = 10$ nm tip-sample separation, $R = 5$ nm, and $C_H = 10^{-19}$ J, is approximately 1 pN.

2.3.3 Electrostatic Force

As in a capacitor, the electrostatic force in our system arises from the attraction between plates separating opposite charges. Here, the plates of the capacitor consist of the conductive cantilever (usually a commercially purchased semi-conducting

[7] Depending on the value of the dielectric constants for the tip, sample, and immersion medium, C_H can be negative, making the van der Waals force repulsive. Ref. [63] describes an experiment where this was shown with AFM.

cantilever is sputter coated with a metallic layer) and the sample. The sample can be completely conductive, or a backelectrode layer can be topped with insulating or semi-conducting layers. Due to the long-ranged nature of the electrostatic force, the voltage applied between tip and backelectrode can be used to probe the electrostatic properties of these layers. If the tip and sample form a capacitor, C, having a charge of $|q|$ on each plate, then the energy of the system is $U = \frac{1}{2}q^2/C$. The electrostatic force, which includes the work done by the battery to maintain the charge on the plates, is then:

$$F_{elec}(\Delta V, z_0) = \frac{1}{2}\frac{\partial C}{\partial z_0}\Delta V^2 \tag{2.18}$$

The voltage, ΔV, dropped between the cantilever and sample is $\Delta V = V_B - V_{CPD}$, where V_B is the tip-sample bias voltage and V_{CPD} is the contact potential difference between them.

To compare the magnitude of the electrostatic force to the van der Waals force, we use the calculation by Hudlet et al. [65] for the electrostatic force between a conductive sphere and plane, $F_{elec} = \pi\epsilon_0(\frac{R^2}{z_0(z_0+R)})V^2$, for a tip of radius $R = 5$ nm, tip-sample separation $z_0 = 10$ nm, and $\epsilon_0 = 8.85 \times 10^{-12}\mathrm{m}^{-3}\mathrm{kg}^{-1}\mathrm{s}^4\mathrm{A}^2$. For $V = 1$ V, the $F_{elec} \approx 5$ pN.

2.4 Nonconservative And Conservative Forces Of Single-Electron Tunneling

In the previous section the forces were distance dependent and so respond in-phase with the oscillatory motion of the cantilever. Now we consider the force exerted by the single electron tunneling between dot and 2DEG. Since the electron has a lifetime on the dot, these forces are not necessarily in phase with the cantilever motion and then these forces damp the cantilevers' motion.

In the Coulomb blockade regime, the charge on the dot is fixed and the tunnel barrier can be treated as a capacitor so that the equivalent circuit can be analyzed. Using the notation of Fig. 2–1(b), the sum of the energy stored in the two capacitors is:

$$U = \frac{q_{sub}^2}{2C_{sub}} + \frac{q_{tip}^2}{2C_{tip}} = \frac{q^2}{2C_\Sigma} + \frac{1}{2}\frac{C_{sub}C_{tip}}{C_\Sigma}V_B^2 \tag{2.19}$$

Where q_{sub} and q_{tip} are the charges on the capacitors formed by the tunnel barrier and the tip-dot, respectively, and $q = q_{sub} - q_{tip} = -n\,|e|$ is the charge on the dot. The latter form of the energy consists of the charging energy of the dot and the energy stored in the capacitors which are connected in series [66]. In order to describe the free energy of the system, the work done by the battery to maintain the voltage on the capacitors, W, needs to be subtracted from the energy stored in the capacitors.

$$W = \int_0^{q_{tip}} V_B dQ = q_{tip}V_B = \frac{C_{sub}C_{tip}}{C_\Sigma}V_B^2 + q\frac{C_{tip}}{C_\Sigma}V_B \tag{2.20}$$

The free energy of the system describing a dot coupled to a cantilever of small oscillation amplitude is then $H = U - W$:

$$H = \frac{q^2}{2C_\Sigma} - q\frac{C_{tip}}{C_\Sigma}V_B - \frac{1}{2}\frac{C_{sub}C_{tip}}{C_\Sigma}V_B^2 \tag{2.21}$$

From Eq. 2.21 we can get the electrostatic force from the charge on the dot [39]:

$$F_{elec}(z_0) = \frac{1}{2}\frac{\partial C_{series}}{\partial z_0}\left(V_B + \frac{q}{C_{sub}}\right)^2. \tag{2.22}$$

Where $C_{series} = \frac{C_{tip}C_{sub}}{C_\Sigma}$. Compare Eq. 2.22 to Eq. 2.18 and notice that the charge on the dot is going to shift the apex of the parabola which describes the force. In our measurements, we are not able to resolve the change in electrostatic force

through the addition of a single electron onto the dot. This measurement is difficult because of the large electrostatic background between the tip and 2DEG, making it difficult to isolate a single charge. In 2009, Gross et al. were able to distinguish a change of a single electron charge on gold adatoms in the frequency shift of the cantilever, resulting from a change in force of a few piconewtons [46]. Differences between microscopes aside, it would be more difficult to measure the addition of a single charge to the quantum dot since it is much larger than a gold atom and so the electron wavefunction is spread out over a larger area.

To show how the force caused by the electron tunneling is measured in the cantilever resonance frequency and cantilever dissipation, we first rewrite Eq. 2.21 into a form that includes the charging energy, E_C, of the dot [67]:

$$H = E_C[(n - \mathcal{N})^2 - (1 + \frac{C_{sub}}{C_{tip}})\mathcal{N}^2] \tag{2.23}$$

Where $\mathcal{N} = -\frac{C_{tip}V_B}{e}$ is the number of electrons that would be on the dot if the number, n, was not restricted to being an integer. The first term determines the periodicity of the Coulomb blockade oscillations, but we are only considering one dot energy level here and so E_C is written as a constant. However, to extend this to a more general notation, each electron can have a different E_C and the total Hamiltonian would be a sum over all of the levels of the dot [67]. The second term describes the capacitive coupling of the cantilever to the dot.

The magnitude of the cantilever oscillation amplitude provides two regimes for studying the quantum dot energy levels. In the *weak coupling* regime cantilever and dot are considered weakly coupled and the cantilever motion is small enough that during one oscillation cycle the cantilever does not swing the dot level completely on/off the charge degeneracy point so that the Coulomb blockade peak linewidth is

thermally broadened [67]. Conversely, in the *strong coupling* regime, the motion of the cantilever during one oscillation cycle affects the dot, namely by modifying the electron add/remove rate. Since the cantilever motion is now large enough to swing the dot level on/off the charge degeneracy point during one oscillation cycle, the peaks are broadened by the oscillation [53]. In order to be in the strong coupling regime, $Aa \gg k_BT$ where Aa and k_BT are approximately the Coulomb blockade peak widths for the oscillation broadened and thermally broadened peaks, respectively. These two regimes need to be treated separately theoretically, however experimentally the transition between these two regimes is gradual. First we will go through the main steps of the weak coupling theory, and obtain an expression describing the resonance frequency shift and dissipation of the cantilever. Afterwards we will take a look at the strong coupling theory.

2.4.1 Weak Coupling For A Non-Degenerate Level

When the coupling between cantilever and dot is weak, linear response theory can be used to derive an expression for the frequency shift and dissipation experienced by the cantilever when an electron is tunneling [67,68]. The motion of the cantilever during an oscillation cycle is considered to be small enough that the system responds linearly to the change and higher order terms can be neglected. Since $C_{tip}(z)$ is the only variable that is a function of cantilever tip position in Eq. 2.23, we Taylor expand it and replace C_{tip} everywhere in Eq. 2.23 with the expanded version and focus on the terms that are both linear in z and depend on the number, n, of electrons on the level (i.e. $n = 0$ or $n = 1$ since we are only considering one level). We find this term is [67]:

$$H_{int} = -Anz. \tag{2.24}$$

Where A is:

$$A = -2E_C \frac{V_B C_{sub}}{e(C_{tip} + C_{sub})} \frac{\partial C_{tip}}{\partial z}, \tag{2.25}$$

and describes the dot-cantilever coupling strength for a given occupation level in the dot (since E_C is different for each peak). The form of H_{int} describes a force (i.e. $H_{int} = Fz$) exerted on the cantilever which fluctuates with n according to whether or not the level is occupied. This force can be decomposed into a sum of an in-phase and out of phase component with respect to the cantilever motion, giving a conservative and damping force respectively [68].

$$f_{damping}(t) = -m \int_{-\infty}^{\infty} dt' \Delta\gamma(t - t')\dot{z}(t'), \tag{2.26}$$

$$f_{conservative}(t) = \frac{2k_0}{\omega_0} \int_{-\infty}^{\infty} dt' \Delta\omega(t - t')z(t'), \tag{2.27}$$

Using linear response theory, we can obtain expressions for the frequency shift, $\Delta\omega$, and dissipation, $\Delta\gamma$, lineshape measured by the cantilever, by solving for the linear response coefficient λ_F since [68]:

$$\frac{k_0}{\omega_0}^2 \Delta\gamma(\omega) = -A^2 \left(\frac{-\mathrm{Im}\lambda_F(\omega)}{\omega} \right) \tag{2.28}$$

$$\frac{2k_0}{\omega_0} \Delta\omega = A^2[-\mathrm{Re}\lambda_F(\omega)]. \tag{2.29}$$

To do so, we look at the probability that a level is occupied while this level is oscillating with respect to the states of the 2DEG as a consequence of the oscillating cantilever [67]. Let p_0 be the probability that the level is empty and p_1 be the probability that the level is occupied. These probabilities satisfy master equations:

$$\frac{\partial p_0}{\partial t} = -\Gamma_+ p_0 + \Gamma_- p_1 \tag{2.30}$$

$$\frac{\partial p_1}{\partial t} = \Gamma_+ p_0 - \Gamma_- p_1. \tag{2.31}$$

The probabilities p_0 and p_1 are related through $p_0 + p_1 = 1$ and so we can substitute Eq. 2.30 into Eq. 2.31 and vice versa and, by using equations Eq. 2.3 and Eq. 2.4 for Γ_+ and Γ_-, obtain the stationary solutions which provide $p_0 = 1 - f(E)$ and $p_1 = f(E)$. By assuming that the oscillating cantilever causes the difference in chemical potentials between dot and 2DEG to also oscillate, $E \to E + \delta e^{(-i\omega t)}$, then the probabilities will oscillate:

$$p_1 \to p_1 + \lambda_F(\omega)\delta e^{(-i\omega t)} \tag{2.32}$$

$$p_0 \to p_0 - \lambda_F(\omega)\delta e^{(-i\omega t)} \tag{2.33}$$

Substituting equations Eq. 2.32 and Eq. 2.33 into Eq. 2.30 and Eq. 2.31 and linearizing in δ we can solve for $\lambda_F(\omega)$ and using Eq. 2.28 and Eq. 2.29 to solve for the resonance frequency shift, $\Delta\omega$, and dissipation, $\Delta\gamma$ [67].

$$\Delta\omega = -\frac{\omega_0}{2k_0}\frac{A^2\Gamma^2}{k_B T}\left[\frac{1}{\omega^2 + (\Gamma)^2}\right] f(1-f). \tag{2.34}$$

$$\Delta\gamma = \frac{\omega_0^2 A^2 \Gamma}{k_0 k_B T}\frac{1}{\omega^2 + \Gamma^2} f(1-f), \tag{2.35}$$

The magnitude of Eq. 2.34 and Eq. 2.35 as a function of ω/Γ (with normalized units) is shown in Fig. 2–2 [37]. As long as the cantilever resonance frequency is less

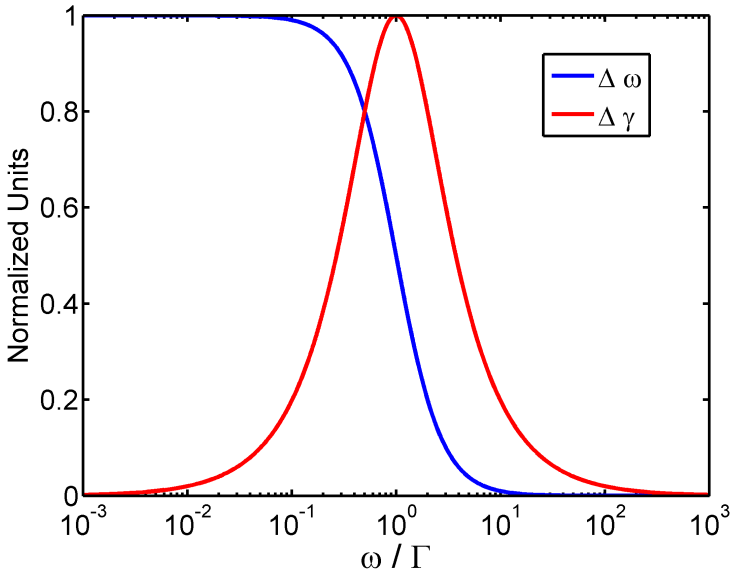

Figure 2–2: Plot of the dissipation and resonance frequency shift response versus ω/Γ with normalized units using Eq. 2.34 and Eq. 2.35.

than the tunneling rate, then a change in resonance frequency can be observed. Conversely, the dissipation response is maximal when the tunneling rate and resonance frequency are nearly equal, and falls off quickly for every order of magnitude away from equality. This plot highlights a challenge of this technique: the ω/Γ ratio is going to affect the signal, and since Γ is inherent to the sample, we want to have easy access to cantilevers with high Q and the appropriate ω_0 but this is not currently aways possible.

In addition we are also provided with an expression for the tunneling rate (or lifetime on the dot) of the electron [37, 68]:

$$\Gamma = -2\omega_0 \frac{\Delta\omega}{\Delta\gamma}, \tag{2.36}$$

Although the above equations for the frequency shift, dissipation and tunneling rate of the electrons fit our data taken with a small oscillation amplitude very well, they

could not describe the results observed for larger amplitude oscillations nor for a shift in the Coulomb blockade peak as a function of temperature. By allowing for degeneracy in the levels (which we had reason to believe was the case from the peak spacing in the electron addition spectra in combination with observed level degeneracies in InAs dots [18, 19, 21, 69]), we were ultimately able to account for these observations.

2.4.2 Weak Coupling For A Degenerate Level

In order to include degeneracy into the above analysis, the Master equations and probabilities have to be modified to include the disparity between the number of ways an electron can be added to the shell (this is equal to the number of unoccupied degenerate levels before adding the electron) and the number of ways to remove an electron (this is equal to the number of occupied degenerate levels after the electron has been added). Following the same procedure used above for a single, non-degenerate level, we can now obtain the resonance frequency shift, dissipation and tunneling rate for an electron tunneling into a shell with degenerate levels [67]:

$$\Delta\omega = -\frac{\omega_0}{2k_0}\frac{A^2\Gamma^2}{k_BT}\left[\frac{(n_{Shell}+1)(\nu-n_{Shell})}{\omega^2+(\phi\Gamma)^2}\right]f(1-f). \tag{2.37}$$

$$\Delta\gamma(V_B) = \frac{\omega_0^2 A^2\Gamma}{k_0 k_B T}\frac{(n_{\rm shell}+1)(\nu-n_{\rm shell})}{\omega^2+(\phi\Gamma)^2}\frac{f(1-f)}{\phi}, \tag{2.38}$$

$$\phi\Gamma = -2\omega_0\frac{\Delta\omega_{\rm dip}}{\Delta\gamma}, \tag{2.39}$$

where $\phi = (\nu - n_{shell})f(E) + (n_{shell}+1)(1-f(E))$. We refer to ϕ as the *degeneracy factor*. The number of electrons already in the shell before adding a new electron is n_{shell}, and ν is the number of degenerate levels in the shell.

Taking the derivative of $\Delta\omega$ and $\Delta\gamma$ as a function of E reveals the maximum in peak amplitude is a function of T, Γ, n_{shell}, and ν, where Γ,n_{shell}, and ν are fixed for a given level. Each peak position thus has a unique temperature dependence which can be used to identify the degeneracy within the shell, and we can observe the shift of the peak along the energy axis with temperature. The degeneracy is responsible for these shifts since an offset between dot and 2DEG energy alignment balances the rates to add and remove electrons, and this maximizes tunneling thereby defining the peak center [67]. This concept is depicted in Fig. 2–3. The gray region on the right of each image represents the Fermi-Dirac population of the 2DEG, the black dots are electrons already occupying a level, the white dots are electrons that will be added to the level, and the dashed line is where maximal tunneling would occur for a single, non-degenerate, dot level. An asymmetry between the number of ways to add and remove electrons, emphasized by the arrows, shifts the location of the peak maximum. Fig. 2–3(a)-(b) shows an example of a shell having two electrons, where the first electron is about to be added (a) and then the second in Fig. 2–3(b). There are two ways to add the electron in Fig. 2–3(a), but only one way to remove it, while for Fig. 2–3(b) we have the opposite case with only one way to add an electron and two ways to remove it. This causes the peaks of the first and second electrons to move away from each other along the energy axis. The scenario for peaks 3 through 6 are depicted in Fig. 2–3(c-f). Once again the first half of the peaks (now peak 3 and peak 4) shift in one direction and the second half (peak 5 and 6) are shifted in the opposite direction with increasing temperature. The two main features of Eq. 2.38 that Fig. 2–3 highlights are: the peaks shift away from the center of the shell (the first half of the peaks shift one way and vice versa) and the magnitude of the shift

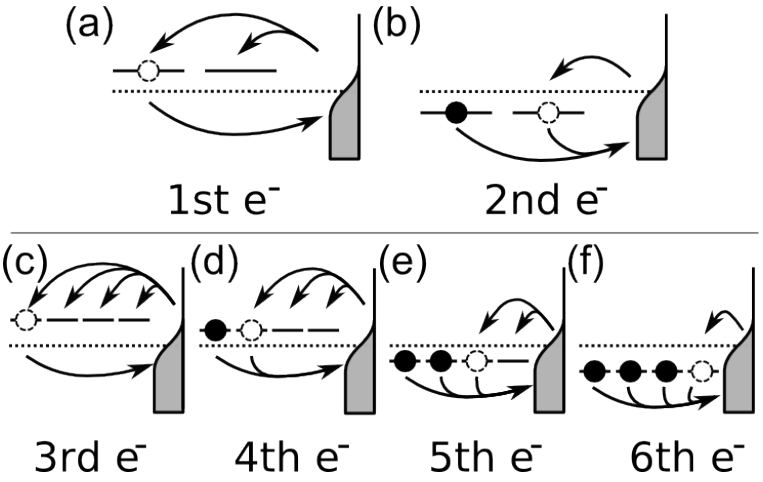

Figure 2–3: The asymmetry in the number of ways to add and remove electrons leads to a shift in the location of maximal tunneling (i.e. a shift in the Coulomb blockade peak maximum). This dot has six energy levels, with two in the first shell and four in the second. The gray region on the right of each diagram is the Fermi-population of the 2DEG. The black circles are electrons that are already on a dot level (solid black line) and the dashed circles are electrons that will be added. The dashed line is where the non-degenerate energy level would line up with the 2DEG energy levels to have maximal tunneling. These alignments for degenerate levels are shifted due to the asymmetry between the number of ways to add or remove electrons. [67] Image courtesy of Steven Bennett.

increases with an increasing discrepancy between the number of ways to add and remove an electron [67].

2.4.3 Strong Coupling

For the same mean tip-sample gap, we can enter into the strong coupling regime by increasing the cantilever oscillation amplitude until the charge degeneracy point is no longer broadened by temperature, but by the tip oscillation. In this regime, we observe non-linear, amplitude dependent, damping of the cantilever because during one period of motion the cantilever can now swing on and off of a charge degeneracy point leading to z-dependent rates to add (Γ_+) and remove (Γ_-) an electron [53].

$$\Gamma_{\pm}(z) = \eta_{\pm}\Gamma f[\pm E(z)] \tag{2.40}$$

Where $\eta_+ = \nu - n_{shell}$ is the number of ways to add an electron, $\eta_- = n_{shell} + 1$ is the number of ways to remove an electron, and $E(z) = \mu_{dot} - \mu_{2DEG} = 2E_C(1/2 - \mathcal{N}) - Az$. It is the asymmetry between the tunneling rates (i.e. $\eta_+ \neq \eta_-$) which ultimately leads to skewing of the Coulomb blockade peaks observed in the frequency shift and dissipation [53].

Since, in our experiments, the electron tunneling rate is similar to the resonance frequency of the cantilever, the dot-cantilever coupled system has to be described as a whole and we cannot treat the timescales separately. It needs to represent the effect of the cantilever motion on the dot and also the reaction of the cantilever to the number of charges on the dot. The modified Master equations are [53]:

$$\partial_t P_0(z, \dot{z}) = \mathcal{L}_0 P_0 + \Gamma_-(z) P_1 - \Gamma_+(z) P_0 \tag{2.41}$$

$$\partial_t P_1(z, \dot{z}) = \mathcal{L}_1 P_1 + \Gamma_+(z) P_0 - \Gamma_-(z) P_1 \tag{2.42}$$

which include a Fokker-Planck equation to describe the evolution of the cantilever's motion, $\mathcal{L}_n = \omega_0^2(z - z_n - F_{drive}/k_0)\partial_{\dot{z}} - \dot{z}\partial_z + \gamma_0 \partial_{\dot{z}} \dot{z}$, where z is the cantilever position and $\dot{z}$ the velocity. The equilibrium position, z_n, of the cantilever is affected by the number, n, of electrons on the dot: $z_n = An/k_0$.

A mean-field approach together with Eq. 2.41 and Eq. 2.42 provides a familiar expression for the average values of the probability P_1 and z [53]:

$$\partial_t \langle P_1 \rangle = \Gamma_+(\langle z \rangle)\langle P_0 \rangle - \Gamma_-(\langle z \rangle)\langle P_1 \rangle. \tag{2.43}$$

Next, by assuming oscillatory motion for the cantilever, that the frequency shift caused by the tunneling is small (i.e. $\Delta\omega \ll \omega$), and that the total dissipation is small (i.e. $\gamma_0 + \Delta\gamma_1 \ll \omega_0$), we obtain an expression for the effective, amplitude-dependent cantilever dissipation [53]:

$$\Delta\gamma_1 = \frac{\omega_0^2 A}{\pi k_0 a} \int_0^{2\pi/\omega_0} \sin(\omega_0 t)\langle P_1(t)\rangle dt \tag{2.44}$$

Eq. 2.44 links the dissipation to the component of the time-varying dot charge, $\langle P_1(t)\rangle$, which is out of phase with cantilever tip motion, as expected from Eq. 2.10. The subscript 1 in $\Delta\gamma_1$ and P_1 indicates which electron is being added to the dot, here it is the first electron. To use Eq. 2.44, we need to solve for $\langle P_1(t)\rangle$, or more generally $\langle P_n(t)\rangle$, numerically. Although this task is relatively simple for $n = 1$ (we just substitute $\langle z(t)\rangle = a\cos(\omega_0 t)$ into Eq. 2.43), it can become quite formidable if multiple shells are involved as the number of Master equations increase with the number of levels. However, in Chapter 4 we see that studying just one level allows us to understand why the lineshape is skewed, and in which direction, and the implications of the direction, which captures most of the interesting features. For more details on what happens when the p-shell is included in the theory, please see Ref. [53].

Unlike the lineshape for the non-degenerate Coulomb blockade peak (Eq. 2.35), the lineshape for a peak within a degenerate shell (Eq. 2.38) is no longer symmetric along the energy axis. In the weak coupling regime, this asymmetry is small and could not be distinguished within the data, and so we could not claim the presence of degenerate energy levels based solely on the peak lineshape which were described well by both (Eq. 2.35) and (Eq. 2.38). This is not the case in the strong coupling regime, where the increased coupling of cantilever and dot drastically enhances the

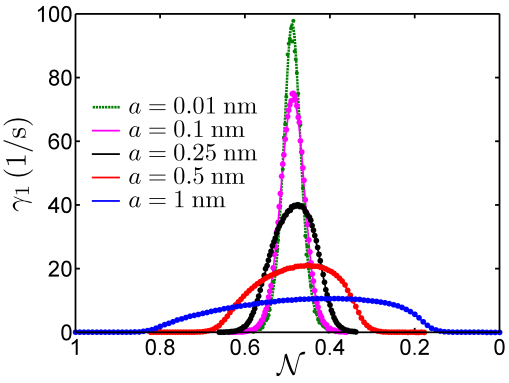

Figure 2–4: The first peak in the dot is theoretically calculated for several oscillation amplitudes. Large oscillation amplitudes (i.e. $Aa \gg k_B T$ enhance the asymmetric peak lineshape [53]. Image courtesy of Steven Bennett.

asymmetric lineshape. Consider the first peak in the two-fold degenerate s-shell. Fig. 2–4 shows the theoretical calculations of this peak for several oscillation amplitudes. The large amplitude of the oscillating cantilever allows for tunneling over a larger V_B range because the voltage dropped across the 2DEG-dot is being modulated to a larger extent. As the cantilever approaches the charge degeneracy point for this peak, the rate to add an electron (Γ_+) is limited by the two ways for the electron to enter into the shell, but as the maximum of this peak is surpassed (and it is more favourable to have the electron in the dot than not) the rate (Γ_-) becomes limited by the single way to empty the dot. Since fewer tunneling events leads to less damping, this peak becomes noticeably more and more skewed for increasing oscillation amplitude and the direction of the skewedness is away from the center of the shell, just as the peak maxima shifted away from the center of the shell with temperature.

2.4.4 Real-Time Measurement Of Electron Loading

Recall, in Section 2.4.3, the expression for the equilibrium deflection of the cantilever is given as $z_n = An/k_0$ for force An (Hooke's Law). In this section, we

explore under what conditions we may be able to measure this deflection caused by a change in the electrostatic force when an electron tunnels into the dot, allowing for real-time read out of the dot occupation. This is opposed to the scenario discussed thus far where the cantilever experiences damping over time caused by the single electron tunneling.

Since the force required to add a single electron is just $F_{ts} = A$, the deflection of the cantilever $z_1 = A/k \sim 20$ fm for $A \sim 1\times10^{-12}$ N and $k \sim$ 48 N/m. This value for A is representative of what we have measured in the experiment. Although all-fiber detection schemes have demonstrated deflection noise densities of 2 fm/$\sqrt{\text{Hz}}$ [70], this deflection is below the resolution of our microscope and furthermore although A can be increased by reducing the tip-sample distance, we cannot increase A enough to see real-time electron tunneling events. We can see this from the equation for A, given in Eq. 2.25, where we see that A can be increased through increasing V_B or decreasing z. We cannot gain much by increasing V_B as the large electric field between tip and sample can potentially cause material to be field emitted from the tip, compromising the experiment and potentially altering the dot. To determine how A may be increased by decreasing z, we can use a capacitance model such as the one by Hudlet et al for a sphere-plane, to describe C_{tip} [65]:

$$C_{tip}(z_0) = 2\pi\epsilon_0 R \ln(1 + R/z_0), \tag{2.45}$$

for tip radius, R, and electric constant, ϵ_0. From this we can also easily obtain $\partial C_{tip}/\partial z_0$, and provide reasonable estimates for the remaining constants in A to observe the z dependence. From this one also learns that we will not significantly increase A by decreasing z, certainly not by a factor of 10 or more, and approaching the cantilever is risky as there is still the potential for material to be field emitted

from the tip with high electric fields and also there is a risk of snap-to-contact when very small oscillation amplitudes are used. However, other types of samples could have a much larger A without the need for larger voltages or smaller tip-sample gap.

The size of the deflection is much smaller than the smallest oscillation amplitudes that we can use ($\sim$ 2 Å), making the deflection of the cantilever a small change on a large oscillation signal which is more difficult to measure. However, if we could reduce the noise of our detector we could also oscillate the cantilever with smaller amplitudes (the thermal oscillations at 4.5 K are $\langle z_{osc} \rangle = \sqrt{k_B T/k} \sim 1$ pm), making this signal easier to detect. It would be a very hard experiment and we are not equiped to perform it at this time but we believe it can be done.

As discussed in Chapter 1, single electron charge resolution is a well known capability of AFM. So far we have not identified a discrete change in frequency shift caused by a change in electrostatic force after a single electron enters the dot, however this should be easier to detect than a change in AFM cantilever deflection and in future experiments we will try to resolve this feature.

CHAPTER 3

Instrumentation

The precursor to the atomic force microscope, the scanning tunneling microscope (STM), was invented by Binnig, Rohrer, Gerber and Weibel in 1982 [30]. The STM imaging capability offered unprecedented resolution of conductive substrates, achieving atomically resolved images within the first two years of operation. Images were produced by maintaining a fixed tunneling current between a sharp metal tip and the surface while raster scanning the tip. The exponential fall off of the tunneling current not only makes it more probable that the tunneling current passes through the last atom on the STM tip before electrons tunnel into the sample, but in addition makes the tunneling current a very good indicator of the tip-sample gap. This leads to higher spatial resolution and provides a feedback channel to control the tip-sample gap. In concert, these two properties led to the success of the STM, highlighted by the 1986 Nobel Prize in physics for its inventors.

Although useful for imaging conductive surfaces, STM was unable to measure non-conductive surfaces where electron tunneling was not feasible. In 1986 the atomic force microscope, invented by Binnig, Quate, and Gerber [32], was based on the same principles as the STM; namely, a *cantilever* with sharp tip placed in close proximity

to a sample surface would lead to cantilever deflections (i.e. static mode AFM as discussed in Chapter 2) due to tip-sample *force* interactions. By controlling the cantilever deflection while raster scanning the tip, i.e. by keeping the interaction force constant with a feedback loop, constant force images could be produced.

The first dynamic mode AFM ever used was amplitude modulation mode or AM-AFM in 1987 [56]. In this mode the cantilever is driven into oscillation with an excitation signal of fixed frequency and drive. When the cantilever interacts with sample forces, the change in resonance frequency leads to a decrease in oscillation amplitude which is used as a feedback mechanism. Since the cantilever tip is not in contact with the sample, the imaging process is gentler on the tip and sample than when operating in contact mode. The main drawback to this mode of operation is the time required for high-Q cantilevers to acquire a new equilibrium amplitude since this time is proportional to Q, i.e. $\tau_{AM} \approx 2Q/f_0$ [58]. This is a disadvantage because higher Q cantilevers are less influenced by thermal noise and are often obtained in vacuum, where ultra-clean samples can be prepared and studied in-situ. The long response time of the amplitude essentially means that at each location, each pixel, in the image, the cantilever tip must remain over that one spot for τ_{AM}, and the large Q factors make imaging infeasible.

The invention of frequency-modulated AFM (FM-AFM) in 1991 [58], which provided the instructions for using the resonance frequency shift of an oscillating cantilever as opposed to the change in amplitude, pushed the AFM into new environments, in particular vacuum systems, and solidified its reputation as a powerful surface science characterization tool. In contrast to AM-AFM, in FM-AFM the transient response rate is independent of Q: $\tau_{FM} \approx 1/f_0$ [58]. Since the minimal detectable force gradient is inversely proportional to the square of Q [56], the ability

to use a high Q cantilever is a huge advantage, particularly for dissipation measurements since the background dissipation, γ_0, is proportional to Q. Using FM-AFM, the minimum force F_{min} that can be detected by a thermally limited microscope is [58]:

$$\frac{F_{min}}{\sqrt{B}} = \sqrt{\frac{4kk_BT}{\omega_0 Q}}. \tag{3.1}$$

Where B is the bandwidth of the FM-demodulator. At $T = 4.5$ K with $k = 48$ N/m, $\omega_0 = 150$ kHz, and $Q = 100,000$, the $F_{min}/\sqrt{B} \sim 1$ fN/$\sqrt{\text{Hz}}$.

Since all surfaces, regardless of their conductivity, will have forces which interact with the cantilever, AFM is not restricted by the sample conductivity. In fact, the robustness of AFM makes it suitable for a variety of samples and imaging environments. For example, it is commonplace to find AFMs used to image biological samples on glass or in liquids (where the samples can be kept alive), in ambient, ultra-high vacuum, ultra-low temperature, and high-temperature environments. In fact, AFMs tailored to each of these environments are commercially available.

3.1 Introduction to Low Temperature AFM

All types of AFM have their own set of challenges, however we are restricted by the environment which best suits our sample. In order to access the Coulomb blockade regime for the quantum dots, we must operate at low temperature ($T < 100$ K). Our home-built cryogenic AFM [71] was built for use at 4.2K (the temperature of liquid helium). The original design and construction is described in the PhD thesis of Mark Roseman [72]. Improvements and modifications to the microscope, most notably the addition of a sample heater, are listed in the PhD thesis of Romain Stomp [66]. An RF-modulated interferometer (for measuring the cantilever deflection) with 1550 nm wavelength was added later and is described in Ref. [73].

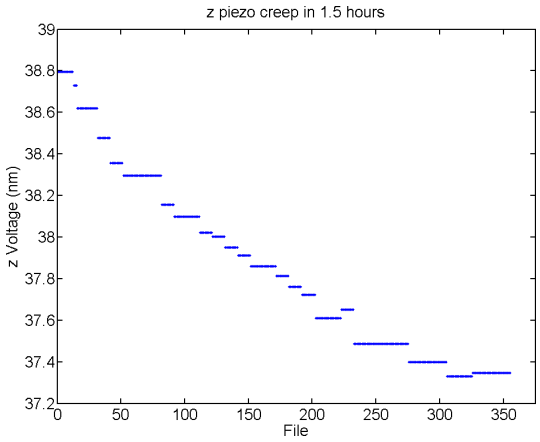

Figure 3–1: The creep of the piezotube in the z-direction is plotted as a function of file number at 4.5 K. We were collecting approximately 350 images over the same location for 1.5 hours and when the frequency shift showed a noticeable change, the height was readjusted (this is the reason for the step-like appearance). In 1.5 hours, the z-creep was approximately 1.5 nm. After 1.5 hours the creep is starting to stabilize.

Not only does working at lower temperature increase the likelihood of observing quantum phenomena, but even classical properties which are thermally activated (e.g. charge traps, dewetting) can be sufficiently slowed in order to investigate dynamics. Working at low temperature also reduces the thermal noise of the microscope: the thermal drift of the microscope body as well as the creep of the piezoelectric tube beneath the sample is reduced so that the location of interest remains in the field of view longer, in addition the thermal noise of the cantilever is reduced while the Q is increased and a higher Q reduces the noise in tracking the resonance frequency. A plot of the piezotube creep at 4.5 K is provided in Fig. 3–1. For comparison, after the creep had stabilized during an experiment at 77 K and left idle, the creep was about 28 nm in 13 hours. When the microscope is immersed in either liquid nitrogen or liquid helium (with exchange gas at 4.5 K), the temperature is very stable, and the piezo-creep will be the main cause of the image window moving with time.

The main disadvantage to using a low-temperature AFM is the stress/strain during thermal cycling leading to problems at low temperature. These problems mainly include: misalignment of the moving parts, and the soldered wires and glued parts disconnecting. In order to ensure success, great care must be taken in assuring the microscope is in peak condition before cooling it down and in particular all electrical loops must be checked. Another disadvantage of our microscope which exacerbates this problem is the long turn-around time. Once the microscope is cold, it needs to be brought up to room temperature before repairs can be made, and in addition the Dewar needs to also warm up before the repaired microscope can be put back inside. This process takes a minimum of two days. Once the microscope has been placed in the Dewar, it takes a day to pump the gas out of the microscope and another day to cool down. However, for the Coulomb blockade experiments, it is important that the cantilever has a high Q factor, and since this is pressure dependent you gain by reducing the pressure in the microscope as much as possible before precooling. This takes a while for our microscope as the conductance of the gas lines into the body is low (long, narrow lines). The pressure obtained before precooling sets the lower limit for the pressure at lower temperatures. We typically run the pump for about one week or more. Typical values of decent Q factors are: 500 (room temperature in air), 7,000 (room temperature at 3×10^{-5} mbar), 60,000 (77 K at 7×10^{-5} mbar), and $100,000 - 200,000$ (4.5 K with exchange gas at 3×10^{-3} mbar).

The stress and strain endured by the materials over such a large temperature range demands that the microscope frame be built as symmetrically as possible, and that all glues and other components be chosen with great care. Since our microscope has the capability of applying a magnetic field up to 8T, it is also important that the microscope not be made of magnetic materials.

3.2 AFM Design

Fig. 3–2 shows a photo of the actual microscope and a simple schematic which highlights the main features. The diameter of the microscope is limited by the bore size of the superconducting magnet. The cantilever is glued above a piezoelectric stack which is used for driving the cantilever. There are two "walkers" - one for the optical fiber and the other for the sample - which move components along piezoelectric stacks using stick-slip motion [74]. The "optical-fiber walker" approaches the end of the fiber optic towards the backside of the cantilever, while the "sample walker" likewise coarse approaches the sample towards the cantilever. Underneath the sample is a piezotube which is then used for fine approach to the cantilever tip. Great care must be taken when approaching the sample to the cantilever so that the cantilever tip is not damaged. We use an automatic approach to safely bring the sample towards the cantilever. To do this, after each coarse approach step of the sample walker the piezotube extends while monitoring the frequency shift to detect the interaction force, if no force is detected, the piezotube retracts and the cycle repeats. Note that in order for this to work, each course step must be a fraction of the extension length of the piezotube.

The Scanita [75] software controls the piezotube (both its extension/retraction and raster scanning), applies the sample bias, and records all of the data. It also displays the imaging information in real-time. Although these are the basic requirements of an AFM software kit, we prefer Scanita because it gives us more flexibility than other commercial software. We have access to many channels for data acquisition, we have the auto-approach feature just mentioned, and we have flexibility in how we acquire the spectra built right into the software. Using Scanita, we can also adjust the voltages applied to the two scan directions in order to compensate for

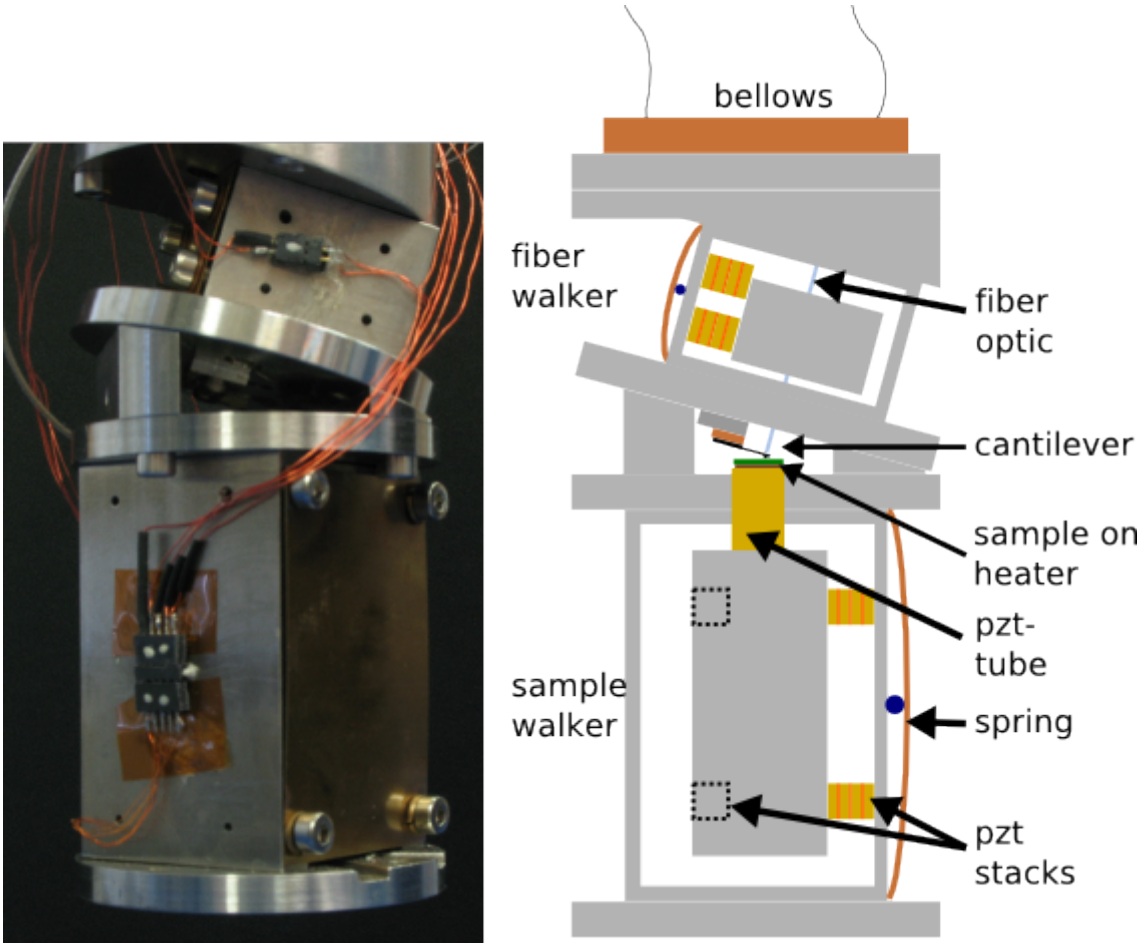

FIGURE 3–2: An actual photo of the cryogenic microscope is shown beside a schematic which labels the relevant features of the microscope. The bottom plate in the schematic is 5 x 52 mm. The different components of the body are slightly rotated in the schematic in order to more clearly label the components.

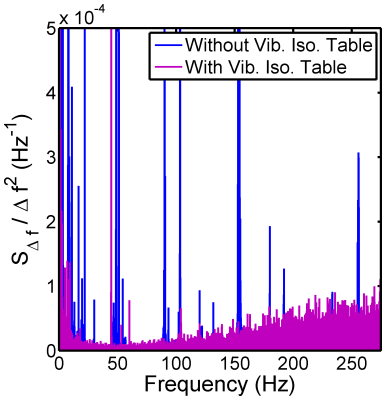

FIGURE 3–3: Power spectral density of the frequency shift of the cantilever while approached to the sample surface, collected over a 300 s time window and consisting of 300,000 points, showing several peaks at low frequency in the data taken without the vibration isolation table. Data is from two different experiments, and the noise at higher frequencies with the table may be due to experimental differences.

a tilted sample. This feature makes it possible to shut off the distance regulation feedback to collect constant height mode images.

Vitally important to the sensitive measurements made with an AFM are vibration isolation techniques. The microscope hangs from a bellows in order to decouple the microscope from external vibrations. Recently, we purchased a passive vibration isolation table (Minus K BM-1 bench top vibration isolation platform) and placed the Dewar on it which further reduced the coupling of the microscope to the low frequency oscillations of the building. Fig. 3–3 shows a noise spectra taken before and after the vibration isolation table was installed at 77 K. Clearly, the vibration isolation table is effective at decoupling the microscope to the building vibrations. The vast majority of the data, including all of Chapter 4, presented herein was taken prior to the installation of the vibration isolation table. Streaks in the images were often caused by the elevator or someone walking by the microscope.

We have built our AFM with features which can be especially useful at low temperature: a heater [72] and superconducting magnet. The heater allows us to do experiments as a function of temperature. The superconducting magnet (see Ref. [72]) allows us to change the perpendicular magnetic field experienced by the sample. The low critical temperature of the magnet means that we can only use it during experiments performed in liquid helium. More details on the design of the AFM can be found in the theses by Roseman [72], Stomp [66] and Cockins [73].

3.3 AFM Operation

As mentioned in Chapter 2, the AFM was operated in self-oscillation mode for the experiments that were done in this thesis. In this mode the cantilever is oscillated by applying the phase-shifted deflection signal to the piezo stack underneath the cantilever, referred to as the bimorph excitation. We use the commercially available silicon Nanosensors PPP-NCLR cantilevers with nominal spring constant of 48 N/m. We sputter coat the cantilevers with a 10 nm titanium adhesion layer and 20 nm of platinum to ensure electrical conduction at low temperature. Typically, the cantilevers have a resonance frequency of 160 kHz.

Cantilever beam deflection detection is done via a fiber optic laser interferometer [76]. The interferometer consists of the reflection of the main reference beam from the glass-air interface at the cleaved end of the optical fiber (optimally $\sim 4\%$ of the light) and the reflection from the back-side of the cantilever. We use a 1550nm RF-modulated laser for this purpose. The noise floor of the interfeometer is about 60 fm/$\sqrt{\text{Hz}}$. For more details about this laser see Ref. [73]. Placing the fiber as close as possible to the cantilever beam increases the detection sensitivity. Most importantly, however, is that the cantilever-fiber gap is adjusted so that the interferometer signal is centered in the region of steepest slope as here cantilever motion leads to

the greatest change in interferometer intensity. The sensitivity of the interferometer signal is given by [77]:

$$S = \frac{2\pi V_{pp}}{\lambda_{laser}} \tag{3.2}$$

Where V_{pp} is the peak-to-peak voltage of the interferometer signal and λ_{laser} is the wavelength of the laser. Eq. 3.2 converts the cantilever deflection signal into nanometers and is used to adjust the drive amplitude to obtain the appropriate oscillation amplitude. For $\lambda_{laser} = 1550$ nm and $V_{pp} \sim 10$ V, Eq. 3.2 gives $S \sim 0.04$ V/nm, with ~ 2 $\mathrm{mV_{rms}}$ noise on the signal. In self-oscillation mode, the detection signal itself is used to drive the cantilever. The amplitude of the detection signal is compared to the setpoint and the drive signal is modified (via a PI controller) in order to maintain the setpoint. The detection signal must be phase shifted before it is reapplied to the cantilever. The bimorph (drive) amplitude is provided by the automatic gain controller (AGC) as the dissipation of the cantilever [78]. In practice, at 4.5 K we are able to oscillate the cantilever with amplitudes as small as ~ 0.2 nm but the oscillation becomes unstable for smaller values.

The block diagram for self-oscillation mode is shown in Fig. 3–4. In this mode, the sinusoidal position signal is fed into a phase-lock-loop (Nanosurf easyPLL-plus) which measures the oscillation frequency of the cantilever and compares it to the stored reference value to provide the resonance frequency shift, $\Delta\omega$, which we hereafter refer to as the frequency shift. The frequency shift is used as feedback to regulate the tip-sample gap. Once amplified to high voltage, this signal is applied directly to the piezotube underneath the sample, which expands or retracts to compensate for the change. This can be done while raster scanning to produce an image taken at constant frequency shift. This is the typical protocol for producing, what is

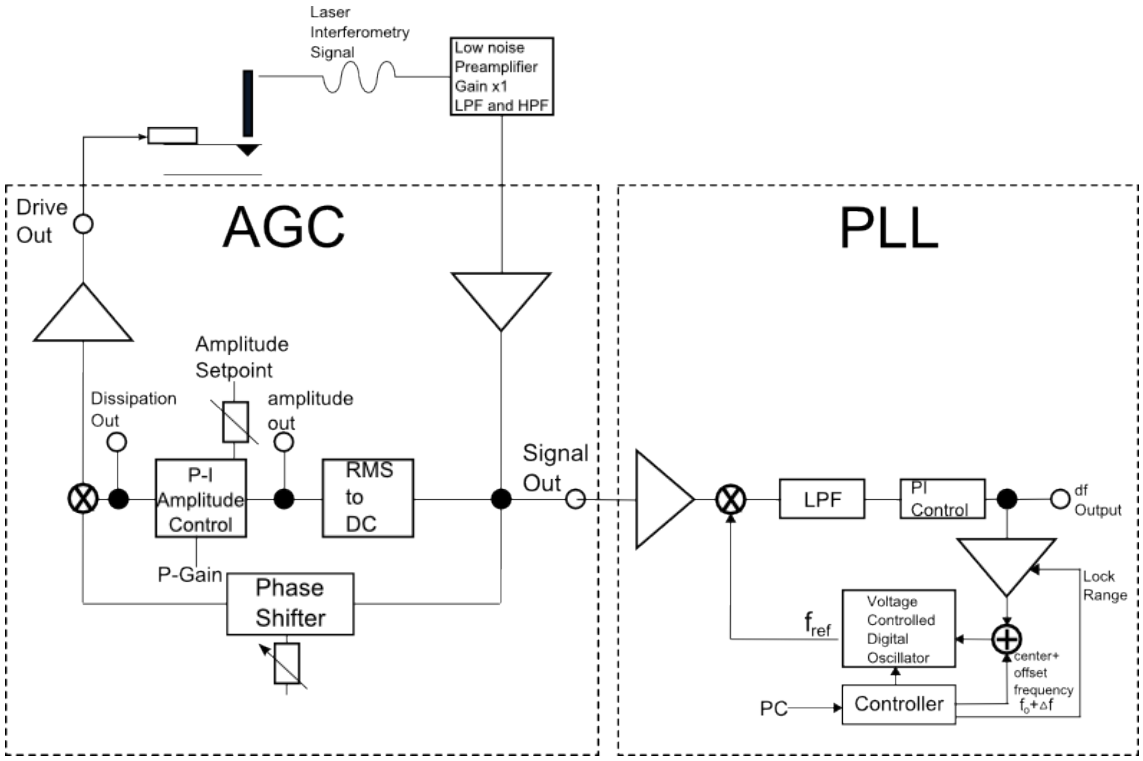

FIGURE 3–4: Block diagram for self-oscillation mode [78]. The left-box isolates the components for maintaining the oscillation amplitude (the AGC), while the right contains the components used for frequency tracking (the PLL).

referred to as, topography or height images, where we are interested in the piezotube extension that was required to maintain a constant frequency shift. In this thesis, constant height images are also frequently used. In contrast, constant height images are produced by recording the cantilever frequency shift and dissipation while raster scanning the tip with the distance-feedback off.

In addition to images, which provide spatial information over our sample, we can also collect spectra over one location while changing the tip-sample gap, bias voltage, cantilever oscillation amplitude, or by not changing anything at all and collecting data as a function of time. The use of images in combination with spectra often greatly assist data interpretation.

3.4 Experimental realization of QDs: Sample Preparation

In order to have a quantum dot, we must have carrier confinement. In semiconductors, the potential well which confines the carriers are formed from the band-alignment in heterostructures. The sandwiched material (the dot) requires a lower conduction band to confine electrons and/or a higher valence band to confine holes [79].

Self-assembled quantum dots are formed by a process called *Stranski-Krastanov* [80] growth where strain between layers drive the spontaneous formation of islands out of the strained layer. Using chemical beam epitaxy, where gaseous materials build on a substrate monolayer by monolayer, a significant difference between the lattice of the deposited material and the substrate results in only the first couple layers being able to form into a two-dimensional layer. The crystallized material is strained by the lattice constant of the underlying substrate. A critical thickness is reached where it is energetically favourable to reduce the strain by the spontaneous formation of regularly shaped islands. The shape and size can be controlled by the

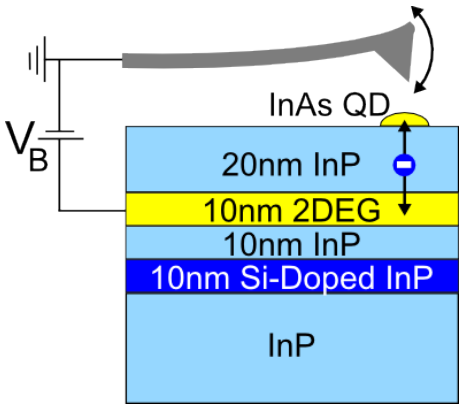

Figure 3–5: Schematic of layers of the sample with the biased AFM cantilever.

strain between the two materials, the temperature, and speed of growth [52]. In our samples these InAs islands are typically about 50 nm in diameter and 1-12 nm high. Although these structures tend to grow with faceted edges, many of the smaller structures we observe (of height 6 nm or less) lack well defined borders and look slightly irregular in topography.

Our samples are grown at the National Research Council of Canada by Sergi Studenikin and Philip Poole [81]. Our sample consists of the following layers: randomly positioned on the sample surface are self-assembled InAs quantum dots, separated from a two-dimensional electron gas by a 20 nm tunneling barrier made of InP (Fig. 3–5). More specifically, the layers of the sample are: 460 nm undoped InP grown on top of an insulating InP substrate, 10 nm Si-doped InP layer, 10 nm undoped layer, 10 nm $In_{0.53}Ga_{0.47}As$ layer, 20 nm undoped layer, and a 1.82 monolayer of InAs.

In the past, we would heat the sample to 120°C for 1 hour while pumping out the microscope to more efficiently remove the water layer from the sample surface. However, we no longer heat the sample since we obtained the same quality of images without this step and we want to exercise as much caution with our samples

as reasonably possible. Electrical contact to the 2DEG is done via indium diffusion through the upper layers of the sample. At 4.5 K the sample is exposed to a higher concentration of helium gas (typically 3×10^{-3} mbar) which we use as exchange gas to keep the microscope from warming up due to thermal coupling to the environment. At other temperatures we typically operate at pressures of approximately 1×10^{-4} mbar or less. Unfortunately, our samples are not fabricated and studied in situ and thus are often exposed to the lab air, however we have not yet noticed any change in the quality of the samples overtime.

CHAPTER 4

Quantum Dot Energy Level Spectroscopy

The charging energy of some of the InAs dots is so large that even at 77 K the dots are in the Coulomb blockade regime. This, in combination with large ΔE, allows us to study the changes in Coulomb blockade peaks over a large temperature range. This section begins with a qualitative overview of the features observed in the dissipation images before moving into the more quantitative analysis of the electron addition spectra obtained over isolated quantum dots. The final section of this chapter will cover our progress towards the analysis of multi-dot complexes.

4.1 Coulomb Blockade AFM Images

The theory in Chapter 2 on the Coulomb blockade peaks as a function of sample voltage focused on the dissipation for a fixed tip position above the sample. In a constant height image, the sample is raster scanned beneath the tip with the distance regulation feedback off. As the tip-dot distance changes the voltage dropped across the dot-2DEG also changes since V_B is held constant. The fraction of V_B that is applied between dot-2DEG is given by the dimensionless lever arm, $\alpha =$

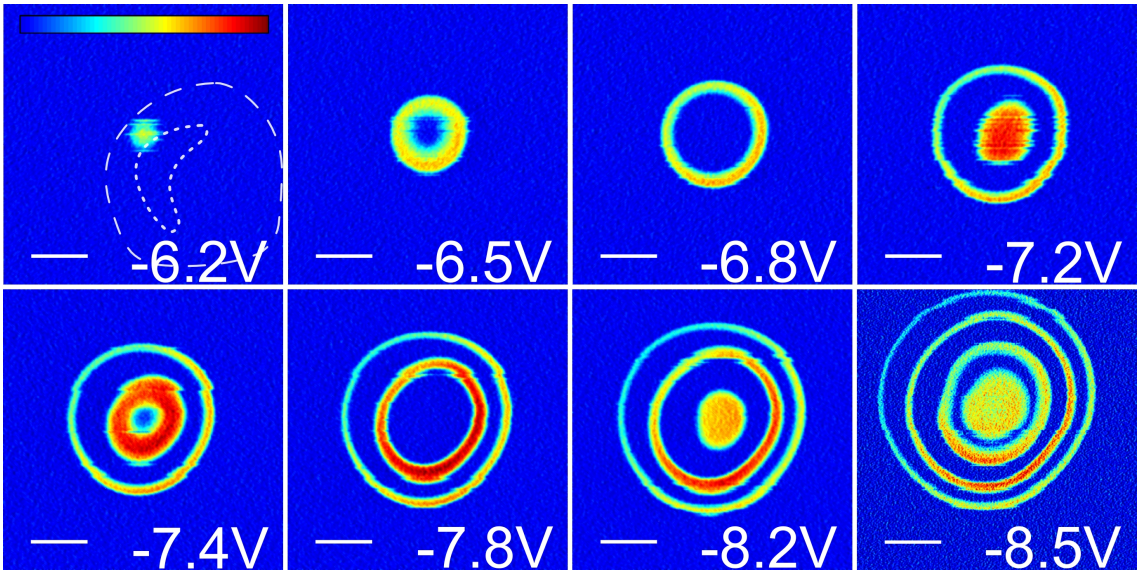

Figure 4–1: Dissipation images showing sequential loading of electrons into a quantum dot through increasing the bias voltage. The shape of the InAs island is outlined in the first image, with the taller region also outlined by a more closely spaced dashed line. This data was collected at 4.5 K, with 0.8 nm oscillation amplitude. These images took approximately 20 min. to complete. The scalebar is 20 nm. All images share the same colorbar with scale $0 - 0.85$ Hz for all except the last image, with scale $0 - 2$ Hz. The last image was taken at a later time in the experiment and so the image is slightly shifted. [67]

$\alpha(x, y, z) = \frac{C_{tip}}{C_\Sigma}$. We observe rings in the dissipation images because when the voltage satisfies a charge degeneracy point, the resulting single electron tunneling events increases cantilever dissipation, and for a given charge degeneracy point the equipotential traces a rough ring around the dot (the locations where the tip-dot distance are electrostatically equal). The rings are thus rings of constant α. The ring furtherest from the dot center corresponds to the first charge degeneracy peak since that ring occurs at the largest tip-sample separation. Fig. 4–1 shows an example of the dissipation images for an isolated quantum dot at multiple sample voltages.

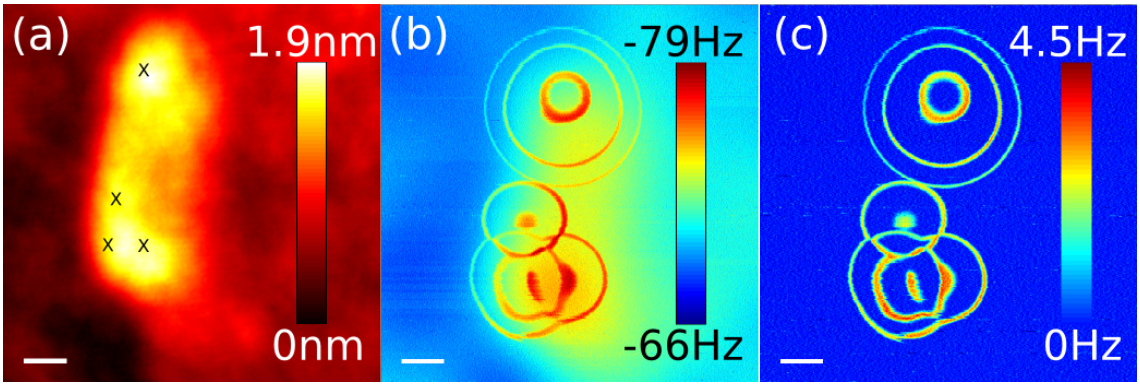

Figure 4–2: Comparison of InAs dot topography image (a) to the constant height images of the frequency shift (b) and dissipation (c). (b) and (c) were taken simultaneously. Approximate locations of dots are marked with X's in (a). (a) was taken at $T = 77$ K, $\Delta\omega/2\pi = -9.4$ Hz, $a = 1.6$ nm and $V_B = -0.35$ V. (b) and (c) were taken at $T = 4.5$ K, with $a = 0.4$ nm, $V_B = -8.0$ V, and $z_0 \sim 19$ nm. Scalebar 20 nm. [67]

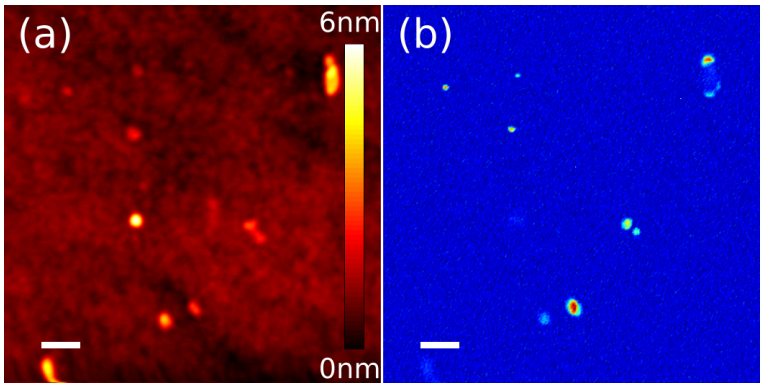

Figure 4–3: Large scan range AFM topography (a) and dissipation (b) images taken simultaneously with V_B = -4 V, $\Delta\omega/2\pi$ = -29 Hz, and $a = 8$ nm at 77 K. The correlation between dissipation features and quantum dots is clear in this image. Notice that taller dots tend to have less pronounced dissipation. Scalebar 200 nm.

4.1.1 Qualitative Features of Dissipation Images

Since the frequency shift images are influenced by the sample topography, the rings are much more visible in the dissipation images and so we focus on the dissipation images here (Fig. 4–2). However, we note that there is a possibility that, for some tunneling rates, the rings will be more apparent in the frequency shift as discussed in Chapter 2.

To choose which dot to study, we first take a relatively large image of about 1-2 μm in order to find isolated dots with large dissipation signals. Often, smaller dots are preferred because the larger E_C makes it easier to identify individual rings and we generally observe larger dissipation signals from the small dots. Taking an image with large oscillation amplitude, e.g. $a \sim 10$ nm, makes it easier to identify these conditions since the large oscillation amplitude fluctuates V_B to a greater extent, making it more likely to find degeneracy points. Fig. 4–3 shows a large scan range topography and dissipation image taken simultaneously. This image highlights that the vast majority of dissipation features at large negative voltages are associated with electrons tunneling into the quantum dots (occasionally additional features are observed, these are discussed in Chapter 6). Fig. 4–4 shows the effect of the oscillation amplitude on the ring width in the dissipation images. There is increased dissipation where multiple rings overlap. The near doubling of the ring height in these regions of overlap suggest that the oscillating cantilever is populating two levels simultaneously.

The resolution in $\Delta\gamma$ and $\Delta\omega$ images is very sensitive to scan speed. The time per pixel spent by the cantilever at each location plays an important role in image quality, especially since typical imaging speeds would certainly prevent one from observing the Coulomb rings from most dots. In a 256 $\times$ 256 pixel image, we usually require at least 1 s/line to barely resolve the rings in a 500 nm $\times$ 500 nm

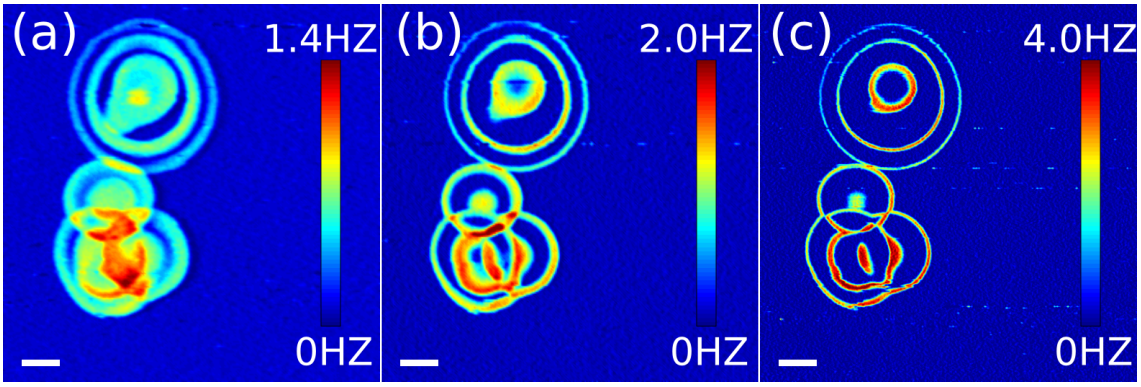

Figure 4–4: Dissipation images taken in constant height mode with V_B = -8 V and a = 1.6 nm (a), 0.8 nm (b) and 0.4 nm (c) at 4.5 K. As the cantilever oscillation amplitude is reduced, the rings become more narrow. All of these oscillation amplitudes are large enough to broaden (and reduce the amplitude of) the rings. Larger oscillation amplitudes can lead to the overlap of rings, which increases the dissipation as more tunneling occurs. Scalebar is 20 nm.

image, but in general we must use 2-8 s/line. A typical image will require 256 lines × 4 s/line = 17 min to complete. Scanning more slowly increases the signal to noise, which is important because the signal is small and the rings are narrow. It is also important to perform the dissipation images using *constant height* mode with the gap-control feedback loop turned off. This leads to less distortion of the rings as the raster scanning cantilever is not simultaneously following the surface topography; furthermore it simplifies analysis as the tip-dot distance is much more straight forward to calculate (assuming a point source for the dot).

As alluded to in the previous chapters, it is assumed that each InAs island constitutes a single quantum dot, however the dissipation images revealed that most islands actually are comprised of multiple dots! This would be very difficult to determine using other techniques which do not allow for spatial resolution. Transport measurements, for example, which attach electrodes close to the dot, would measure conductance spectra which would consist of the Coulomb blockade peaks from several

quantum dots and it would be difficult to know how many dots are participating. In general it is often assumed that each island corresponds to one quantum dot, but our results clearly show that this is not always a valid assumption.

Is it possible that the tunneling we observe is not between 2DEG and dot but across some other barrier? It is possible, however we have good reasons to believe it is a 2DEG-dot tunneling process. Most importantly, the dots do show some correlation between the size of the InAs island and the charging energy of the dot; taller islands tend to have smaller E_C and vice versa, and although there are multiple dots in one island we note that the islands are often irregular in shape and often dot positions seem correlated with these irregularities (see Fig. 4–5). We also note that the majority of rings are centered only in locations where InAs islands are easily identified (see Fig. 4–3). One observation worth pointing out here is that the quantum dots often are not centered with respect to the island, and can be located anywhere within the island perimeter. Finally, usually there are 2-4 sets of concentric rings within a given island, and although this seems like a lot, if the rings were originating from traps at the structure boundary or surface, then we would expect to see a much larger density of rings covering the entire surface of the dot. It would be nice to further support this argument (that the tunneling is really happening between 2DEG and dot) by comparing the measured tunneling rate to values calculated by other means, however currently no other technique is capable of doing so for our dots. Our technique is the only one which has measured the tunneling rate between a 2DEG and uncapped self-assembled dot.

The images also reveal some details about the quantum dot environment. For example, the rings are not perfectly circular or uniform in width. Both of these features can be noticed in Fig. 4–1. The deviation of the equipotential from a perfect

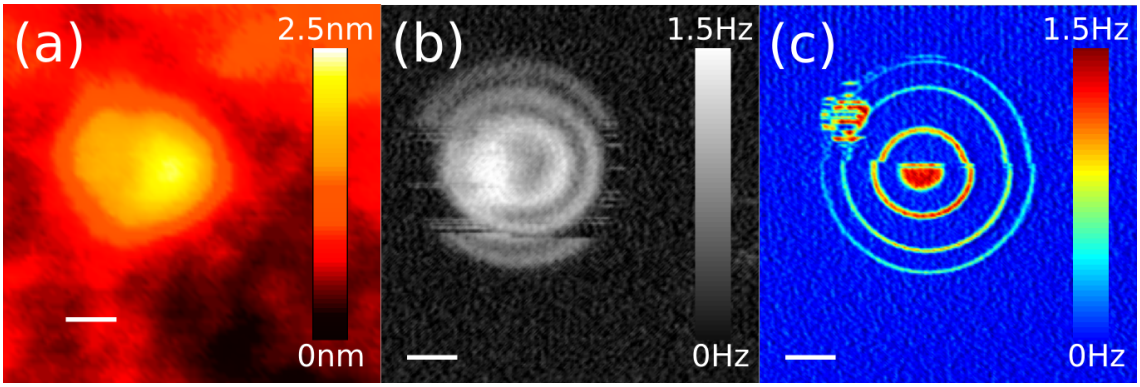

Figure 4–5: Topography of InAs island (a) and corresponding dissipation images taken in constant height mode at 77 K (b), and 4.5 K (c). At both temperatures, this dot seems to be affected by changes in the electrostatic background. In (b) the number of electrons in the dot is fluctuating by one, as observed by the streaky outer ring. In (c), while the cantilever is scanning in the upwards direction, the energy level of the dot seems to shift suddenly below the energy level of the 2DEG. Also observed in (c) is the first streaky ring of another dot. Perhaps this new dot, which seems to have a shallow confinement potential, was the cause of the streaky ring in (b). Notice how in (c) the two observed dots roughly correlate with the island structure in (a) [67].

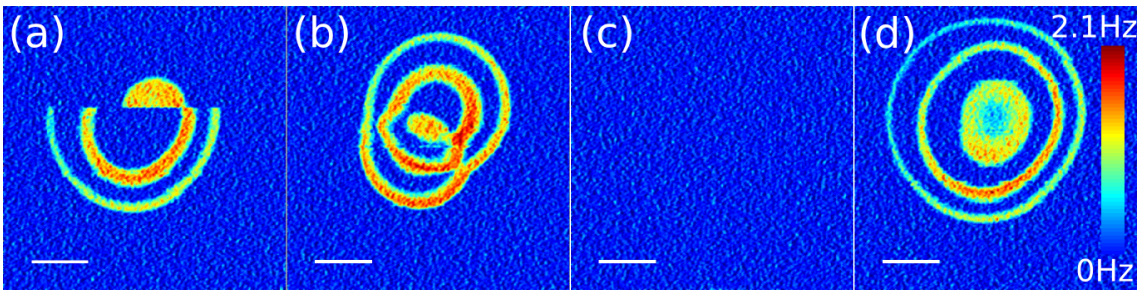

Figure 4–6: Dissipation images taken in constant height mode at 4.5 K with 0.8 nm oscillation amplitude. The slow scan direction is upwards in all four images. In (a) a sudden and dramatic switch of the confinement potential of an isolated quantum dot (the same dot as shown in Fig. 4–1) results in a double quantum dot ($V_B = -8.0$ V). The double dot is confirmed in (b) at $V_B = -9.0$ V. To reverse the change, we image with a positive bias voltage over the same region (c) ($V_B = +6.8$ V). In the following image, we confirm that the dot has returned to its original, single dot, confinement potential, by imaging with $V_B = -8.0$ V (d). [67]

circle indicates that the electrostatics of the environment are *statically* interfering with the voltage dropped across dot and 2DEG. For example, this could be caused by the shape of the InAs structure, a nearby charge deposition or a significantly deformed tip shape.

The electrostatics of the environment can also *dynamically* affect the charge state of the quantum dot. In the images, we sometimes see a ring that is streaky in some region which indicates that, although in other locations along the ring the tip can stay on the charge degeneracy point, it cannot do so here because of fluctuations. Such fluctuations must be caused by the confinement potential of the dot being influenced by some unstable charge configuration. Fig. 4–5 shows an example of a dot with a "streaky" ring.

There is also a middle-ground for the electrostatic influence on the dots, where a bistable charge configuration can allow for us to image two different confinement potentials for one dot. Interestingly, especially from an applications point of view (both for failure analysis or for new types of switches), by imaging with a positive voltage these changes are often reversible! Fig. 4–6 shows an example of such a dot. Imaging this dot at a large negative voltage frequently led to a change in the dot from a single isolated dot to a double dot, and by scanning with a positive voltage we were able to return it to its previous condition. These changes are also seen in the spectra, akin to observations reported from some transport measurements [82]. One might suspect that these changes in the images were caused by some change in the cantilever tip. However, although one dot may undergo a switch, not all dots are effected, implying no tip change (see Fig. 4–7).

Finally, future projects will investigate the ability to manipulate the confinement potential of the dot. In Fig. 4–8, we show a proof of principle demonstration. Here,

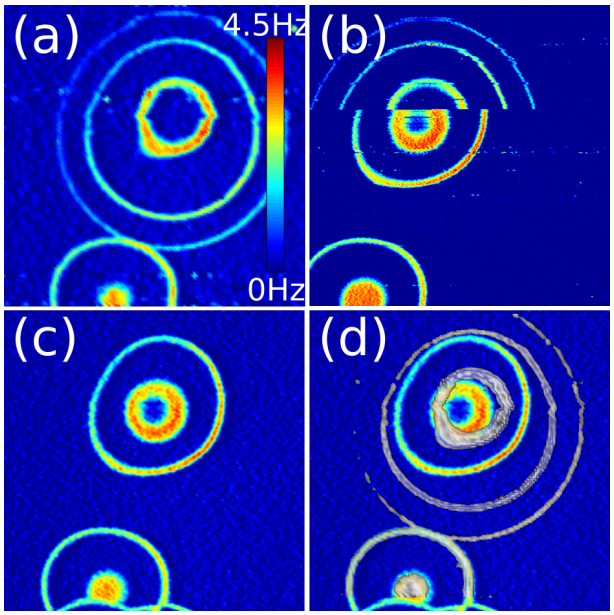

Figure 4–7: The upper isolated dot shown in (a) undergoes a switch in confinement potential in (b). The new shape of the dot is confirmed in (c). Note how both the energy levels of the dot with respect to the 2DEG and the shape of the dot are changed. The lower dot in the images, however, is unaffected. In (d) the rings from (a) are overlaid on (c) and it is clear that the lower dot has not changed. All images were taken with $V_B = -8.0$ V at 4.5 K using constant height mode. This change also was reversed by imaging with a positive V_B as in Fig. 4–6

we were looking at the quantum dot in Fig. 4–8(a) and crashed the tip nearby, in the lower left corner of the image. The confinement potential of the larger dot was affected while the nearby small dot on the right was much less so. From Fig. 4–8(a) to Fig. 4–8(b) it looks like the large dot went from one large or two strongly coupled dots into two clearly separated dots. This is especially apparent in Fig. 4–8(c). Kelvin Probe Force Microscopy [83] was used to simultaneously obtain the topography [Fig. 4–8(d)] and variation in surface potential [Fig. 4–8(e)] which showed that the tip clearly crashed into the sample [the depression in Fig. 4–8(d)] and caused a change in the the uniformity of the surface potential [Fig. 4–8(e)]. Examples such as these are convincing evidence that we can influence the dot confinement potential, which has numerous interesting possibilities.

Although it is relatively easy to observe the effect the environment is having on the dot, and maybe even to obtain an intuitive understanding of the possible mechanisms, characterizing the cause with indirect information is challenging. Nevertheless, we have investigated some methods to characterize different sources of electrostatic noise and these are discussed in Chapter 5.

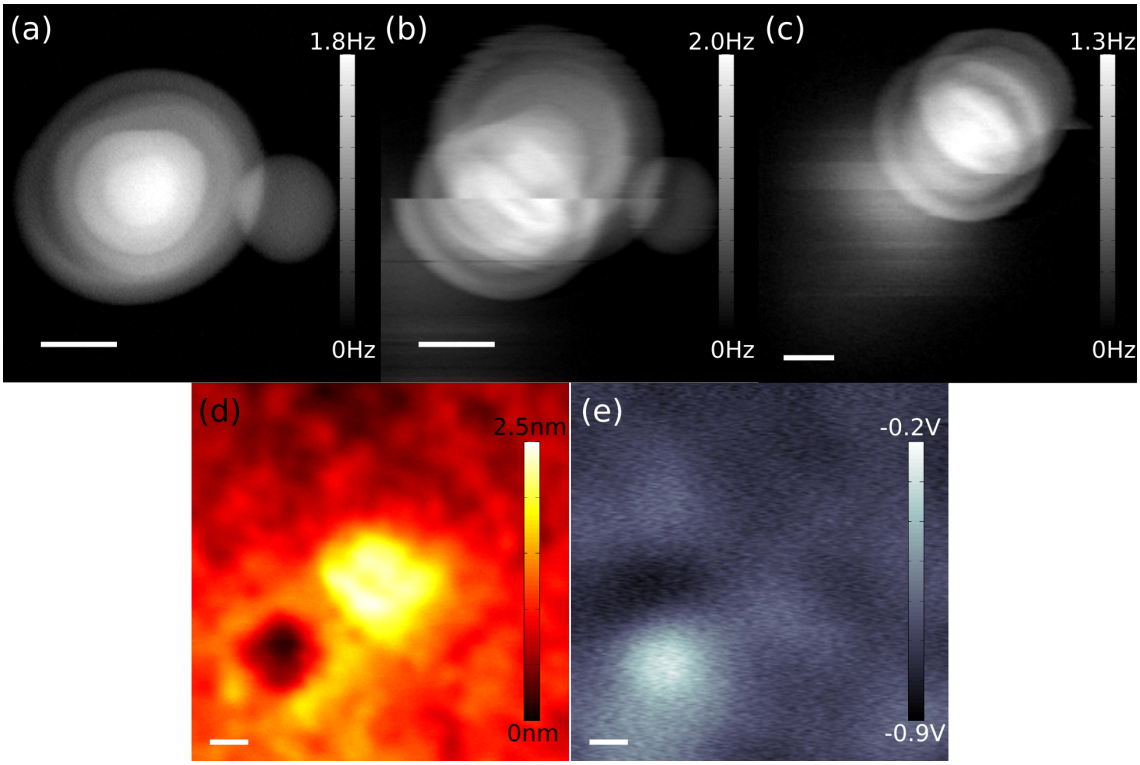

Figure 4–8: The dissipation image in (a) was taken before a tip crash and (b) afterwards. The confinement potential is obviously affected by the charge deposit at the crash site [lower left of the image in (b)]. In (c) we zoom out slightly to inspect the crash site. The voltages in the first three images are: -6 V, -6.5 V and -6.7 V. In (c) the dissipation is lower because the cantilever scanned the image more quickly. The dissipation images are shown in black and white here to be able to distinguish more easily between the rings and the increased dissipation resulting from the crash site. From the Kelvin Probe Force Microscopy images of the topography (d) and contact potential difference (e) taken simultaneously, we see that the tip crash created a depression in the sample that is charged. The Kelvin Probe Force Microscope images applied an additional ac-voltage to the tip of 0.6 V_{rms}, at a 1 kHz modulation, and the lock-in time constant was 3 ms. Scalebar in all images is 20 nm. Oscillation amplitude was 4 nm.

4.2 Electron Addition Spectra

The electron addition spectra that we acquire are always taken as close to the middle of a dot as possible, in a dissipation image this corresponds to the center of a set of concentric rings. One of the main goals of the electron addition spectra analysis is to obtain the lever arm, α, as this parameter converts the voltage axis into energy so that we can get an estimate of the charging energy of the dot. So far, the only way we have of doing this is to obtain thermally limited Coulomb blockade peaks by increasing the temperature and reducing the oscillation amplitude until the peak lineshapes are thermally broadened so that fitting the peak lineshape to Eq. 2.38 determines α. Similarly, thermally broadened peaks are also required to calculate the tunneling rate, Γ, otherwise the large oscillation amplitude reduces the peak height and broadens its width and it is difficult to obtain an expression for Γ with peaks of this lineshape theoretically. Thus, in order to quantify some physical properties of the dot we need to heat the sample and take a voltage spectrum, from which we can know α, Γ, E_C, and ΔE for the n-electron state. In addition, from multiple voltage spectra as a function of oscillation amplitude, we can determine the shell structure and the shell splitting, ΔE, for the ground state electron. To be able to measure ΔE in this way, we need to perform excited state spectroscopy measurements. This is discussed further in Chapter 6.

4.2.1 Obtaining the lever arm, α

In order to have an estimate of the lever arm, we performed Finite Difference Modeling (FDM) of a tip 20 nm above a 20 nm InP sample sitting on an electrode.

Finite Difference Modeling of Cantilever Tip and Sample

Following the approach of [84,85], the cantilever tip was modeled as a cone with a hemi-spherical tip, making the tip-gap-sample system cylindrically symmetric. The system is divided into a number of volume elements, each given a dielectric constant, ϵ, and initial values for the charge density, ρ, and electrostatic potential, u, and the MATLAB program iteratively solves the Poisson equation and potential simultaneously until the result converges. The motivation for writing an iterative program, as opposed to using a software package, was to eventually use a backelectrode with a voltage-dependent charge-density (such as in a 2DEG), and also to allow for the flexibility of placing a quantum dot somewhere other than directly underneath the tip (towards 3-dimensional modeling). The results discussed here do not include a quantum dot, however the heights of the dots that we use to study Coulomb blockade are often sub nanometer (which is below the mesh size of this simulator) and the tip is usually about 20 nm away from the surface, so we do not expect that adding the dot will alter the results significantly.

The initial conditions for the sample at 1 V and the tip at 0 V are listed in the table below.

Material	ϵ	u (Volts)	ρ
Metal (Inside)	10^{11}	1V (sample), 0V (tip)	0
Metal (Surface)	1	1V (sample), 0V (tip)	Calculated Surface Charge
InP	12.5	1 V	0 (insulator at low temperature)
Vacuum	1	0.5 V	0

We use the symmetry of the system to simplify the calculation into a two-dimensional system consisting of a rectangular matrix with one edge along the tip axis. The

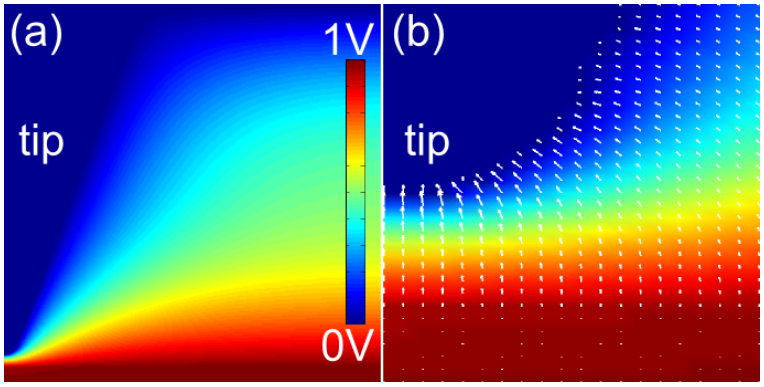

Figure 4–9: (a) The potential and (b) electric field lines of a 20 nm radius tip with 40° cone angle and 20 nm tip-sample gap. (a) is 550 x 550 nm, and (b) is 60 x 40 nm.

outside edges of the matrix require boundary conditions. Since the bottom material is metallic, the ρ and u need not be calculated there ($\rho = 0$ and u is fixed within the metal) and only the surface charge needs to be calculated (using Poisson's equation). The top edge is grounded (held at 0 V) in an attempt to simulate the grounded cantilever beam and microscope structure. The vertical edges are given the potential of the adjacent horizontal volume.

Using the initial and boundary conditions, the program iteratively solves for the potential and charge density simultaneously. An example for a tip with 20 nm tip radius and 40° cone angle, and 20 nm tip-sample gap is shown in Fig. 4–9. The voltage within the vacuum falls off as expected for the given boundary conditions [Fig. 4–9(a)], and the electric field lines are perpendicular to the metal surface [Fig. 4–9(b)]. The charge on the tip and sample is calculated from ρ, from which we can calculate the capacitance. We use the voltage dropped across the sample to get an estimate of the lever arm α and can compare how the lever arm changes as a function of tip cone angle [Fig. 4–10(a)], tip radius [Fig. 4–10(b)], or tip-sample gap [Fig. 4–10(c)-(d)]. Fig. 4–10(a) reveals that the cone angle has little effect on α.

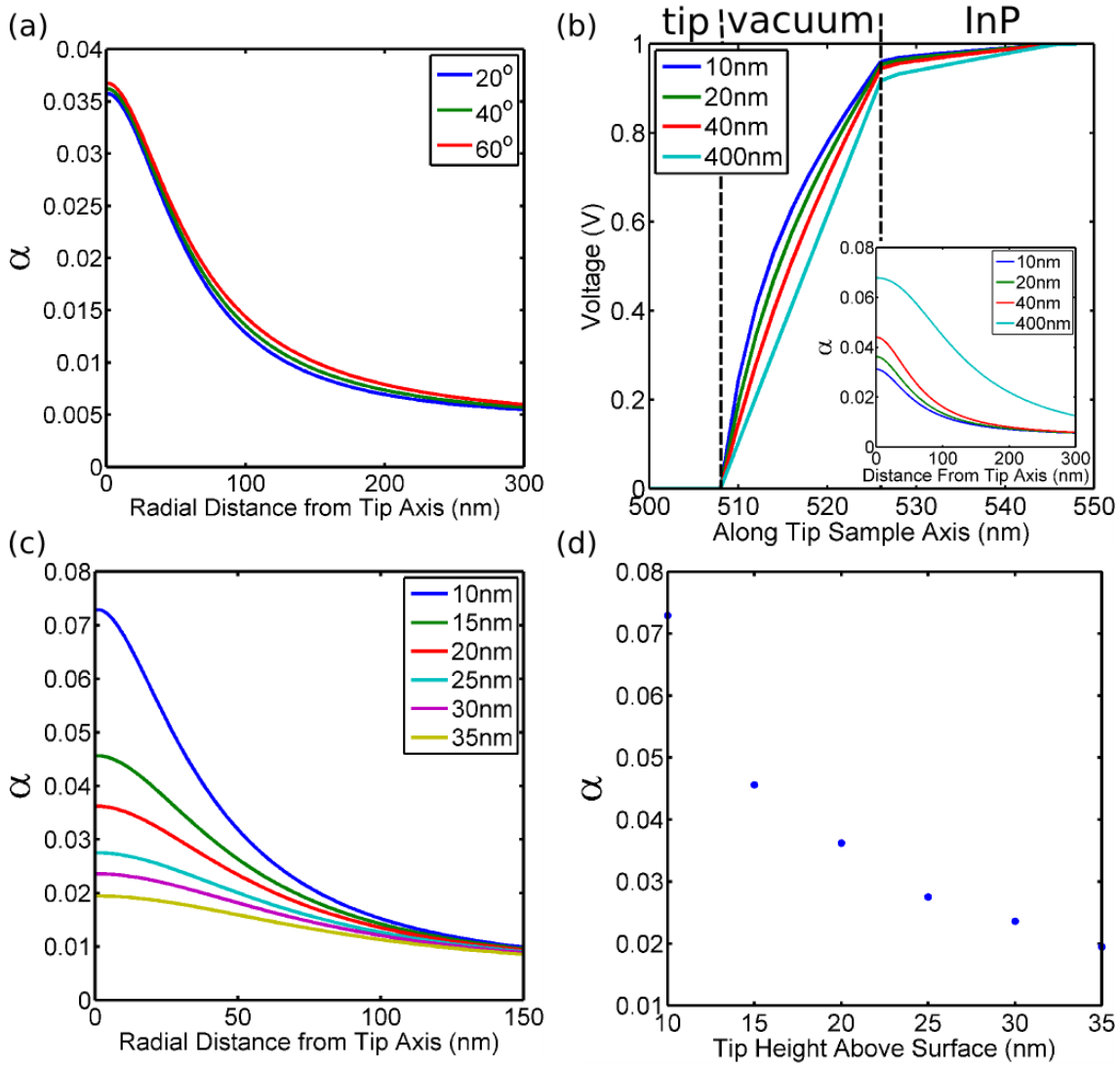

Figure 4–10: Change in α for different tip cone angles (a) and radii (b). In (a) the tip radius is 20 nm and in (b) the tip cone angle is 40°. For (a) and (b) the tip-sample gap is 20 nm. The change in α along the surface for different tip-sample distances (c) for a tip with 20 nm radius and 40° cone angle. In (d) the value in (c) directly underneath the tip is plotted to show how α changes with tip-sample gap.

The tip radius, however, has a much stronger influence on α. Fig. 4–10(b) and the inset show that a larger tip radius leads to a larger voltage fall-off between surface and 2DEG, and with increasing tip radius the result approaches that of a parallel plate capacitor. This is observed for the 400 nm tip radius where the voltage falloff between tip and sample is linear, and in the inset where the voltage falls off much more gradually as the distance from the tip axis increases. The voltage falloff along the sample surface gives an indication of how the α changes with lateral position which shows up in the AFM images, but in addition gives us an indication of the uniformity of the voltage over the quantum dot which would affect the confinement potential and dot wavefunction. We usually use a 20 nm tip-sample gap, and from Fig. 4–10(c), we observe little change (a maximum of 9 %) for the first 20 nm away from the tip-axis which corresponds to a 40 nm diameter dot. A diameter of 40 nm is a typical value for the diameter of the islands so it is reasonable to assume that the dots are less than this value. Finally, we plot the values from Fig. 4–10(c) for closest approach to show the change in α as a function of tip-surface gap in Fig. 4–10(d). From Fig. 4–10(d) we see that it is reasonable to assume a linear relationship between α and tip-sample gap over distances of 15 nm as long as the minimal gap is at least 15 nm.

Collecting data for comparison with the model for α is difficult because large voltages and small tip-sample gaps could result in field emission of tip material onto the sample. For this reason, at this point the model is used only for providing rough estimates of the lever arm.

Experimentally Determining the Lever Arm, α, E_C, and ΔE

In order to experimentally determine the lever arm, we need to heat up the sample and reduce a so that the peaks are thermally broadened and not broadened

by the oscillation amplitude of the tip. Currently, we are limited to an oscillation amplitude of approximately 0.2 nm before the oscillation is lost. Experimentally, in order to reach such small oscillation amplitudes, we need to disable the PLL safety feature which withdraws the sample when the PLL becomes unlocked. This needs to be done even while imaging because the PLL will intermittently become unlocked from the resonance frequency when using very small amplitudes, however for the majority of the time the PLL remains locked and the signal can be acquired. Although a less stiff cantilever would be more sensitive, in order to prevent a jump-to-contact event at small oscillation amplitudes it is important that the cantilever does not stop oscillating, and this is more likely to be achieved with a more stiff cantilever. This makes it difficult to reduce the oscillation amplitude even further without changing the microscope or cantilever design. One option may be to use a high-aspect ratio tip [54, 73]. These tips are long and thin which reduces the force on the tip shank and thereby lessens the risk of jump-to-contact.

For thermally limited peaks at a given tip-sample separation, we can obtain a quantitative value for α by fitting the peak to the expected lineshape using Eq. 2.38 (an example of fitting all six peaks to Eq. 2.38 is shown in Fig. 4–11). The value that we get, 0.036 ± 0.003, for the thermally broadened peaks [see Fig. 4–14(a)], agrees very well with the value expected by the electrostatic model (Fig. 4–10). [1]

[1] Since the lever arm is a function of the tip-dot and dot-2DEG capacitances, i.e. $\alpha = C_{tip}/C_{\Sigma}$, we can assume that it will not change as long as the cantilever is held at the same tip-sample separation. This is not necessarily the case if α is a function of voltage, for example due to band-bending or deformation of the dot confinement potential [4]. Since we obtain decent fits to all six peaks using the same value for α, we assumed that we could neglect these details. However, this does point out that, since each dot is different in size, α will be dot-dependent and so α needs to be determined for each dot.

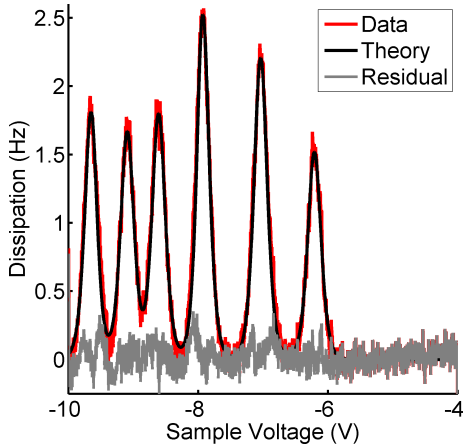

Figure 4–11: Residual plot of the dissipation compared to theory. Data was taken over an isolated quantum dot at 30 K with $a = 0.4$ nm.

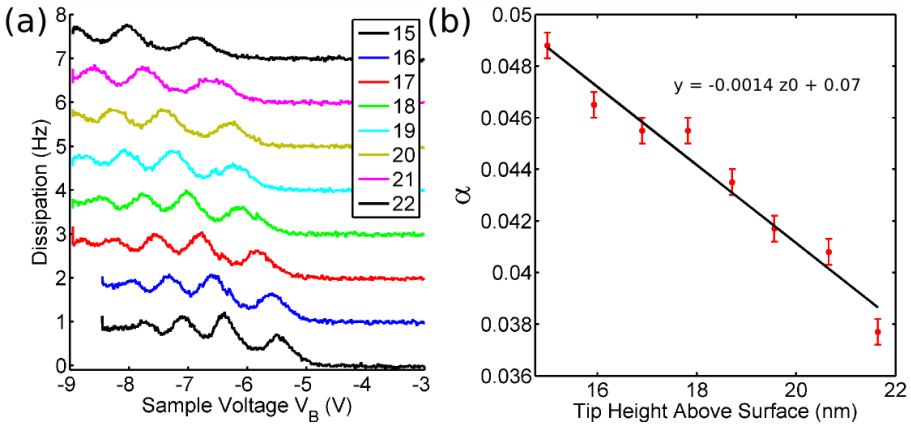

Figure 4–12: (a) Voltage spectra at different tip-sample gaps. (b) $\alpha(z_0)$ from the data in (a) with a linear fit. Data taken at 77 K.

For thermally limited peaks, such as those at 77 K, we can do voltage-spectra as a function of tip-sample gap distance, z_0, to obtain $\alpha(z_0)$ and confirm that over small distances α linearly depends on z_0. Fig. 4–12 shows this data.

If we plot the imaging voltage of the charge degeneracy point for each ring as a function of tip-dot distance, we can analyze the manner in which the rings spread out with distance and thereby determine $\alpha(r)$, with r being the distance between

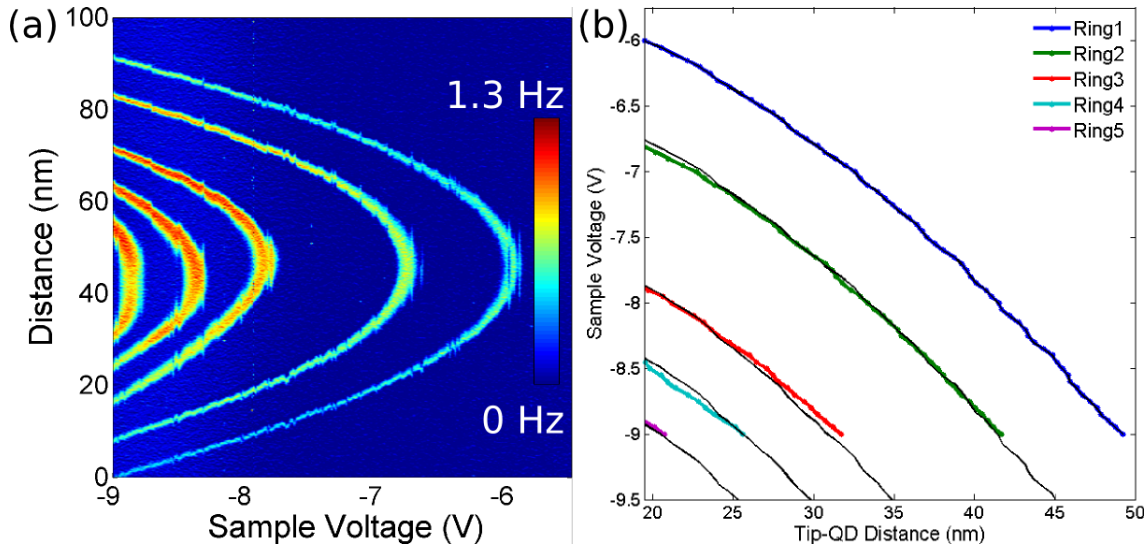

Figure 4–13: (a) 2D plot over the isolated dot in Fig. 4–2 created by repeatedly scanning over one line as a function of V_B. From (a) we can determine $\alpha(r)/\alpha(r_0)$ and, by knowing the separation in Coulomb blockade peaks at r_0, we can use this ratio to predict the positions of the other rings as shown in (b) for one half of the image in (a). In (b) we have used the change in the blue ring with distance to predict the positions of the other rings with position. The predicted locations are in black.

dot and tip, from a sequence of voltage images (for example, one could use Fig. 4–1). Alternatively, one can scan one line for several voltages and construct a voltage versus distance 2D plot as shown in Fig. 4–13(a) for the upper dot in Fig. 4–2. From Fig. 4–13(a) we can extract the ring voltage as a function of tip-dot distance. Since we know the charge degeneracy point must always be met in order to have tunneling, we know $\alpha(r)V(r) = \alpha_0 V(r_0)$ along the rings, where $\alpha(r)$ and $V(r)$ are the lever arm and voltage required to meet the charge degeneracy point at a tip sample distance r, and α_0 and $V(r_0)$ are the lever arm and voltage required to see the ring when the tip is directly over the dot. By plotting $\alpha(r)V(r)$ we observe that $\alpha(r)$ is well described by a linear relationship over these dot-tip distances. We can use this result to estimate the separation of the rings as a function of distance and compare the results to what we actually measure. This graph is shown in Fig. 4–13(b). In this graph, by accounting for how the lever arm decreases with distance r for the first ring (blue), we can account for the spreading out of the other rings (black lines). We can compare plots of data in Fig. 4–13(a) to the plots of the simulation in Fig. 4–10(a) and (c) to observe that the simulation captures the lineshape of the spatial dependence of α very well.

4.2.2 Calculating E_C From α

Once α is known, it is straightforward to obtain an estimate for the charging energy, $E_C = \frac{1}{2}\alpha e \Delta V$, where ΔV is the voltage difference between the first two peaks (as long as these energy levels are degenerate, e.g. due to spin-degeneracy). In the classical regime of Coulomb blockade the peaks will be evenly spaced with $2E_C$, however in the quantum regime the quantized energy level spacing can significantly affect the peak spacing. Not only are we able to detect the ΔE shell spacing, but in addition the peaks are not equally spaced and in fact move as a function of

temperature at different rates and directions due to level degeneracies (discussed in Chapter 2). These two properties make our values for E_C and ΔE estimates which can be improved by extrapolating to $T = 0$ K.

4.2.3 Determining the Shell Structure By Temperature

The shell structure can be determined by varying the temperature, oscillation amplitude, or magnetic field. Here, we do so via temperature which, to our knowledge, is the first time the shell structure has been verified using a temperature experiment even though the results were predicted theoretically in 1991 [86].

As discussed in Chapter 2, having degenerate energy levels within the dot shifts the Coulomb blockade peaks along the energy axis as a function of temperature. The rate at which they do so is determined both by the number of total levels ν, and the number of electrons n_{shell}, in a degenerate shell. Fig. 4–14(a) shows several voltage spectra taken over the same isolated dot at several temperatures. The positions of the maxima in the data in Fig. 4–14(a) have been repositioned in order to compensate for varying tip-dot distances influencing the peak separation, and so is useful only for demonstrating the lineshape fit at various temperature. To do this, all of the first peaks for each temperature were aligned and then the voltage axis of each curve was rescaled (by a maximum factor of 1.088) so that the second peak maxima was aligned with the corresponding theoretical peak maxima, and the amplitude of the peaks were left unaltered. However, the graphs in Fig. 4–14(b)-(c) plot the actual voltage difference in peak maxima as a function of temperature, where now these variations in peak location are represented with errorbars. The energy separation of the peaks is less sensitive to the tip position than the individual peak energies. The errorbars represent how well the difference between peaks was reproduced at one location and temperature, and therefore represents mainly the

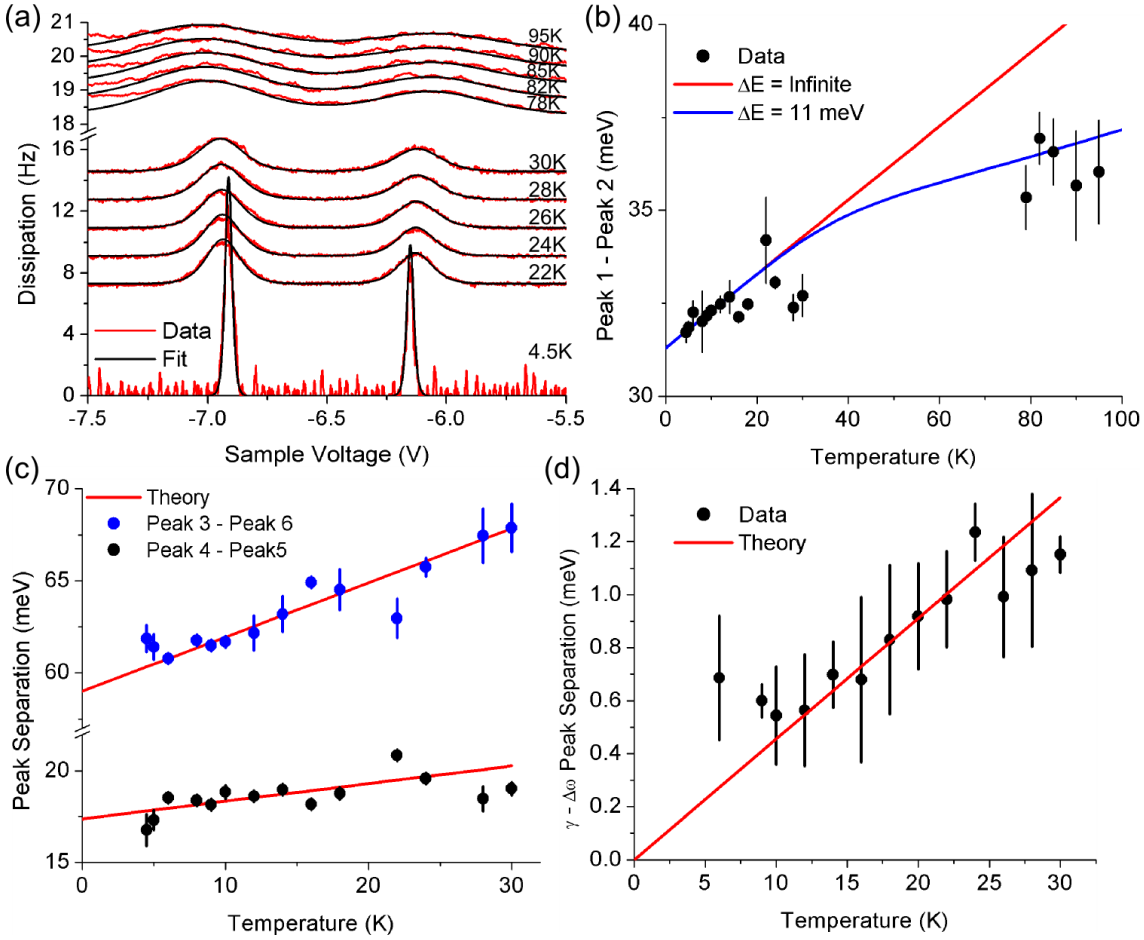

Figure 4–14: (a) The Coulomb blockade peaks of the first two electrons. Increasing the temperature broadens the peaks which is explained well by the theory (Eq. 2.38). (b) The separation between the first two peaks as a function of temperature. (c) The separation between peaks 3 and 6 and peaks 4 and 5 as a function of temperature. (d) Separation between the dissipation and frequency shift peak for the third peak as a function of temperature with theoretical fit. [67]

error in changing the tip-dot distance. For example, points that lie further from the general trend probably resulted from the tip being placed off center (i.e. not over the same location spatially) since at each temperature the dot center needed to be relocated, while points with large errorbars are probably the result of a change in tip-dot height (caused by piezocreep, for example).[2] By setting the energy derivative of Eq. 2.38 to zero to solve for the peak position as a function of T, we find the peak position is linearly dependent on the temperature with a prefactor that depends on ν, n_{shell}, and Γ (as long as we are in the $\Delta E << k_B T$ regime). The resulting slopes are plotted with the data where the only fit parameter is the $2E_C(T = 0)$ value which is 31 meV for this dot which agrees well with spectra taken at 4.5 K. The difference between peaks 2 and 3 at 4.5 K is 42 meV, so that we can estimate $\Delta E = 11$ meV. Fig. 4–14(b) is of particular interest because here we were able to determine the difference between the peak centers up to 95 K, and observed that these points did not follow the trend at all. However, at these temperatures the energy splitting between the s and p shells (approximately 11 meV) is comparable to the thermal energy of the electrons. In effect, this makes the s and p shells effectively degenerate, we can account for this numerically to obtain a much better fit to theory (blue curve) [67]. These added levels make the second peak belong to the first half of the new shell versus the second half of the s-shell and so it reverses its direction of movement along the energy axis so that now the first two peaks are traveling in

[2] Since the sample needs to be retracted each time the temperature is increased (due to thermal expansion of the sample and changes to the cantilever Q and ω_0), at each temperature the center of the dot needed to be relocated, making these types of errors inevitable but they could be reduced by collecting more sets of data at each temperature.

the same direction (but the separation between them is still increasing). Not shown here is the observation that the distance between the centers of the s and p shells decreased with increasing temperature. We believed this is caused by the repulsion of the s and p shells by the more degenerate d shell (expected to be 6-fold degenerate). Finally, it is possible that the deviation from the trend at the lowest temperatures in Fig. 4–14(c)-(d) is caused by the energy levels within the shells being no longer degenerate at this temperature (at 4.5K, $k_BT \sim 0.4$ meV). This could be caused by a deformed confinement potential or other effects.

From Eq. 2.38 and Eq. 2.37, we expect the peak maxima in the frequency shift and dissipation to not exactly line up. This can be observed in a single voltage-spectra and is more enhanced for peaks with a greater asymmetry between the number of ways to add and remove an electron. In Fig. 4–14(d) we show the result for the third peak (from the right in Fig. 4–11) plotted from the same data as the other graphs in this figure. That the differences between the positions of the maxima of the corresponding $\Delta\gamma$ and $\Delta\omega$ peaks agree to the theory over such a large temperature range further supports that the thermal shifting of Coulomb blockade peaks in Fig. 4–14(b)-(c) are caused by degeneracy, and not some other more exotic temperature dependent process [67].

4.2.4 The Tunneling Rate, Γ

For data with thermally limited peaks, we can obtain the tunneling rate Γ. In order to use Eq. 2.39, we first need to know which peak belongs to which energy shell in order to calculate ϕ. This was done via a temperature dependence experiment explained in the previous section. From the voltage spectra shown in Fig. 4–15, we can measure everything else that we need in order to calculate Γ for each peak. Doing so gives the following Γ from the first (rightmost) to the sixth peak: 70, 90, 160, 180,

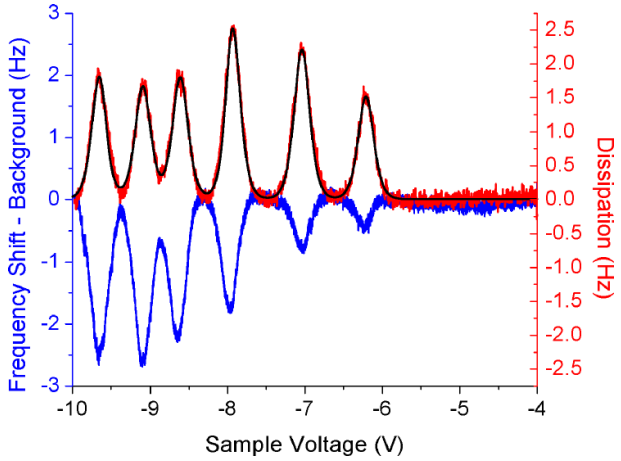

FIGURE 4–15: The dissipation and frequency shift spectra taken simultaneously over the isolated quantum dot at the top of Fig. 4–2. The parabolic background of the frequency shift has been subtracted. The peak widths are thermally limited for this spectra: $T = 30$ K, $a = 0.4$ nm. [67]

230, and 330 kHz. As expected, the tunneling rates increase with increasing electron number since this corresponds to a larger V_B which reduces the dot-2DEG tunneling barrier. Note that the large parabolic background in the $\Delta\omega$ has been subtracted in Fig. 4–15.

4.3 Multiple Quantum Dot Complexes

Since the quantum dots are influenced by the electrostatic environment, intuitively we expect each dot to also be influenced by the charges held in near-by dots. This dependence manifests itself in images where abrupt jumps in ring radii can be observed whenever rings from separate quantum dots are about to intersect. When the abrupt change is observed, we say the rings "anti-cross" at the location referred to as the "triple-point" for two dots, "quadruple-point" for three dots and so on. This is the vocabulary used to describe the identical features in a charge stability diagram obtained from a transport or charge-sensing measurement.

The relative magnitude of change in ring radius indicates how strongly the dots are coupled. Weakly coupled, or capacitively coupled, dots mutually shift their degeneracy points due to the Coulomb repulsion from electrons on the other dot. This happens for dots separated by relatively large distances (tens of nanometers) and results in a small change in ring radius. Strongly coupled, or tunnel coupled, dots tend to be very close together (less than 20 nm) and a small potential barrier between dots makes sharing an electron a possibility. The shared electron can tunnel between the two dots so that its wavefunction spans the whole dot. These types of dots are sometimes referred to as "artificial molecules", akin to the isolated dots being referred to as "artificial atoms." The change between the two types of coupling is gradual and thus hard to distinguish with certainty. One intermediate stage of the coupling involves a higher order tunneling process where dots are capacitively coupled but instead of sharing the same electron, an electron from each dot co-tunnel simultaneously with the 2DEG so that one level is emptied while the level in the other dot is occupied by a different electron [51]. Unlike that for the tunnel coupled quantum dots, this co-tunneling process is a decoherent process and there is no reason to assume that the spin of the new electron will be the same after the switch. [3] In our images, we can easily distinguish between weakly and strongly coupled quantum dots, however we need to do more analysis to be able to distinguish

[3] There are other decoherence processes that the quantum dots are subjected to which will lead to the electron losing its initial spin configuration, such as the spin-orbit and nuclear-spin interactions. Tunnel coupled quantum dots are not immune to such sources of decoherence. [9]

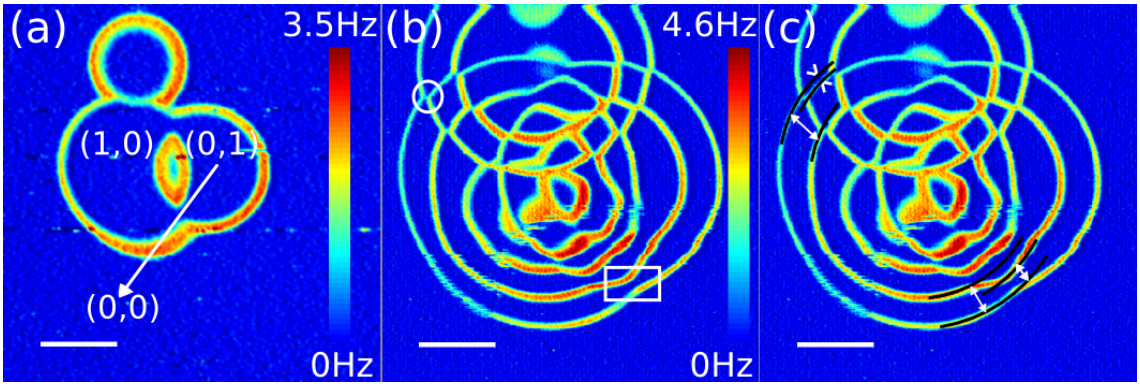

Figure 4–16: Dissipation images taken over the same region containing three quantum dots at -7.6 V (a) and -9.0 V (b) at 4.5 K. Images (b) and (c) are identical. In (b) the anti-crossing of the first rings from the upper and left quantum dots is circled and the anti-crossing of the first rings from the right and left quantum dots is boxed. The markings overlayed on (c) are showing the required distances needed to use Eq. 4.1 as explained in the text. Note how the distance between the first two rings is measured as close as possible to the change in ring radius and is not taken as a constant value over the whole dot. Scalebar is 20 nm. [67]

between strongly coupled dots which are tunnel coupled compared to those using co-tunneling processes. This is a topic of further study and is discussed in Chapter 6.

4.3.1 Quantifying Dot Coupling

In order to quantify the dot coupling, we need to have α for each dot so that the dot capacitance can be known from E_C. However, since we need a thermally limited peak to determine α, and the smallest oscillation amplitude we could use prevents the peaks from being thermally limited at 4 K, we instead compare the relative coupling between dots. We do this for a system of three coupled dots and show that the dot of interest is much more strongly coupled to one dot over the other.

Fig. 4–16 shows dissipation images of the same three dots taken with $V_B = -7.6$ V (a) and $V_B = -9$ V (b). The smaller V_B in Fig. 4–16(a) makes the three dots

easier to identify, since each dot is surrounded by only one ring. Following the arrow in Fig. 4–16(a), although starting in the right dot in the $(n_{left}, n_{right}) = (0, 1)$ state (for the number n of electrons in each dot), we can move the tip into the left dot [into the $(1, 0)$ state] without crossing a line of dissipation. The lack of dissipation implies that single electron tunneling has not occurred, but does not rule out higher order tunneling processes such as a co-tunneling process. Notice, for example, that we cannot do this with the upper quantum dot. This is an indication that the left and right dot are much more strongly coupled than either dot to the upper dot.

We can characterize the coupling by comparing the ratio of change in ring radius to the spacing of the first two rings for the left dot as it interacts with the upper and right dot. In Fig. 4–16(b), these two areas of interest are highlighted with a circle (interaction with upper dot) and a box (interaction with right dot). Notice already that it is clear that the more weak interaction leads to less distortion of the rings.

Since we confirmed that α is linearly dependent on the distance from the dot center, we can take an image such as Fig. 4–16(b) and measure directly off the image the values needed to make the comparison. Note that in order for α to linearly depend on lateral distance (as in an image) and not the total distance, which takes into account the tip-sample gap, the measurements made off of the image need to be at least 20 nm from the dot center. In order to be as accurate as possible, it is best to measure the values for $2E_C$ (i.e. the distance between the first 2 rings) as close to the change in ring radius as possible. This procedure helps to compensate for the discrepancy between the spacing of the first two rings over relatively large distances. Fig. 4–16(c) shows an example where the distances are roughly indicated. From this figure, for interactions with the upper dot, we measure the change in radius for ring 1 as $\Delta V_m = 1.0$ nm and the distance between ring 1 and 2 as $\Delta V_C = 10.0$ nm.

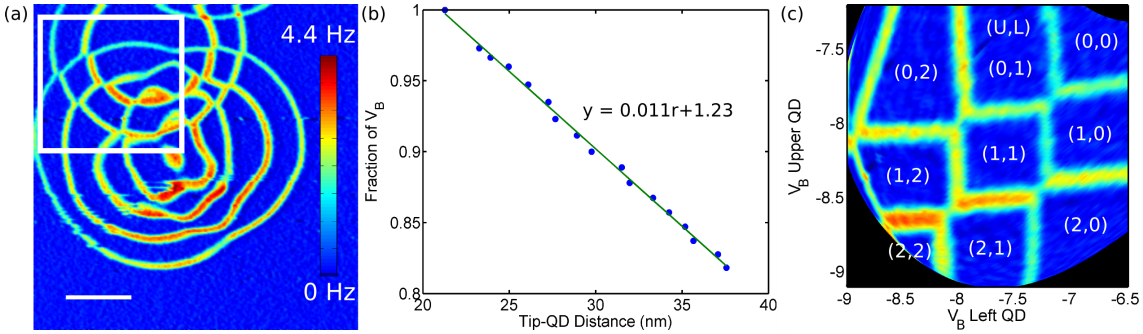

Figure 4–17: Dissipation image shown in (a) is over the same three dots as in Fig. 4–16(a)-(b), but at V_B = -8.8 V. (b) By taking several images over the same dots at different voltages and measuring the position of a ring with voltage, the voltage falloff as a function of tip-dot distance can be fitted to a line [this curve was deduced for the first ring of the left dot in (a)]. The equation of this fit provides the conversion from distances to voltage so that the stability diagram with axes in Volts can be created (c).

Similarly for interactions with the right dot, we measure the change in radius for ring 1 as ΔV_m = 3.8 nm and the distance between the ring 1 and 2 as ΔV_C = 9.1 nm. The ratio of these quantities is equal to the ratio of the electrostatic coupling energy, E_{Cm} (i.e. the energy change of the dot resulting from an electron in the other dot), and the charging energy of the dot [87]:

$$\frac{\Delta V_m}{\Delta V_C} = \frac{E_{Cm}}{E_C} \tag{4.1}$$

Using Eq. 4.1 and the quantities measured from Fig. 4–16(c), we calculated that the left quantum dot is coupled approximately 4.2 times more strongly to the right dot than to the upper dot. It is clear that if α is known, then by using Eq. 4.1, E_{cm} can be directly measured. Note that the dots become more and more strongly coupled as $E_{Cm}/E_C \to 1$ [87].

4.3.2 Converting AFM Images to Charge Stability Diagrams

To emphasize further that AFM measurements provide as much information as transport measurements, in this section we convert our images into "conventional" stability diagrams. We will take the dissipation image in Fig. 4–17(a), taken at -8.8 V, and focus on the region of anti-crossings between the left and upper dots. First we analyze the change in α as a function of tip-dot distance, which we can deduce by tracking the change in location of a ring over images taken at multiple voltages as discussed in Section 4.2.1. This gives a linear relationship, shown in Fig. 4–17(b), and this relation converts the tip-dot distances of Fig. 4–17(a) into voltages. Each dot will have a different conversion equation, and both are required. The number of dots determines the dimensionality of the resulting plot. For example, the axes on a two dimensional plot corresponds to the voltages across two different dots, i.e. $\alpha_1(r_1)V_B$ and $\alpha_2(r_2)V_B$ with V_B being the voltage used during imaging (-8.8 V here). The two-dimensional plot most closely resembles a conventional stability diagram where two voltages are swept (the source and gate voltages, for example). Fig. 4–17(c) shows the resulting stability diagram with occupation numbers for the upper (U) and left (L) dots given in parentheses.

4.4 Verifying the Shell Structure Via Strong Coupling Measurements

Chapter 2 covered the theory for a strongly coupled cantilever and dot. One main result was that the peaks skew away from the center of the shell as a result of the asymmetry between the rates to add and remove electrons to the dot [53]. Fig. 4–18(a) shows the voltage spectra for three large oscillation amplitudes and a theoretical curve of what would be expected in the weak coupling regime (i.e. the thermally broadened peaks) at 5 K and Fig. 4–18(b) shows just the first peak compared to the theory developed in Ref. [53]. The large oscillation amplitudes

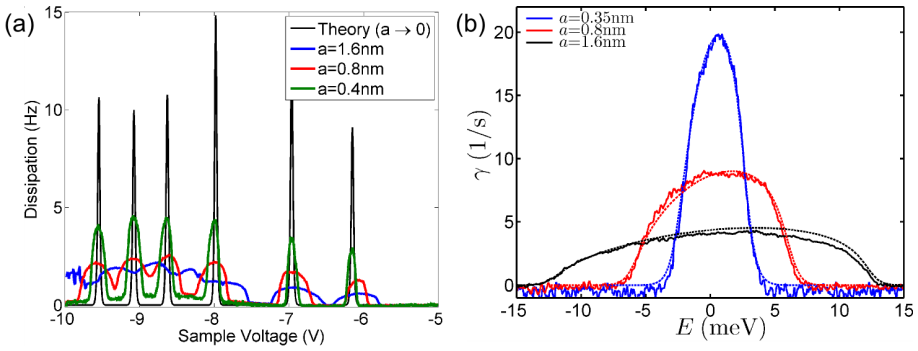

FIGURE 4–18: (a) Three spectra at different oscillation amplitudes (in the strong coupling regime), taken over the same dot, are compared to the theoretically displayed thermally limited peaks in black (which represents weak coupling). With increasing oscillation amplitude, the peaks clearly skew away from the center of the shell. (b) Comparison between strong coupling theory and data for the first peak for different oscillation amplitudes [53]. All data shown was taken at 5 K. (b) is courtesy of Steven Bennett.

flatten and broaden the Coulomb blockade peaks. In addition, it is clear that the peaks are skewing away from the center of the shell, i.e. the first two peaks (from the right) skew in the opposite directions, while in the p-shell the first two and last two skew away from each other. This implies that the dot has an s-shell consisting of two degenerate levels and a p-shell consisting of four. This is in agreement with the temperature analysis discussed earlier in this Chapter which was done on the same dot. For more details on the strong coupling regime see Ref. [53].

CHAPTER 5

The Quantum Dot Environment

As touched upon in previous chapters, the confinement potential of the quantum dot is influenced by its electrostatic environment. For semi-conductor based devices, an understanding of the electrostatic environment is crucial to control device noise, operation point, and failure rates. Further, we can imagine controllably manipulating the electrostatic environment to achieve a desired outcome. In this chapter, we show that the sensitivity of electrostatic force microscopy [41, 44, 46] combined with its high spatial resolution, provides a powerful way to characterize the electrostatic environment of the sample. Although STM can be used to characterize localized states or charge traps with high spatial resolution [88–90], this method requires conductive samples and so is limited in its applicability to semi-conductors, quantum dots, and molecules on insulators. Electrostatic force microscopy experiments combined with shuttling charges between tip and sample has led to the identification of charge traps within thick dielectrics which cannot be accessed by STM [43–45]. Here, we use electrostatic force microscopy to characterize charge trap noise that is originating from the shuttling of charge completely within the sample. Charge sensing techniques, such as the AFM technique described herein, have the

added benefit of the noise not being influenced by the electrodes, which complicates the analysis. Other examples of charge sensing techniques that have been used to characterize charge noise are quantum point contacts [10,91], single electron transistors [12,13], and scanning single electron transistors [27], but these methods currently do not possess the high spatial resolution of AFM.

We focus on generation-recombination noise [92], induced through shining super-bandgap light on a semi-conductor surface and measuring the generation-recombination time of the charge carriers near the surface. In principle, the technique demonstrated here can detect the noise from any fluctuating charge mechanism (provided the microscope is sensitive enough to measure the charge fluctuation and the acquisition time is not affected by drift).

5.1 Generation-Recombination Noise In Semiconductors

Electrical noise can reduce or enhance the current through micro or nano-sized restrictions in channels since the usual culprits, charge traps, not only significantly modify the current flow through the channel but in addition locally gate the device. This is actually the main principle used in the design of a quantum point contact [10], and is similar to multiple quantum dots gating each other as we have seen in Chapter 4. A fluctuating charge near a quantum dot will also affect its ability to stay in a coherent state, which can be crucial for some applications such as maintaining a specific charge configuration of qubits in a quantum computer [9]. Photovoltaic devices also depend highly on the number of traps present, especially as devices continue to shrink in size, and recent AFM studies used EFM to highlight regions of photoinduced charging and to characterize the quantum efficiencies of polymer blends [93]. The quantum dots and the photovolatics both interact with light, but in opposite ways; the bound exciton created by light absorption needs to efficiently

separate in photovoltaic devices so that a current can be created, whereas in the quantum dot the exciton remains strongly bound due to quantum confinement and the charges cannot escape the depth of the potential well of the quantum dot and so recombine locally. [1] Both of these processes can be identified, through confirming the existence or lack of generation-recombination noise, by detection of continuous charge trapping and de-trapping. For example in photovoltaic devices the presence of traps often means that the charge carriers are recombining before they can arrive to the collector electrode, which is usually undesirable.

By choosing to study G-R noise on a semiconductor sample with quantum dots, we simultaneously demonstrate the detection of electron-hole pair separation and quantum confinement within the quantum dots, through the presence and absence of generation-recombination noise [94]. The fact that the noise was present over some regions of the sample but not others (i.e. over the quantum dots) allowed us to rule out the possibility that the noise was being caused by the influence of the laser on the cantilever (e.g. laser instabilities, laser heating, etc.), and additionally allowed for a demonstration of our spatial resolution. The main sample studied had the same growth parameters as the sample discussed in the previous chapter [81]: a 20 nm InP insulating layer separating surface self-assembled InAs quantum dots and the buried 2DEG. However, we note that control experiments on gold, silicon dioxide, and the same InP sample without InAs were all performed. Similar noise results to those presented herein were found on the InP sample, but the noise was absent on the gold and silicon dioxide sample. The absence of the noise in these last

[1] This is assuming that the quantum dot is not capped with a material which favours charge-pair separation.

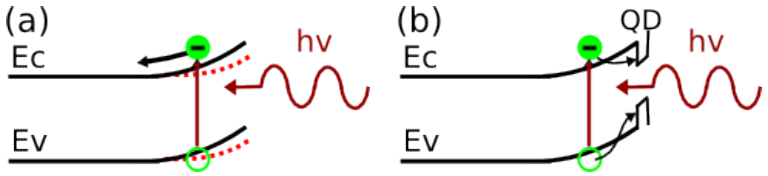

Figure 5–1: Schematic of the band bending of the InP sample. (a) Initially bands are bent upwards due to negative charge at the surface, but super-bandgap irradiation leads to holes traveling to the surface and recombining with negative charges to relax the bands. (b) Generated charge pairs are trapped in the potential well of the quantum dot where they recombine. [94]

two systems is expected as the gold does not undergo charge-pair separation through light absorption and the photon energy was not enough to span the large band-gap of the SiO_2 (9 eV).

The G-R noise results from the generation of electron-hole pairs upon super-bandgap laser irradiation, the charges then move in the electric field arising from charges trapped in surface states. Although the sample is neutral, near the surface there is upward band-bending due to excess negative charge being trapped in surface states, establishing a built-in electric field within the sample. This field separates generated electron-hole pairs and the holes recombine with these surface charges. This leads to large fluctuations in the surface charge which we are detecting via the electrostatic force[Fig. 5–1(a)]. Free electrons nearby the quantum dot will tunnel into the potential well of the dot, while free holes drift into the dot leading to recombination of charge pairs within the potential well of the dot [94]. The observations described in the following sections of this chapter elaborate more on this process and provide convincing evidence that this is indeed the observed mechanism.

5.1.1 Experimental Setup

After the 1550 nm laser was installed [73], changes to the microscope were made so that the previous laser, 780 nm wavelength, could be used to shine light onto the

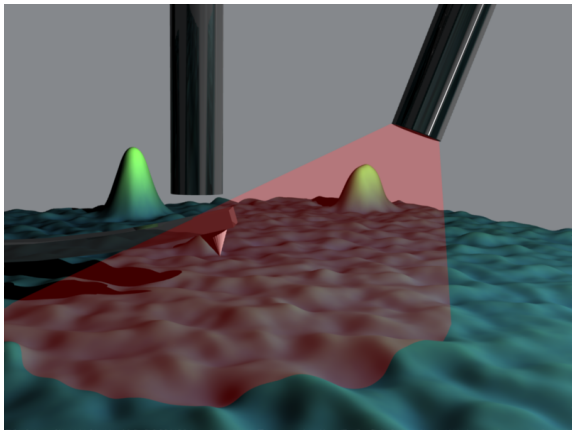

Figure 5–2: Schematic showing the cantilever positioned over the sample surface and the two fiber optics. The 780 nm light shines on the surface, while the 1550 nm light (invisible) shines onto the backside of the cantilever for the interference signal for position detection. We know that the cantilever does not block all of the light from this laser, as the resistance of the 2DEG decreases when this laser is on. However, stray light can be minimized by optimal cantilever-fiber alignment and reducing the gap between fiber and cantilever as much as possible.

sample surface. A schematic of the setup is shown in Fig. 5–2. The higher energy of the 780 nm laser (1.6 eV) exceeds all of the bandgaps of the InAs/InP sample. For example, at room temperature, the bandgap of InP is 1.35 eV, while for InAs it is 0.36 eV, both of which monotonically increase with decreasing temperature with an approximate increase between 0.05-0.1eV at 0 K [79]. We used an intensity of $\approx$ 150 nW/mm^2 for the 780 nm light. The thinness of the sample ensures that the vast majority of light completely penetrates beyond the 2DEG. Fig. 5–3 shows the graph that we use to convert the laser currents, read off of the laser power supply, into laser powers. We placed a photodiode on the AFM sample stage (a Hamamatsu Si PIN photodiode S6695-01) and approached it to the cantilever in order to mimic the experimental conditions of sample illumination. Fig. 5–3, however, only gives an estimate of the power since the fiber optic needs to be reconnected for each experiment, resulting in varying coupling losses. For this reason, the laser currents

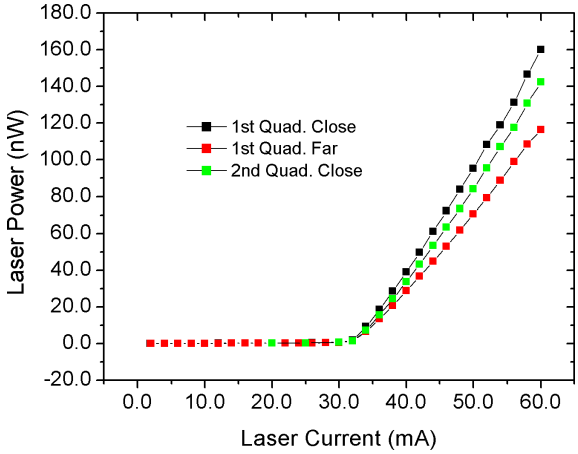

FIGURE 5–3: Graph for the laser current to laser power intensity. The first quadrant of the photodiode was underneath the tip, and approached to the sample (black) and the values on a nearby quadrant were also recorded (green) to give a feeling for the spatial variation of the laser intensity. Then, the photodiode was retracted approximately 1 mm away from the tip and the values were recorded for quadrant 1 (red) to show a distance dependence of the light intensity.

are often cited where one might expect to be given the laser power. Performing our experiments at a laser intensity where the bands have relaxed makes these differences in laser power less of an issue. The diode is 1 mm^2 in area, so the intensity of the laser can be read off of the $y-$axis in Fig. 5–3 in units of nW/mm^2.

The AFM is operated in self-oscillation mode. We use a Si cantilever from Nanosensors (PPP-NCLR) with a 10 nm Ti layer adhesion layer and 20 nm Pt layer sputter coated onto the cantilever. The experiments are done at low temperature (either 77 K or 4.5 K) because we do not detect an increase in noise with laser irradiation at room temperature. The reason for this is two-fold. Firstly, the thermal noise of the cantilever is larger, and secondly an increase in thermal energy of the sample electrons already allows for more background charge fluctuation. These two effects make it difficult to detect a change from the laser irradiation.

5.1.2 GR-Noise Imaging and Spectra

By comparing the electrostatic topography images of the surface, it is easy to observe the laser induced noise as the InP surface is covered with streaks in the fast scan direction. We emphasize here that the images taken via a standard topography approach (i.e. with constant $\Delta\omega$) are not representative of the topography of the surface since an applied V_B also results in electrostatic features showing up in the image. Fig. 5–4(a)-(b) compares images with laser off and on. The images give an indication of the uniformity of the noise over the wetting layer. We can learn more about the dynamics of the noise by positioning the cantilever over one location, shutting off the feedback, and collecting data on the frequency shift of the cantilever as a function of time. Fig. 5–4(c) compares an example of such a spectra taken over the wetting layer for 10 s. with the laser both on and off, to one taken over a quantum dot [Fig. 5–4(d)]. Since it is rare to see the noise in the dissipation channel, only the power spectral density (PSD) of the frequency shift is plotted and shown in Fig. 5–4(c)-(d). Since G-R noise results from the detection of several processes occurring randomly but with a characteristic time constant, by converting the time trace into the frequency domain via a Fourier transform, we can characterize this time constant by measuring the corner frequency of the PSD [95]. Since G-R noise is described by a Lorentzian frequency response, we expect the PSD to have a slope of approximately -2 at higher frequencies and to level off at low frequencies. Both of these features are shown in the PSDs in Fig. 5–5, where several PSDs generated from 600 sec. frequency shift acquisitions taken over the wetting layer are shown for different laser currents. Once the laser current exceeds 45 mA, the spectra reproduce themselves well and the corner frequency can be estimated. Fig. 5–6 shows two spectra taken at 2 V with 600,000 points over 600 seconds. The corner frequency of the data in

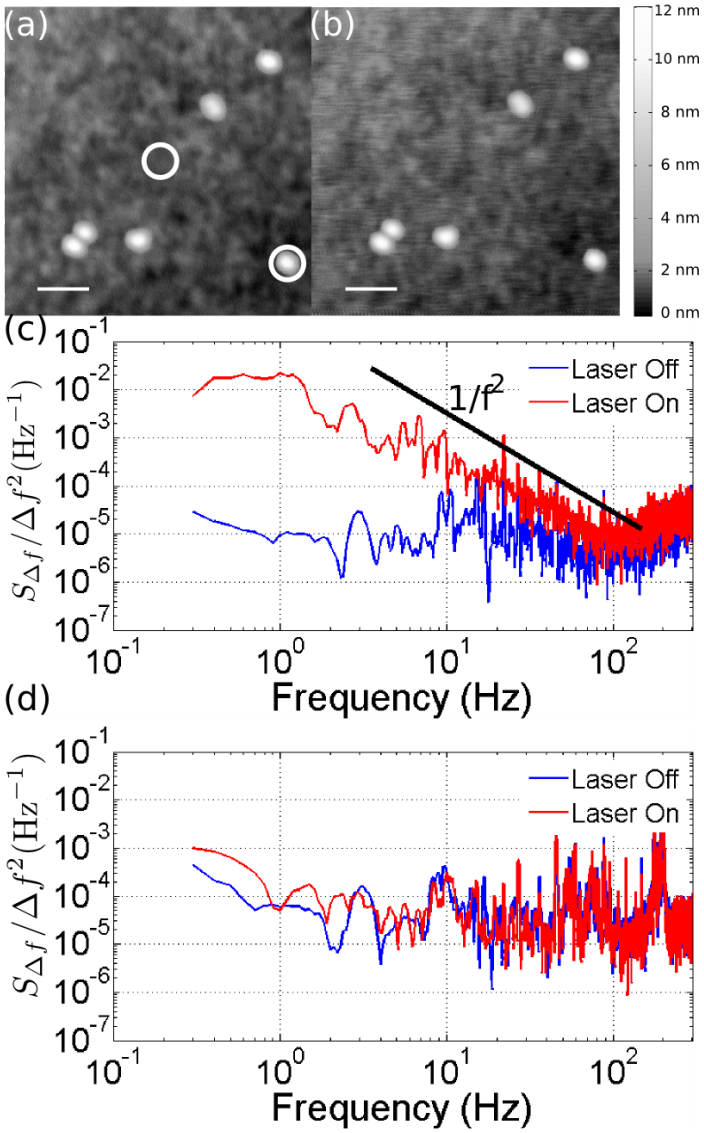

Figure 5–4: AFM Topography images taken at $V_B = 2$ V and -31.66 Hz at 4.5 K with laser off (a) and on (b). Noise from laser irradiation is observed in the topography image as streaks in the fast scan direction. PSD spectra taken over the wetting layer (c) and a quantum dot (d) at the circled locations in (a). The PSD spectra were created from 10 sec. time scans of the frequency shift while the distance feedback was off, each contains 10,000 points. Although the presence of the laser clearly affects the noise over the wetting layer, the noise over the quantum dot is unaffected by the laser irradiation. [94]

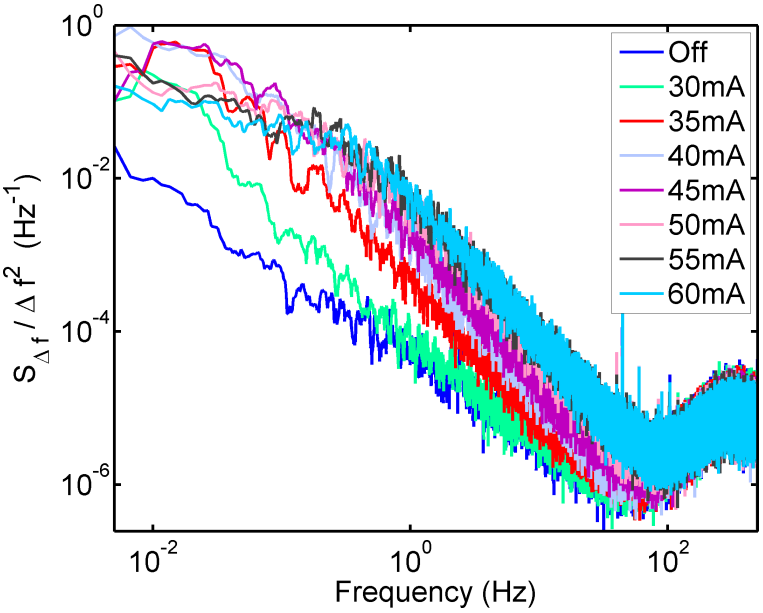

Figure 5–5: PSD of the frequency shift over the wetting layer for increasing laser currents. The frequency shift data consisted of 600,000 pts. and was collected for 600 s with $V_B = 2$ V at 77 K. The frequency shift data is treated with a Hamming window and the resulting PSD is subjected to a 15pt moving average.

Fig. 5–6 is estimated from the frequency at which the two lines in Fig. 5–6 cross. This gives a corner frequency of approximately 0.3 Hz, indicating a time constant of roughly 0.5 seconds, representing the average time with which the charge carriers are recombining.

Fig. 5–7 shows the PSD at different temperatures for data taken over the wetting layer, for the laser on and off at $V_B = 2$ V. The data taken at room temperature ("RT") consists of only 10 s and 10,000 pts, while the other two have 300 s and 300,000 pts. At room temperature, the tip position is considerably more unstable, and drift and piezocreep can make it difficult to keep the tip in the same position over the sample, making long time data acquisitions difficult. However, it is clear from Fig. 5–7, that the laser does not change the noise over the sample at room temperature. More data needs to be collected before we are able to characterize the

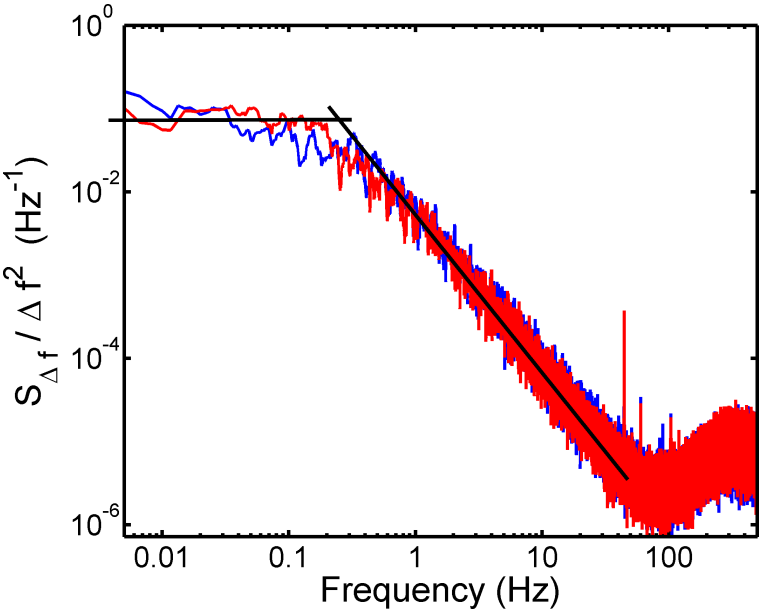

Figure 5–6: PSD of the frequency shift over the wetting layer for two sets of data. The frequency shift data consisted of 600,000 pts. and was collected for 600 s, at 77 K with $V_B = 2$ V. The corner frequency is estimated from where the slope of -2 intersects the flat region. The corner frequency is approximately 0.3 Hz. The frequency shift data is treated with a Hamming window before preforming the PSD and the resulting PSD is subjected to a 15pt moving average.

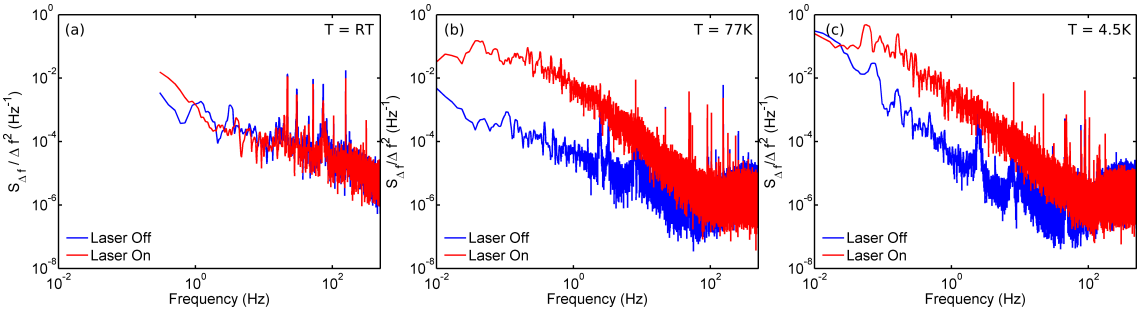

Figure 5–7: PSDs taken over wetting layer for multiple temperatures. All data taken with $V_B = 2$ V.

noise as a function of temperature (e.g. measuring the corner frequency as a function of temperature). The data should be taken over a longer time period so that there are more points in the region of interest, and many locations over the sample should be measured to rule out spatial variations leading to a change in the corner frequency.

The electric field in the sample resulting from the initial upward bending due to excess negative charge on the surface is modified by the bias voltage. Positive V_B (strictly speaking, $V_B > V_{CPD}$) complements the electric field of the sample, enhancing the bandbending and electric field, which more efficiently spatially separates the photo-generated charge carriers and leads to more charge fluctuations at the surface once the laser is turned on. Conversely, the electric field from negative V_B reduces the bandbending and so fewer fluctuations are observed. Fig. 5–8(a) shows these characteristics in the frequency shift as V_B is swept with both the laser on and off. When the laser is on, the net flow of minority carriers to the surface reduce the V_{CPD} (i.e. the difference between the work functions of the sample and tip is increased by the relaxation of the band bending) [96]. In addition, there is a larger electrostatic force between the sample and negative tip (corresponding to positive V_B) when the laser is on because of increased flow of positive charge to the surface [93]. Little difference between the laser on and off curves for negative V_B suggest that the bands

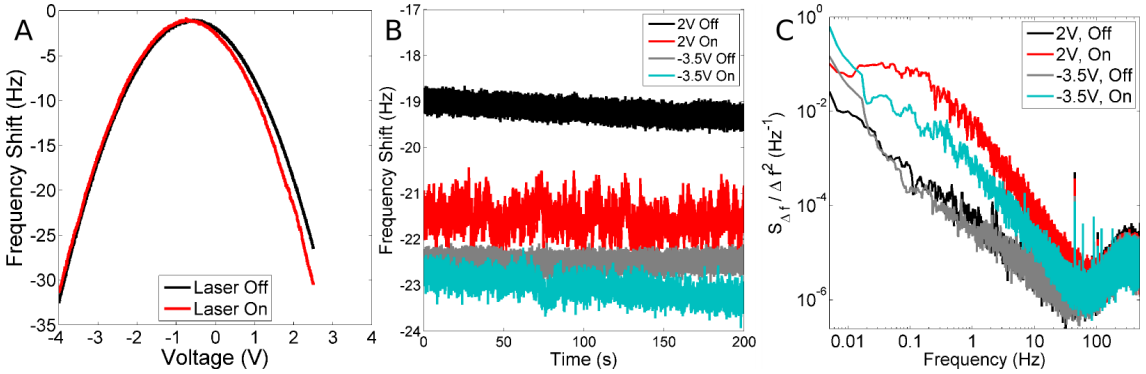

FIGURE 5–8: The frequency shift parabola resulting from sweeping V_B undergoes two changes with laser irradiation (a). First, the location in V_B where the apex occurs shifts to a more negative value, and secondly the parabola curvature increases. (b) Time traces (200 sec., 200,000 points) over the same location as (a) are shown for the laser on and off for V_B = 2 V and V_B = -3.5 V. It is evident from both (a) and (b) that the measured noise is larger for $V_B > V_{CPD}$. The corresponding PSD of the full 600 sec. which is partially shown in (b) is graphed in (c). Data taken at 77 K.

are already mostly flattened by the applied bias alone. The 200 s. time traces shown in Fig. 5–8(b) are taken over the same location as the parabolas in Fig. 5–8(a). Even from the time traces, it is apparent that the noise is greater at positive voltages. The corresponding PSD curves are shown in Fig. 5–8(c) using the 600 s. time traces [Fig. 5–8(b) is showing only 200 s. of these 600 s. acquisitions].

We can also estimate the spatial resolution of the noise by taking advantage of the lack of G-R noise over the QD and observing the onset of the noise as we approach the wetting layer [94]. Fig. 5–9 shows an image of a dot taken with the laser off, and the PSD curves with the laser on, taken over each location marked in the image. As we move off of the dot in 20 nm steps, we see a significant change in the noise in only one step, indicating a resolution better than 20 nm. It would be interesting to see a 2D plot of the amplitude of the noise over the entire sample surface, but automatic data collection is recommended since it would take several

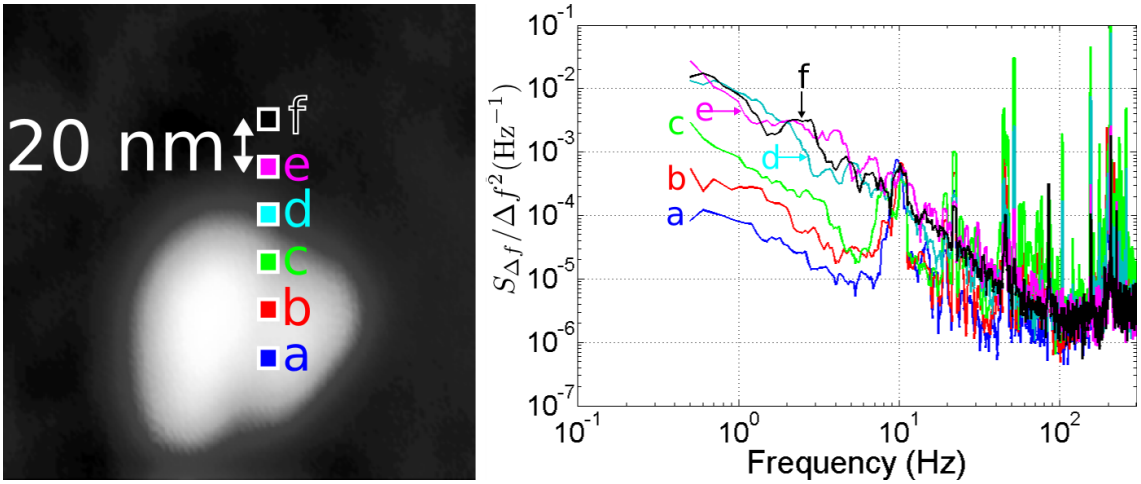

FIGURE 5–9: Topography image of a quantum dot where PSD spectra were taken at each spot labeled on the topography. The PSD spectra were made from 10,000pts frequency shift data collected over 10s at 77 K and 2 V. A clear increase in the noise is discernible between 20 nm steps. [94]

hours to do (for example, an image comprised of 50 × 50 pixels at 10 sec. will take 7hrs for the data collection alone).

5.1.3 Time Constant For Band-Bending

The time-spectra of the previous section were collected by placing the cantilever over one location, turning on the laser, and waiting for 5-10 s. before recording the time trace of the frequency shift. The wait time was crucial to ensure that enough of the minority carriers (holes) had migrated to the surface, so that we would be measuring solely the recombination process and not this migration. Fig. 5–10 shows a typical example of a time trace during which the laser was turned on and back off again. In such a time trace we see that the laser causes a large change in the overall electrostatic force (i.e. a large change in frequency shift), and it is also obvious that the initial process of "charging" the surface is much faster than "de-charging", where we consider the charging process as the movement of charge to the sample surface

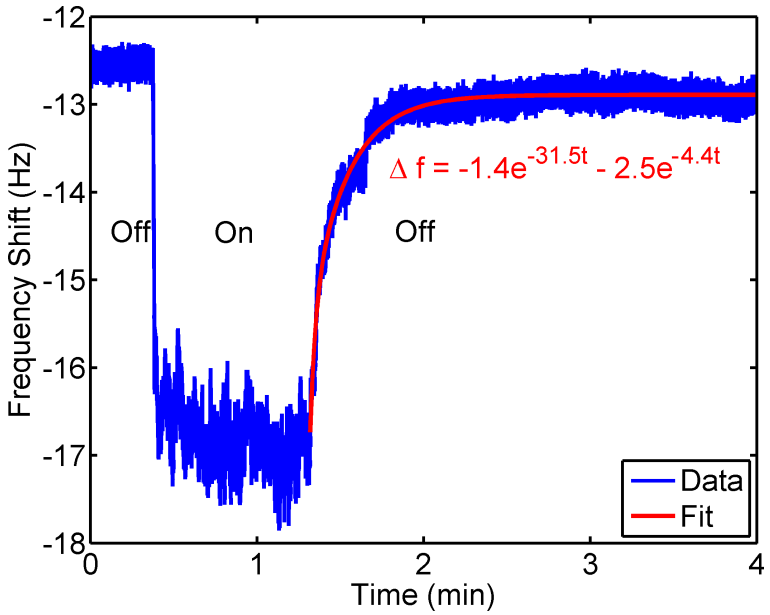

FIGURE 5–10: Time spectra for $V_B = 1.0$ V. The laser is initially off, but is turned on briefly and off again. The increase in low frequency noise is clearly visible while the laser is on. The frequency shift takes a relatively long time to return to its initial value, here we fit it to an exponential decay. For this spectra, we obtain a better fit to a sum of exponential functions with time constants of ~ 14 s. and ~ 2 s.

caused by the generation of free carriers. The two time scales of the data in Fig. 5–10 might represent the abrupt decrease in flow of minority carriers (due to the laser shutting off) while the longer decay rate may be representative of the decharging of the sample surface. More data is needed to get a better estimate of this value, and to understand the voltage dependence, temperature dependence, and the effect of the laser power on this time constant. The long "de-charging" process makes it very important to wait between time-spectra in order to give the sample enough time to reinitialize, however the wait time could be vastly reduced by simply changing the voltage to the opposite polarity corresponding to roughly the same frequency shift (all done with the feedback off to prevent the feedback from crashing the tip into the sample) which forces the de-charging.

5.1.4 Different Laser Powers and Kelvin Probe Force Microscopy For Surface Photovoltage Measurements

The surface photovoltage (SPV) is equivalent to the light induced, negative change in contact potential difference between two materials, i.e. $SPV(P) = V_{CPD}(P) - V_{CPD}(0)$, for laser power P. We can measure this in one of two ways; either with an EFM approach or with Kelvin Probe Force Microscopy [83, 97]. The latter method is discussed in the following paragraph. Recall from Eq. 2.18 that the minimum in the electrostatic force occurs at the applied voltage where the tip-sample contact potential difference is compensated for or canceled. This manifests itself in the frequency shift parabola obtained by sweeping the sample voltage, where the parabola apex occurs at this value. Thus, by sweeping the sample voltage at several light intensities, this minimum will shift towards a new value with increasing light intensity [recall Fig. 5–8(a)]. This shift is a measure of the band bending resulting from the migration of minority carriers to the sample surface and it eventually reaches an equilibrium when the bands are flattened, then there is no longer a space charge layer since there are enough minority carriers to recombine with the surface charge and null the built-in electric field. We took care to perform our G-R experiments in the laser intensity regime where the bands are flattened.

The Kelvin Probe Force Microscope [83] applies a modulated bias voltage between tip and sample and uses an additional lock-in to track the magnitude of this signal. This signal is used to determine the bias voltage needed to cancel the V_{CPD} between tip and sample. This voltage is applied to the sample and tends to improve imaging resolution of the topography because it nearly cancels the electrostatic force component, and in addition simultaneously provides an image of the V_{CPD} variations. Unlike in EFM where the V_B is affecting the bandbending of the sample, the Kelvin Probe Force Microscope approach has a minimal effect on the bandbending

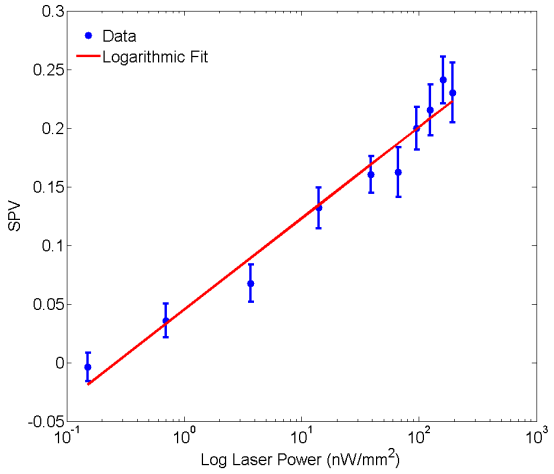

FIGURE 5–11: Logarithmic dependence of surface photovoltage on laser power.

since the tip and sample have a minimized contact potential difference. We performed the same experiment with the Kelvin Probe Force Microscope as with the EFM technique, but this time measured the compensating voltage as a function of time. As with the frequency shift in the previous case, we observed increased noise in this voltage channel when the laser was on. For different laser powers, we can use the Kelvin Probe voltage to plot the resulting average change in the surface photovoltage and observe the characteristic logarithmic dependence on laser power that is expected for an SPV measurement (Fig. 5–11) [98]. In this experiment, the modulated voltage had a 0.6 V_{rms} amplitude and 1 kHz frequency, and the time constant of the Stanford Systems lock-in was 300 μs.

CHAPTER 6

Outlook and Conclusions

AFM, and in particular electrostatic force microscopy, is a useful tool for measuring the energy levels of quantum dots and characterizing noise caused by charge fluctuations. The main benefit of using AFM over conventional approaches is the spatial resolution and the ability to link the topography to other information (e.g. force information, charge noise, etc.). Using the AFM to probe electrostatic properties will not only aid in device diagnostics but also in furthering our understanding of physics at the nanoscale; this was demonstrated in particular for semi-conductor quantum dots. The results that we have obtained using the AFM have motivated us to pursue a number of other energy-level probing experiments and these are discussed below.

6.1 Outlook: Furthering our Understanding

6.1.1 Magnetic Field For Verifying Shell Structure

Electron addition spectra as a function of magnetic field should produce a Fock-Darwin [99,100] spectra for our quantum dots. The Fock-Darwin spectra is the name given to the electron addition spectra versus magnetic field for a disk-shaped quantum dot with parabolic confinement potential having two electrons in the first energy

shell, four in the second, six in the third, and so on. It does not account for many-body interactions [101]. Since the energy levels are shifted with magnetic field due to the electron angular momentum (and also the Zeeman effect), from such spectra we can directly label the quantum numbers of each electron and thereby determine the shell structure. As we have a superconducting magnet installed capable of 8 T, we intend on carrying out this experiment which would close the loop on the shell structure analysis. However, it will be a challenging experiment mainly because of the increased noise from the magnet power supply in combination with the magnetic components of the microscope moving with magnetic field. The Fock-Darwin energy levels are described by [4, 101]:

$$E_{nl} = (2n + |l|)\hbar\sqrt{\omega_{\Delta E}^2 + \frac{\omega_c^2}{4}} - \frac{1}{2}l\hbar\omega_{\Delta E} \tag{6.1}$$

Where n is the radial quantum number and l is the angular momentum, $\omega_c = eB/m^*$ is the cyclotron frequency in magnetic field B for effective mass m^*. For InAs, $m^* = 0.028m_0$ [79] for free electron mass m_0. Finally, $\hbar\omega_{\Delta E} = \Delta E$ is the energy separation between shells. The Zeeman splitting of the energy levels is:

$$E_Z = \pm 0.5 g \mu_B B; \tag{6.2}$$

With g being the g-factor and μ_B the Bohr magneton. Fig. 6–1(a) shows the theoretically calculated Fock-Darwin and Zeeman splitting as a function of magnetic field for an InAs quantum dot with $\Delta E = 11$ meV similar to the dot studied in Chapter 4. Notice in Fig. 6–1(a) that the Zeeman splitting is responsible for the noticeable spin split of the energy levels. In this calculation, the g-factor for InAs was taken as the bulk value of $g = -14.7$, but the measured g-factors for InAs quantum dots can be substantially different than that value. In Ref. [102], experiments on InAs quantum

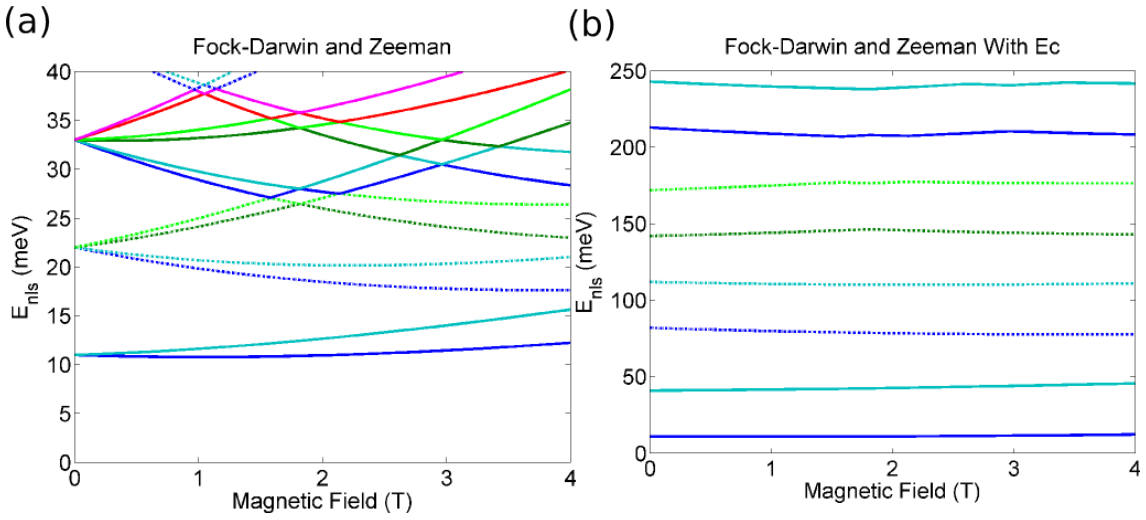

Figure 6–1: (a) The Fock-Darwin and Zeeman energy level splittings up to 4 T are plotted for an InAs dot with ΔE=11 meV. In (b) the charging energy is added to each curve. The first two energy levels of each shell are coloured blue, the next two green, and the next two red. The energy levels of the second shell are plotted with dashed lines to make it easier to tell the levels apart.

dots formed in nanowires found the absolute values of the measured $g-$factors to be between $2-18$ and depended on a number of factors, with smaller dots having the smaller values. However, one reason for such a large range of values is partially due to the difficulty in accessing several single dots (the experimental technique used required electrodes to be attached to the wire). It would be interesting to measure the g-factor of several individual dots to determine the variation in this value for our dots, but the magnitude of the value used here is almost certainly too large. In Fig. 6–1(b) the same curves are plotted as in Fig. 6–1(a), but now we incorporate the charging energy, $E_C = 30$ meV, which spaces out each of the curves. Our data will look similar to Fig. 6–1(b).

The radius of the Fock-Darwin eigenstates is proportional to $1/B$ and so increasing the magnetic field shrinks the electron wavefunction. At high magnetic fields, the Fock-Darwin levels group into the free electron Landau levels, with Landau quantum

number $n + (|l| - l)/2$ [101]. In Fig. 6–1(a) the lower 8 levels are grouping into the first Landau level. When Coulomb interactions are considered, the decrease in electron wavefunction with increasing magnetic field leads to a higher concentration of electrons on the dot, increasing the Coulomb energy. Since the wavefunction radius increases with angular momentum, it eventually becomes favourable for the electron to increase its angular momentum to reduce the Coulomb energy [101]. Since the radius of the wavefunction affects the dot properties and how strongly it couples to nearby dots, we may observe this effect indirectly in our measurements.

6.1.2 Excited State Spectroscopy

Now we consider oscillating the cantilever with such a large amplitude that a single electron (since we are in the Coulomb blockade regime) can be given enough energy to enter into an excited state of the dot. In other words, an electron that would have entered the s-shell enters the p-shell. This is analogous to the transport measurement done in [6], where a quantum dot was essentially coupled to only one of the two electrodes and a square pulse wavetrain injects an electron into, and then out of, the dot. The size of the pulse was slowly increased from the value required for overcoming the charging energy but not to the point where it reached twice the charging energy, and so only one electron is able to enter the dot. In this intermediate region, the pulse becomes large enough that an excited state also becomes available for the electron to tunnel into (as opposed to solely the ground state). The availability of two states changes the tunneling rate of the electron and, since their measurement technique is sensitive to the tunneling rate, they observe this change in their signal.

In our experiment, by increasing the oscillation amplitude access to more energy levels is provided for the incoming electron. Allowing for tunneling into excited states

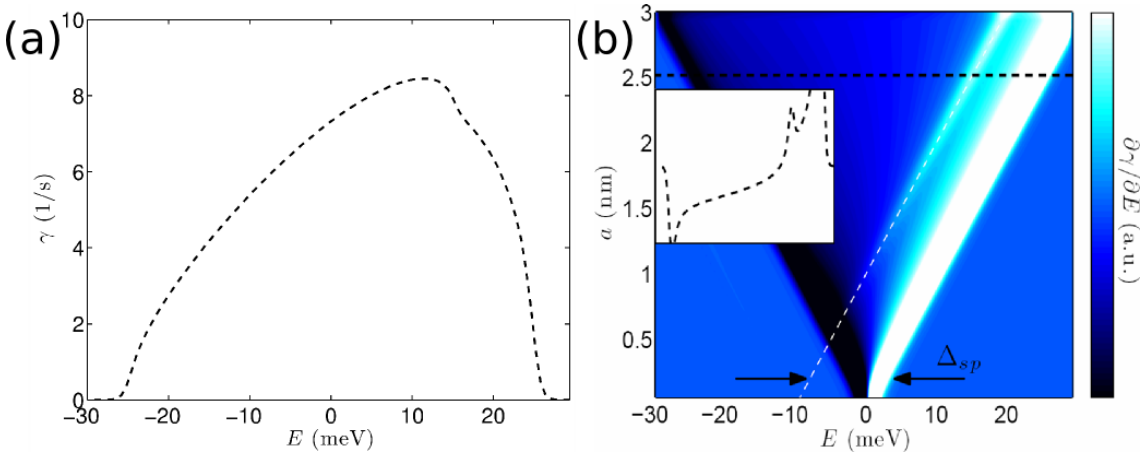

FIGURE 6–2: (a) A bump on the Coulomb blockade peak is an indication that the cantilever oscillation amplitude is large enough to permit the electron to enter an excited state of the dot. (b) Theoretically, taking several curves at increasing oscillation amplitudes and plotting the derivative of the peak, the onset of this bump is obvious (dashed line) and the splitting of the shells (Δ_{sp} since this is the first peak) can be determined from the spacing between the dashed line and the line marking the onset of the peak. An example of one slice of the peak derivative at a larger amplitude is given in the inset. [53] Image is courtesy of Steven Bennett.

increases the dissipation, and a small "bump" on the dissipation peak appears [an example for the first peak is shown in Fig. 6–2(a)]. Taking multiple curves as a function of oscillation amplitude allows us to determine the splitting between energy shells [Fig. 6–2(b)]. [53]

Preliminary data indicates that we may have observed this phenomena, but having few dissipation-voltage spectra at several amplitudes makes this bump on the dissipation peak difficult to identify, and so to be sure this experiment needs to be done for several oscillation amplitudes. The type of dot that one wants to study using this technique is one with a large E_C so that the peaks are spaced out enough that we can use relatively large oscillation amplitudes to observe this bump before the peaks smear into each other.

6.1.3 Additional Dissipation Features

While most AFM experiments ignore the information in the dissipation channel, our group spends a lot of time analyzing this information and have found a number of observations which are interesting but have not been previously reported. Two such observations are expanded on below.

Enhanced Contrast In Dissipation

Two separate experiments had a single peak in the dissipation-voltage spectra which was not associated with any feature on the sample, and in particular was not associated with the quantum dots, and interestingly when the voltage was set near to this peak in dissipation we could obtain very impressive spatial resolution in the dissipation channel (compared to the resolution of all of the channels of our microscope). Fig. 6–3(a) shows the dissipation$-V_B$ spectra taken over the wetting layer, with a sharp jump/peak in dissipation around 1 V. While taking an image at $V_B = 1$ V the dissipation contrast abruptly changes, as emphasized in Fig. 6–3(b) by an arrow (slow scan direction is downwards). Fig. 6–3(c) and (d) are the dissipation and simultaneously recorded electrostatic topography images taken afterwards at $V_B = 1.2$ V. Here, the dissipation images are taken with the distance regulating feedback on, i.e. at constant frequency shift. The images were repeatable after this contrast appeared in Fig. 6–3(b). The resolution over the quantum dot is especially impressive in Fig. 6–3(c) as usually we only obtain an image of that quality by imaging in the repulsive force regime. Notice that many of the features in Fig. 6–3(c) can also be identified in Fig. 6–3(d) which is also an indication that the dissipation image is recording electrostatic information. In the second experiment, the peak in the dissipation occurred at a different voltage for a spectra taken over the wetting

layer [Fig. 6–4(a)], however we still obtained interesting features in the dissipation images, as shown in Fig. 6–4(b).

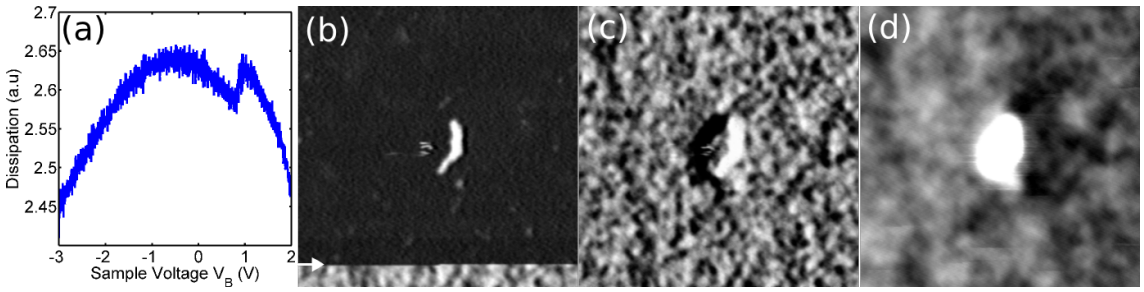

Figure 6–3: (a) Dissipation-voltage spectra showing an anomalous peak around 1 V, taken over the wetting layer. (b) Dissipation channel recorded with $V_B = 1.2$ V and $\Delta\omega/2\pi = -15.8$ Hz, during the scan the dissipation image abruptly changed in contrast (slow scan direction is downwards). (c) Dissipation channel taken with $V_B = 1.2$ V, and $\Delta\omega/2\pi = -15.84$ Hz and the simultaneously acquired electrostatic topography image in (d). Images taken at 4.5 K with 8 nm oscillation amplitude. All images are 500 by 500 nm.

The cause of this peak is unknown and we speculate that it is tip (as opposed to sample) related because of the irreproducibility of the dissipation peak location and because the presence of the peak is rare. As the images are reproduced over the sample surface, it seems we are imaging some feature of the sample. These two observations indicate that the tip is ultra-sensitive to charge, for example in surface states or the bulk, potentially due to something on the tip which fluctuates in response to charge variations over the sample surface.

Imaging Impurities

As mentioned in Chapter 4, we occasionally observe rings that are not located near a quantum dot. Most often, we are only able to discern a single ring, and even when the voltage is increased further a second ring is not resolved. It is possible that we are observing the ionization of impurities in this case. An STM study observed

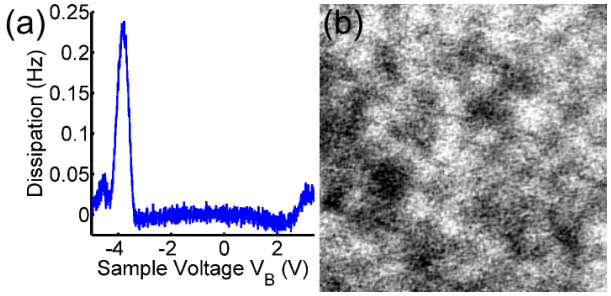

Figure 6–4: (a) Dissipation-voltage spectra, showing a peak in dissipation around −4 V. (b) Constant height dissipation image taken over the wetting layer (area of a quantum dot sample where there are no quantum dots) with $V_B = -4.3$ V. Image is 700 nm by 700 nm. Data taken 4.5 K with 4 nm oscillation amplitude.

single rings over silicon donors in a GaAs sample which they concluded were caused by the ionization [103]. Another possibility is the formation of quantum dots due to small regions of InAs caused by incomplete surface coverage of the wetting layer [104], or even quantum dots formed in the 2DEG due to variations of the electrostatic landscape of that location [27]. We need to acquire more data on these features, but the dissipation signal of these features is especially weak, even for smaller amplitudes, and this makes it difficult to characterize these rings. Fig. 6–5 shows the evolution of such a ring for increasing V_B. The ability to locate, characterize, and potentially even utilize, single impurities is an interesting avenue which is being pursued with a number of experimental techniques.

6.1.4 Coupled Quantum Dots

Further investigation of the coupled dots is definitely needed, not only to advance our understanding of the physics of the coupling in quantum dots and molecules but since coupled quantum dots have important potential applications (e.g. as qubits in a quantum computer). In particular, it may be possible to detect a signature of the tunnel versus co-tunnel coupling mechanism.

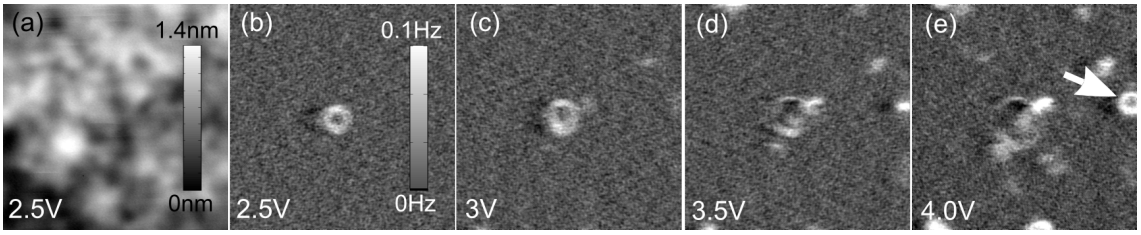

Figure 6–5: (a) Electrostatic topography of quantum dot sample, taken over the same area as Fig. 6–4(a), with $\Delta\omega/2\pi = -27.8$ Hz. and $V_B = 2.5$ V as marked on the image. An InP step-edge is in the bottom left corner. All images are over the same area and are 700 nm by 700 nm. (b) - (e) are constant height dissipation images showing the spreading of a single ring at the center of the images. In (e) a white arrow points to another single ring that is showing up. These are different from the rings associated with the InAs islands, which show up in the vicinity of the islands at negative voltages. Images taken at 4.5 K with 4 nm oscillation amplitude.

Fig. 6–6 highlights some of the features of coupled quantum dots which we are going to look into further. Fig. 6–6(a) and (d) are the simultaneously obtained frequency shift and dissipation images taken in constant height imaging mode. In Fig. 6–6(a) there are some areas of increased frequency shift in the image that occur when rings from two separate dots anti-cross (it is much easier to see these areas on the electronic version of the thesis rather than the printed version). This is emphasized by subtracting the background frequency shift which is influenced by the dot topography [Fig. 6–6(b)], and then redisplaying Fig. 6–6(b) with circles placed over the areas of increased frequency shift. Arrows in Fig. 6–6(b) point to areas of elongated increases in frequency shift. The dots and arrows are then overlayed on the dissipation image in Fig. 6–6(d). The topography of this quantum dot is the inset in Fig. 6–6(c). An increase in frequency shift that is not mirrored in the dissipation indicates that the cantilever has detected a faster tunneling rate in this region (recall Eq. 2.39 and Fig. 2–2). Although we cannot say for certain, this could be the detection of tunneling between the dots since the tunnel barrier between dots

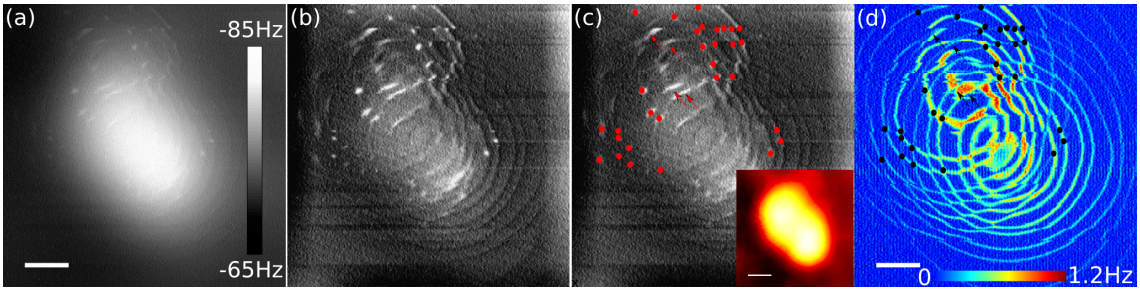

Figure 6–6: (a) Frequency shift image of an InAs island. Sharp increases in the frequency shift are visible. (b) Same image as (a) but with the background subtracted. (c) Peak-like increases are marked with circles and line-shaped increases marked with arrows. The inset in (c) is showing the topography of the quantum dot. (d) The simultaneously acquired dissipation image, with the same overlayed circles, showing that the peaks in frequency shift are occurring at the triple points and the lines occur along larger intersections of the rings. Both images acquired at 4.5 K, with 0.4 nm oscillation amplitude. Scalebar is 20 nm.

should be smaller than the InP tunnel barrier, which would lead to a faster tunneling rate. Conversely, the tunneling rate of co-tunneling events is much slower than the tunneling rate of single electron processes, by a factor R_K/R_T where $R_K = h/e^2$ and R_T is the tunneling resistance [51]. We do not have many examples of the sharp increases in frequency shift such as those observed in Fig. 6–6(a), since initially we were focused on characterizing single isolated quantum dots, but we have observed similar features in a small subset of other coupled quantum dots.

More theoretical analysis needs to be done before we know what to expect between capacitively, tunnel, and co-tunnel coupled dots. We are continuing to collaborate with Dr. Clerk's condensed matter theory group at McGill in order to clearly distinguish between them.

6.1.5 Other Quantum Dot Samples

The experiments we have demonstrated on quantum dots can be applied to several other types of interesting samples. Our next candidate for Coulomb blockade studies will be a capped quantum dot sample. Optical measurements require quantum dots to be capped and so to be able to compare our results with those measurements we need to characterize the energy levels of the capped quantum dots. We studied one capped sample and observed rings in the dissipation [Fig. 6–7(a) shows the topography and (b) the dissipation image at $V_B = -7$ V], but the density of quantum dots was fairly high and it was difficult to isolate the rings from just one dot. Further, the rings did not behave the same way as the rings from the uncapped quantum dot sample. The ring shape seemed relatively unaffected by temperature [Fig. 6–7(c)] or changes in the bias voltage. Although more rings became visible with a larger V_B, the diameter of the rings seemed unaffected, and as the temperature was increased the rings did not noticeably thermally broaden. Currently, we do not have an explanation for these results, however we note that the density of the quantum dots is very high on this sample and perhaps we are observing a regime where many body interactions are prevalent. We now have a sample with a lower density of dots, and we hope to be able to isolate one for study.

We are also interested in investigating gold nanoparticles as quantum dots in controllable architectures so that we can investigate dot coupling more effectively. Gold nanoparticles connected via specific lengths of DNA are given to us through a collaboration with Dr. Sleimann in the Chemistry department at McGill. These samples separate the gold nanoparticle quantum dots at preselected distances, providing an excellent platform for investigating different dot coupling regimes and how to characterize them with the AFM. These kinds of studies pave the way for devices

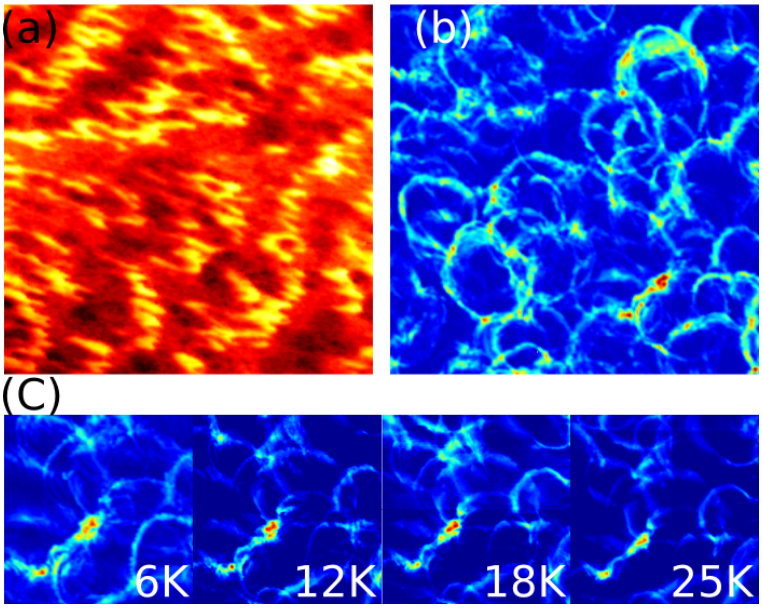

Figure 6–7: (a) Topography image of capped quantum dot sample. Image is 1 μm^2, $\Delta\omega/2\pi = -0.4$ Hz, using Kelvin Force Probe Microscopy ($V_{ac} = 0.6$ V_{rms} with 1 kHz frequency and 10 ms time constant for the lock-in. (b) Constant height dissipation image taken over the same area as (a) with $V_B = -7$ V. (c) Series of constant height dissipation images for increasing temperature (all images are 400 nm $\times$ 400 nm taken with $V_B = -7$ V). Dissipation has the same colour scheme as previous figures, but a colourbar is omitted since it was difficult to subtract the background. Dissipation in these images is approximately 1.5 Hz. All images took 18 min to complete.

based on larger scale self-assembled architectures. The size of the gold nanoparitcles can be controlled relatively well and dots can be made small enough that the Coulomb blockade regime is accessible at room temperature.

6.2 Conclusions

The main results of the work presented in this thesis are concisely summarized below.

6.2.1 Quantum Dot Spectroscopy

From the thermally broadened linewidth of the Coulomb blockade peaks, we were able to extract the lever arm, α, which allowed us to estimate E_C and ΔE. By measuring the position of the dissipation peak maxima as a function of temperature, we were able to extrapolate values for E_C and ΔE at $T = 0$ K. Additionally, we demonstrated the first example where the shell structure of a quantum dot was verified via a temperature experiment. By increasing the cantilever-dot coupling through increasing the cantilever oscillation amplitude, we moved from the weak to the strong coupling regime. In this regime, we demonstrated for the first time that the shell structure can also be verified simply by sweeping the sample voltage. Increasing the coupling even further allowed for the electron to enter a higher energy shell of the dot. Theoretically this leads to a small bump on the dissipation peak which is within our resolution to observe and in a future experiment we will look for this feature. The success of this work relied heavily on the theoretical model developed by Steven Bennett and Dr. Aashish Clerk which yielded an excellent agreement between theory and experiment. Dissipation measurements are still in their infancy within the AFM community, making the explanation of where the dissipation is coming from all the more valuable.

6.2.2 Quantum Dot Environment

We detected generation-recombination noise resulting from super-bandgap irradiation of a semi-conductor surface. From our measurements, we were able to deduce that the sample bandstructure was initially bent upwards at the surface due to negative charges which established an electric field within the sample. Super-bandgap irradiation created electron-hole pairs which were separated in this electric field with the holes moving towards the sample surface and relaxing the bands. We were able to characterize the generation-recombination noise time constant by taking the power spectral density of the cantilever resonance frequency shift as it reacted to charge fluctuations near the surface. A second time constant, that of the charge redistribution after the light was shut off, was also demonstrated.

To ensure that we were in the regime where the bands were nearly relaxed, we used Kelvin Probe Force Microscopy to measure the surface photovoltage as a function of laser power to find the laser power at which the surface photovoltage was saturated. Also, using electrostatic force microscopy we looked for reproducibility of the power spectral density curves once a certain laser power had been reached to verify we were in this regime.

The confinement potential of the uncapped self-assembled quantum dots did not allow for charge-pair separation, resulting in no fluctuations in overall charge with super-bandgap irradiation. This property was used to determine the spatial resolution of the technique, demonstrating a resolution better than 20 nm.

Since these results are, to our knowledge, the first measurements of generation-recombination noise using an AFM, we expect more of these measurements to be preformed in the future. In particular, with samples that rely heavily on light irradiation and the generation of excitons, namely photovoltaics. It would be nice to

see the technique used for locating recombination centers either in a bulk sample or within a molecule, and to observe spatially varying noise, for example over the wetting layer.

References

[1] T. Heinzel, *Mesoscopic Electronic in Solid Sate Nanostructures 2nd Edition*, Wiley-VCH, 2007.

[2] S. Tarucha, D. G. Austing, T. Honda, R. J. van der Hage, and L. P. Kouwenhoven, Phys. Rev. Lett. **77**, 3613 (1996).

[3] L. L. Sohn, L. P. Kouwenhoven, and G. Schon, *Mesoscopic Electron Transport*, Kluwer Academic, 1997.

[4] L. P. Kouwenhoven, D. G. Austing, and S. Tarucha, Rep. Prog. Phys. **64**, 701 (2001).

[5] D. C. Ralph, C. T. Black, and M. Tinkham, Phys. Rev. Lett. **74**, 3241 (1995).

[6] J. M. Elzerman, R. Hanson, L. H. W. v. Beveren, L. M. K. Vandersypen, and L. P. Kouwenhoven, Appl. Phys. Lett. **84**, 4617 (2004).

[7] U. Meirav, M. A. Kastner, and S. J. Wind, Phys. Rev. Lett. **65**, 771 (1990).

[8] M. Ciorga, M. Pioro-Ladriere, P. Z. P. Hawrylak, and A. S. Sachrajda, Appl. Phys. Lett. **80**, 2177 (2002).

[9] R. Hanson, L. P. Kouwenhoven, J. R. Petta, S. Tarucha, and L. M. K. Vandersypen, Rev. Mod. Phys. **79**, 1217 (2007).

[10] M. Field et al., Phys. Rev. Lett. **70**, 1311 (1993).

[11] R. Schleser et al., Appl. Phys. Lett. **85**, 2005 (2004).

[12] W. Lu, Z. Ji, L. Pfeiffer, K. W. West, and A. J. Rimberg, Nature **423**, 422 (2003).

[13] T. Fujisawa and Y. Hirayama, Appl. Phys. Lett. **77**, 543 (2000).

[14] M. A. Reed et al., Phys. Rev. Lett. **60**, 535 (1988).

[15] M. Björk et al., Nano Letters **4**, 1621 (2004).

[16] R. C. Ashoori et al., Phys. Rev. Lett. **68**, 3088 (1992).

[17] R. C. Ashoori et al., Phys. Rev. Lett. **71**, 613 (1993).

[18] H. Drexler, D. Leonard, W. Hansen, J. P. Kotthaus, and P. M. Petroff, Phys. Rev. Lett. **73**, 2252 (1994).

[19] B. T. Miller et al., Phys. Rev. B **56**, 6764 (1997).

[20] M. Jung et al., Appl. Phys. Lett. **86**, 033106 (2005).

[21] M. Jung et al., Appl. Phys. Lett. **87**, 203109 (2005).

[22] Y. Igarashi et al., Phys. Rev. B **76**, 081303 (2007).

[23] Y. Igarashi et al., Journal of Physics Conference Series **61**, 463 (2007).

[24] K. Shibata et al., Journal of Crystal Growth **301-302**, 731 (2007).

[25] K. Shibata and K. Hirakawa, Journal of Crystal Growth **311**, 1795 (2009).

[26] S. H. Tessmer, P. I. Glicofridis, R. C. Ashoori, L. S. Levitov, and M. R. Melloch, Nature **392**, 51 (1998).

[27] M. J. Yoo et al., Science **276**, 579 (1997).

[28] I. Kuljanishvili et al., Nature Physics **4**, 227 (2008).

[29] N. Zhitenev et al., Nature **404**, 473 (2000).

[30] G. Binnig, H.Rohrer, Ch.Gerber, and E.Weibel, Phys. Rev. Lett. **49**, 57 (1982).

[31] U. Banin, Y. Cao, D. Katz, and O. Millo, Nature **400**, 542 (1999).

[32] G. Binnig, C. F. Quate, and C. Gerber, Phys. Rev. Lett. **56**, 930 (1986).

[33] M. T. Woodside and P. L. McEuen, Science **296**, 1098 (2002).

[34] J. Zhu, M. Brink, and P. L. McEuen, Appl. Phys. Lett. **87**, 242102 (2005).

[35] M. Woodside, *Scanned Probe Microscopy of the Electronic Properties of Low-Dimensional Systems*, PhD thesis, Berkeley University, 2001.

[36] J. Zhu, M. Brink, and P. L. McEuen, Nano Lett. **8**, 2399 (2008).

[37] M. Brink, *Imaging Single-Electron Charging In Nanostructures By Low-Temperature Scanning Force Microscopy*, PhD thesis, Cornell University, 2006.

[38] A. Dana and Y. Yamamoto, Nanotechnology **16**, S125 (2005).

[39] R. Stomp et al., Phys. Rev. Lett. **94**, 056802 (2005).

[40] Y. Azuma, M. Kanehara, T. Teranishi, and Y. Majima, Phys. Rev. Lett. **96**, 016108 (2006).

[41] C. Schonenberger and S. F. Alvarado, Phys. Rev. Lett. **65**, 3162 (1990).

[42] L. J. Klein and C. C. Williams, Appl. Phys. Lett. **79**, 1828 (2001).

[43] J. P. Johnson, N. Zheng, and C. C. Williams, Nanotechnology **20**, 055701 (2009).

[44] E. Bussmann and C. C. Williams, Appl. Phys. Lett. **88**, 263108 (2006).

[45] E. Bussmann, N. Zheng, and C. C. Williams, Nanoletters **6**, 2577 (2006).

[46] L. Gross et al., Science **324**, 1428 (2009).

[47] D. Dalacu et al., Laser & Photon. Rev. (2009).

[48] D. Loss and D. P. DiVincenzo, Phys. Rev. A **57**, 120 (1998).

[49] T. Tanamoto, Phys. Rev. A **61**, 022305 (2000).

[50] M. Kastner, Physics Today **46**, 9 (1993).

[51] H. Grabert and M. Devoret, *Single Charge Tunneling Coulomb Blockade Phenomena in Nanostructures*, Plenum Press, 1992.

[52] L. Jacak, P. Hawrylak, and A. Wojs, *Quantum Dots*, Springer, 1998.

[53] S. D. Bennett, L. Cockins, Y. Miyahara, P. Grütter, and A. A. Clerk, PRL **104**, 017203 (2010).

[54] L. Cockins, Y. Miyahara, R. Stomp, and P. Grutter, Rev. Sci. Instrum. **78**, 113706 (2007).

[55] V. Braginsky and F. Khalili, in *Quantum Measurements*, edited by K.S.Thorne, chapter 1, pages 12–14, Cambridge University Press, 1992.

[56] Y. Martin, C. C. Williams, and H. K. Wickramasinghe, J. Appl. Phys. **61**, 4723 (1987).

[57] J. E. Sader et al., Nanotechnology **16**, S94 (2005).

[58] T. R. Albrecht, P. Grütter, D. Horne, and D. Rugar, J. Appl. Phys. **69**, 668 (1991).

[59] H. Hölscher et al., Phys. Rev. B **64**, 075402 (2001).

[60] F. J. Giessibl, Appl. Phys. Lett. **78**, 123 (2001).

[61] H. J. Hug and A. Baratoff, in *Noncontact Atomic Force Microscopy*, edited by S. Morita, R. Wiesendanger, and E. Meyer, chapter 20, pages 395–432, Springer, 2002.

[62] J. N. Israelachvili, *Intermolecular and Surface Forces with Applications to Colloidal and Biological Systems*, Academic Press, 1985.

[63] J. Hutter and J. Bechhiefer, J. Appl. Phys. **73**, 4123 (1993).

[64] U. Hartmann, J. Vac. Sci. Technol. B **9**, 465 (1991).

[65] S. Hudlet, M. Saint-Jean, C. Guthmann, and J. Berger, Eur. Phys. J. B **2**, 5 (1998).

[66] R. Stomp, *Dissipative and Electrostatic Force Spectroscopy of InAs Quantum Dots by Non-contact Atomic Force Microscopy*, PhD thesis, McGill University, 2005.

[67] L. Cockins et al., PNAS **107**, 9496 (2010).

[68] A. A. Clerk and S. Bennett, New J. Phys. **7**, 238 (2005).

[69] T. Ota et al., Phys. Rev. Lett. **93**, 066801 (2004).

[70] H. I. Rasool, P. R. Wilkinson, A. Z. Stieg, and J. K. G, Rev. Sci. Instrum. **81**, 023703 (2010).

[71] M. Roseman and P. Grutter, Rev. Sci. Instrum. **71**, 3782 (2000).

[72] M. Roseman, *Low Temperature Magnetic Force Microscopy Studies of Superconducting Niobium Films*, PhD thesis, McGill University, 2001.

[73] L. Cockins, High aspect ratio cantilever tips for non-contact electrostatic force microscopy, Master's thesis, McGill University, 2006.

[74] S. Pan, Piezo-electric motor, International patent publication No. W093/19494, International Bureau, World Intellectual Property Organization.

[75] A customized version of Scanita was designed and built at the University of Basel.

[76] D. Rugar, H. J. Mamin, and P. Guethner, Appl. Phys. Lett. **55**, 2588 (1989).

[77] K. Bruland et al., Rev. Sci. Instrum. **70**, 3542 (1999).

[78] Nanosurf, *easyPLL FM Sensor Controller*, 2 edition.

[79] M. Grundmann, *The Physics of Semiconductors*, Springer, 2006.

[80] I. N. Stranski and L. V. Krastanow, Akademie der Wissenschaften und der Literatur in Mainz **146**, 797 (1939).

[81] P. J. Poole, J. McCaffrey, R. L. Williams, J. Lefebvre, and D. Chitrani, J. Vac. Sci. Technol. **B19**, 1467 (2001).

[82] J. G. A. Dubois, E. N. G. Verheijen, J. W. Gerritsen, and H. van Kempen, Phys. Rev. B **48**, 11260 (1993).

[83] M. Nonnenmacher, M. P. O'Boyle, and H. K. Wickramasinghe, Appl. Phys. Lett. **58**, 2921 (1991).

[84] N. Spasojevic, Electrostatic simulations of interactions between a scanning probe and quantum hall liquid, BSc Thesis, 2005, Massachusetts Institute of Technology.

[85] A. Finck, Numerical simulation of a laterally confined double dot with tunable interaction potential, BSc Thesis, 2005, Massachusetts Institute of Technology.

[86] C. W. J. Beenakker, Phys. Rev. B **44**, 1646 (1991).

[87] W. G. van der Wiel et al., Rev. Mod. Phys. **75**, 1 (2003).

[88] M. E. Welland and R. H. Koch, Appl. Phys. Lett. **48**, 724 (1986).

[89] E. N. Schulman and R. C. White, Phys. Rev. B **52**, 7864 (1995).

[90] S. Sugita, Y. Mera, and K. Maeda, J. Appl. Phys. **79**, 4166 (1996).

[91] M. Pioro-Ladriere et al., Phys. Rev. B **72**, 115331 (2005).

[92] J. E. Hill and K. M. V. Vliet, J. Appl. Phys. **29**, 177 (1958).

[93] D. C. Coffey and D. S. Ginger, Nature Materials **5**, 735 (2006).

[94] L. Cockins, Y. Miyahara, and P. Grutter, Phys. Rev. B **79**, 121309 (2009).

[95] J. Copeland, IEEE Transactions on Electron Devices **18**, 50 (1971).

[96] L. Kronik and Y. Shapira, Surface Science Reports **37**, 1 (1999).

[97] V. Palermo, M. Palma, and P.Samori, Advanced Functional Materials **18**, 145 (2006).

[98] C. Loppacher et al., Nanotechnology **16**, S1 (2005).

[99] V. Fock, Z. Phys. **47**, 446 (1928).

[100] C. Darwin, Proc. Camb. Phil. Soc. **27**, 86 (1930).

[101] P. Makslyn, in *Atoms and Molecules in Strong External Fields*, chapter 27, pages 301–311, Springer US, 2002.

[102] S. Csonka et al., Nanolett. **8**, 3932 (2008).

[103] K. Teichmann et al., Phys. Rev. Lett. **101**, 076103 (2008).

[104] A. Babiński et al., Appl. Phys. Lett. **92**, 171104 (2008).